

VICTORIA UNIVERSITY OF TECHNOLOGY

DEPARTMENT OF MECHANICAL ENGINEERING



**MODELLING THE SCAVENGING PROCESS
IN A TWO-STROKE I.C. ENGINE**

BY

QI XIAN ZHANG

**A RESEARCH THESIS SUBMITTED IN FULFILMENT OF
THE REQUIREMENT FOR THE DEGREE OF MASTER OF ENGINEERING
BY RESEARCH**

1995

To my mother, Wen Shu Hua

FTS THESIS
621.430113 ZHA
30001004525202
Zhang, Qi Xian
Modelling the scavenging
process in a two-stroke I.C.
engine

ACKNOWLEDGMENT

The work reported in this thesis was carried out in the Department of Mechanical Engineering of the Victoria University of Technology.

I would like to express my deep gratitude and thanks to my supervisor, Dr. Michael Sek, for his valuable guidance and patient support of this work. Without his vision and constructive suggestion this project would not have been possible. He has been a great source of encouragement.

I am grateful to thank Professor Geoff Lleonart for his valuable consultation and patient correction of this thesis. Without his critical vision, this thesis would not achieve its current quality.

I wish to thank the head of Mechanical Engineering Department, Associate Professor Kevin Duke, for the part-time employment I was offered which enable me to finish my study.

I wish to thank the technical staff at the Department of Mechanical Engineering, especially Mr. Harry Friedrich, Ray Mackintosh and Harry Braley, for their practical assistance on many occasions.

I am thankful to Yamaha Australia for their kind donation of a Yamaha two-stroke engine to the Department of Mechanical Engineering. All engine testing was conducted on this engine.

I am grateful to my friend, Mr. Cliff Hadley, especially for his help and encouragement. He also helped me to correct this thesis.

I am highly obliged to my beloved wife Xin Yuan, and lovingly daughter Katie, who was born at the conclusion of this project. Without Xin's understanding and moral support, I would not be able to brave enough to complete this work. She also helped me greatly in binding this thesis before it comes to publication.

I am deeply in debt to my parents, Wen Shu Hua and San Wei Zhang, for the enormous love and understanding I used to received from them.

ABSTRACT

The primary concern associated with a two-stroke engine performance is its gas exchange process (scavenging process). The success of the scavenging process greatly affects the thermodynamic properties of cylinder content at the trapping conditions and hence the combustion and power output. The unsteady gas flow in engine pipes has a marked influence on the scavenging process.

In the current study, the two-stroke engine simulation model has been developed to predict the steady state performance characteristics of a crankcase compressed, piston port-timed, two-stroke engine equipped with expansion chamber. The characteristics include parameters such as engine torque and power, BSFC, scavenging efficiency and charging efficiency. The model also has the ability to predict the unsteady gas dynamic behaviour in various engine pipes. The instantaneous pressure fluctuation and mass flow rates at inlet port, transfer port and exhaust port were calculated and analysed.

The model has several advantages compared with other one-dimensional isentropic model. It includes an improved procedure to account for the variation in geometry of pipe and to determine the thermodynamic states in cylinder/crankcase. The model also considered the temperature discontinuity at port/pipe interface. All these efforts increase the accuracy and numerical stability of the prediction.

A single cylinder two-stroke engine dynamometer rig and dedicated fast data acquisition hardware and software have been developed in the project. Engine torque, speed and fuel consumption can be measured on the dynamometer rig. The dynamic pressure signals in engine cylinder, transfer port and exhaust port, together with crankshaft position signal, can be acquired at a speed of 50,000 sample/second per channel, sufficient for accurate acquisition of experimental data.

Substantial simulations and experiments were performed and the computer model was validated. A variable exhaust system, as described in this study, was used to improve a two-stroke engine's performance under off-design engine speeds. This was realised by making the mid-parallel section of a conventional expansion chamber extendable, while the other dimensions of that chamber remained unchanged. In the study it was found that with the adjustable expansion chamber, the pressure wave timing at the exhaust port was under control within the test speed range (2200 - 4400 RPM) so that such wave timing matched the engine port timing, leading to a relative optimum in performance. The numerical approach proposed could satisfactorily handle the complicated pipe flow calculation and predict both engine performance and dynamic wave variations in the test engine. Thus the program can be used for improving the design and development of naturally aspirated, port-controlled crankcase compressed two-stroke engines.

NOMENCLATURE

English:

a	local speed of sound (m/s)
a^*	non-dimension speed of sound
a_0	speed of sound at reference pressure (m/s)
$a_{0,x}$	reference speed of sound at location x (m/s)
A	area (m ²)
BDC	bottom dead center
BMEP	brake mean effective pressure (kpa)
BSFC	brake specific fuel consumption (kg/kw*h)
C	denotes characteristic curves
c	wave propagation velocity (m/s)
C+, C-	unsteady flow Mach lines
C_0	unsteady flow path line
C_c	coefficient of contraction
C_D	coefficient of discharge
C_p	specific heat at constant pressure (J/kg*K)
C_v	specific heat at constant volume (J/kg*K)
CV1	control volume 1, ie, the cylinder
CV2	control volume 2, ie, the crankcase
E	system internal energy (J/kg)
EPC	exhaust port closure
EPO	exhaust port open
h	enthalpy (J/kg)
h	effective port height (cm)
H	geometric port height (cm)
IMEP	indicated mean effective pressure (kpa)
IPC	inlet port closure
IPO	inlet port open
K	mass flow ratio

k	instantaneous port/pipe area ratio
l	effective port width (cm)
L	differential operator
L_3	length of the middle parallel section of the exhaust pipe (mm)
M	local Mach number
\dot{m}	mass flow rate (kg/s)
n^*	node n at new time step in the physical (Z-X) plane
p	pressure (pa)
p_0	reference pressure (pa)
$P_{cc} - p_{cyl}$	pressure difference between crankcase and cylinder (kpa)
p_i	pressure of the incident wave (pa)
p_r	pressure of the reflecting wave (pa)
Q	heat transferred to or from the system (J/kg)
R	gas constant (J/kg*K)
R_m	universal gas constant (J/kg*K)
RPM	revolution per minute
s_1	transfer port area ratio
s_2	throttle area ratio
T	gas temperature (K)
t	time (sec)
T_0	reference temperature (gas temperature at reference pressure) (K)
TDC	top dead center
TPC	transfer port closure
TPO	transfer port open
u	gas particle velocity (m/s)
$u_{R,E}, u_{L,E}$	gas particle velocity on simple pressure wave (m/s)
$u_{R,L}, u_{L,R}$	relative velocity (m/s)
$u_{(R,E)S}, u_{(L,E)S}$	gas particle velocity on superposed pressure wave (m/s)
U	non-dimensional gas particle velocity
w	work (J/kg)
W	geometric port width (cm)
X, X_w, X_r	non-dimensional distance

x	distance (m)
x	the scavenging ratio at displacement/mixing transition point in Benson-Brandham scavenging model
X	pressure amplitude ratio
X_1	pressure amplitude ratio in cylinder
X_i	pressure amplitude ratio of incident wave
X_L	pressure amplitude ratio of left-ward running wave
X_R	pressure amplitude ratio of right-ward running wave
X_r	pressure amplitude ratio of reflecting wave
X_s	superposition pressure amplitude ratio
y	the proportion of short-circuiting in Benson-Brandham scavenging model
Z	non-dimensional time
Greek:	
B	the group $(2X_i-1)/X_1$
γ	ratio of specific heat
ΔZ	non-dimensional time increment
ϵ	mass imbalance rate in duct
η_c	charging efficiency
η_s	scavenging efficiency
θ_{ax}	port axial inclination angle
θ_{tan}	port tangential inclination angle
λ_d	delivery ratio
λ_s	scavenging ratio
λ, β	Riemann variable
λ', β'	Riemann variable after considering the effect of non-uniform reference temperature
λ_n^*, β_n^*	Riemann variable at node n at new time step
$\lambda_w, \lambda_r, \beta_w, \beta_r$	Riemann variable at interpolation point
ρ	gas density (kg/m^3)

ρ_0	reference gas density (kg/m ³)
$\sigma_1, \sigma_2, \sigma_3$	arbitrary parameters
Ψ	pressure ratio

CONTENTS

CHAPTER 1

INTRODUCTION	1
1.1 Background	1
1.2 Research Objectives and Significance	3
1.3 Research Methodology	3
1.4 Scope of the Study.	5
1.5 Organisation of Thesis.	6

CHAPTER 2

MODELLING AND STUDIES OF SCAVENGING

IN THE TWO-STROKE ENGINE - LITERATURE REVIEW	7
2.1 Scavenging	7
2.2 Definitions and Terminology	9
2.3 Experimental and Theoretical Evaluation of the Scavenging Process	11
2.3.1 Experimental Studies of Scavenging	12
2.3.2 Theoretical Modelling of the Scavenging Process	15
2.4 Improvement of the Scavenging Process	24
2.4.1 Non-symmetric Port Timing	24
2.4.2 Stratified Charging.	27

CHAPTER 3

THEORETICAL CONSIDERATIONS

AND DEVELOPMENT OF MODELLING A TWO-STROKE ENGINE	30
3.1 Introduction	30
3.2 Fundamentals of Pressure Wave Theory.	30
3.2.1 Basic Concepts	30
3.2.2 Superposition of Pressure Waves	34
3.2.3 Reflection of Pressure Wave at Port/Pipe Boundary	37
3.3 The Method of Characteristics (MOC)	40
3.4 Characteristic and Compatibility Equations for Quasi One Dimensional	

	Flow in a Pipe	42
3.5	Solution of Equations with the Riemann Variable Technique	48
3.6	Evaluation of Flow Variables in Terms of Riemann Variables	52
3.7	Computation of Riemann Variables	54
3.8	Integration of Riemann Variables Along the Direction of Characteristics	61
3.9	Calculation of Riemann Variables At Pipe Ends.	67
3.10	Determination of In-Cylinder Thermodynamic State During the Scavenging Process: Open Cycle Analysis	70
	3.10.1 Energy Equation for Cylinder/Crankcase	70
	3.10.2 Reflections Due to Non-Isentropic Behaviour at the First Node.	79
	3.10.3 Computational Procedure for Flow at Port/Pipe Boundary.	84
3.11	Verification of Mass Balance	85
	3.11.1 Mass Flow Balance in Pipes	85
	3.11.2 Mass Balance Across Engine Ports.	86
 CHAPTER 4		
	COMPUTER SIMULATION.	87
4.1	Model Description	87
4.2	Model Assumptions	88
4.3	Discussion of the Computer Simulation Results.	92
	4.3.1 Discussion of Calculated Wave Diagrams	95
	4.3.2 The Analysis of Scavenging Quality	100
	4.3.3 Optimisation of Exhaust Pipe for Rated Output Condition.	101
	4.3.4 Mass Balance Examination.	105
 CHAPTER 5		
	EXPERIMENTAL APPARATUS	106
5.1	Introduction	106
5.2	Test Engine Specification	106
5.3	Construction of Experimental Apparatus and Engine Instrumentation	106
	5.3.1 Fuel System	107

5.3.2	Torque Measurement	109
5.3.3	Dead Centre Marker and Engine Speed Measurement	113
5.3.4	Pressure Transducer Installation and Pressure Trace Measurement	116
5.3.5	Measurement of Exhaust Temperature	116
5.4	Computerised Data Acquisition System	116
5.4.1	Description of Hardware	117
5.4.2	Description of Software	118
5.5	Engine Experimental Procedure	119

CHAPTER 6

EXPERIMENTAL RESULTS AND DISCUSSION	121
6.1 Introduction	121
6.2 Measured and Predicted Performance Characteristics.	121
6.3 Measured and Predicted Pressure Traces	127
6.4 Discussion	128

CHAPTER 7

CONCLUSIONS	136
7.1 Research Achievement.	136
7.2 Conclusions	137
7.3 Recommendation For Future work	137

REFERENCES	139
----------------------	-----

Appendix A: Measurement of $\eta_s - \lambda_s$ Characteristics With QUB Single Cycle Scavenging Rig	145
---	-----

Appendix B: Computer Program for Unsteady Quasi One-Dimensional Pipe Flow . .	147
---	-----

Appendix C: Computer Model Testing of the Effect of Various Schemes on the Changes of Pipe Area	150
--	-----

Appendix D: Computer Model Testing of the Effect of Various Computational Mesh Size	153
Appendix E: Computer Model Testing of the Effect of Modifications of Wave Reflection Near Engine Ports Due to Discontinuous Reference Temperatures	155

CHAPTER 1

INTRODUCTION

1.1 Background

An internal combustion engine (I.C. engine) which has a power stroke in each cylinder during each revolution of the crankshaft is classified as a two-stroke engine. The "simple" two-stroke engines use crankcase compression for the induction process, while the controlling of the timing and area of the inlet, transfer and exhaust ports are fulfilled by pistons. Fig. 1.1 shows a schematic layout of such a two-stroke engine. Depending on the manner of the introduction of fuel, both compression ignition and spark ignition two-stroke engines have been developed in the past. The main advantages of this engine type, compared with its four-stroke engine rival, are its mechanical simplicity, superior power to weight ratio, lower production cost and lower maintenance cost.

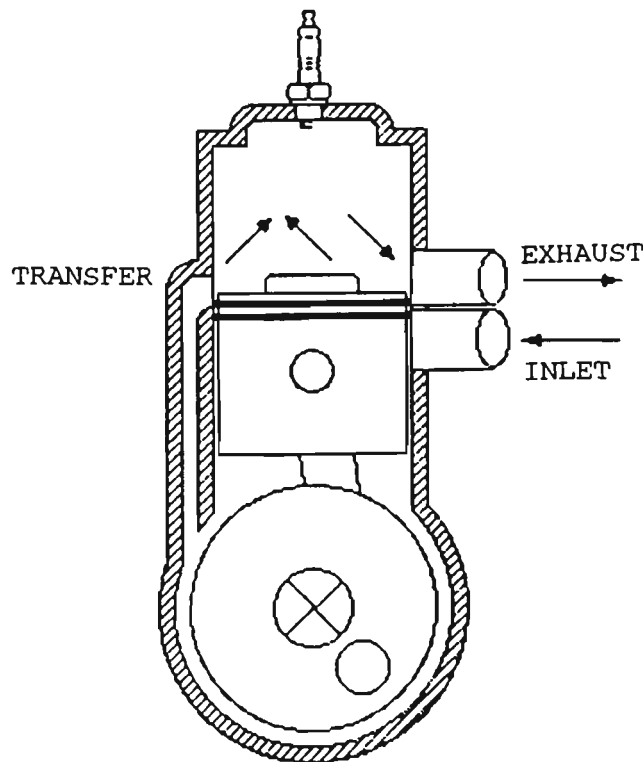


Fig. 1.1 A simple two-stroke engine

Two-stroke engine applications in modern life are numerous. For a conventional carburetted two-stroke engine, which is the focus of this study, typical applications are found as power units for:

- * hand-held tools, such as chain saws, lawn mowers, brush cutters
- * transportation, such as motorcycles, mopeds and scooters
- * electricity generators
- * racing machines, such as motorcycles and outboard motors
- * recreational products, such as go-kart, snowmobile and remotely-controlled model air planes.

The primary concern associated with a two-stroke engine is its gas exchange process (scavenging process). The success of this process greatly affects the thermodynamic properties of cylinder contents at the trapping conditions and hence the ensuing combustion and power output. Scavenging is complicated by the fact that during the scavenging period, the gas flows into and out of the engine cylinder take place at the same time. The incoming fresh charge only partly displaces the burnt gases and partly mixes with them. An extreme case is that some entering fresh charge leaves the cylinder through the exhaust ports without either displacing the burnt gases or mixing with them, this is technically termed short-circuiting. The unsteady gas flows in engine pipes sometimes further complicates the problem. The consequences may be high fuel consumption, high hydro-carbon (HC) emission levels and low performance figures.

The opening and closing timing of a simple crankcase-scavenged two-stroke engine is fixed and symmetric with respect to the bottom dead centre. The timing for the ports is optimised for best performance at a well-defined condition of operation. At off-design operating conditions the engine cannot take advantage of the unsteady gas dynamic effect created by the exhaust expansion chamber which assists the scavenging process under normal operating conditions. The performance characteristics may be significantly degraded due to the occurrence of short circuiting and back flow (exhaust flow entering cylinder via exhaust port, or, cylinder contents entering transfer ducts via transfer ports).

1.2 Research Objectives and Significance

The scavenging process is dominated by in-cylinder scavenging and the combined gas dynamic effect in various sections of the engine. The emphasis of this research is on investigating the effect of unsteady gas dynamics in the exhaust expansion chamber on the performance characteristics of a two-stroke engine operating at off-design conditions. The aims include:

- 1) Development of a computer model to simulate exhaust gas dynamics and prediction of the performance of a two-stroke engine equipped with an exhaust expansion chamber under various operating conditions.
- 2) Design and construction of a dynamometer rig for on line monitoring and simultaneous acquisition of data.
- 3) Validation of the model by comparing its predicted performance with engine test data.

The successful outcome of the project may contribute to economy in fuel consumption as well as reducing hydro-carbon emission from two-stroke engines.

1.3 Research Methodology

The improvements of two-stroke engine performance under off-design operating conditions are usually realised "mechanically" by introducing the necessary variable exhaust port timing and area, or, a non-symmetrical port-timing arrangement, to reduce the unwanted short-circuiting and back flow. Tsuchiya *et al* [1]¹ and Sher *et al* [2] studied the installation of a butterfly valve at the exhaust port. The oscillating charge trapping valve situated in the exhaust port was designed and tested by Blundell *et al* [3]. The non-

¹ Number in brackets designates reference number.

symmetrical effect at the inlet port can be obtained by fitting a rotary disk valve, Blair [4]; a reed valve, Blair *et al* [5]; or a fluid diode, Sher [6]. Scroll diodes were fitted in transfer ports to reduce the back flow, Sher [7]. Good results were claimed but at the cost of unavoidable mechanical complexity.

A well known simple and effective method used to increase two-stroke engine performance is to control the dynamic pressure at the exhaust port. This study investigates the application of the unsteady gas dynamic effect in a quasi-one dimensional pipe to enhance the scavenging process. The analysis will be further extended to cover off-design operating conditions. By controlling the pressure wave reflection timing at the exhaust port, the reduced delivery ratio at off-design engine speed in conventional engines - which is responsible for poor performance - is postulated to improve the performance.

The proposed experimental program calls for testing two exhaust systems. These are: a box silencer which came as a standard item with the test engine and a specially designed extendable expansion chamber. The results from tests on each system would be compared with each other in order to establish whether the extendable pipe system is superior. As the only significant variable in the experiment would be the configuration of the exhaust systems, it is logical to conclude that any improved engine performance resulted from the improved overall scavenging quality brought about by the unsteady gas dynamic effect in the pipe system. The phenomenon may be explained in terms of the finite amplitude pressure wave theory. Three piezo-electric pressure transducers would be located at the exhaust port, transfer port and cylinder, respectively to get the data for such analysis.

Simulation of the compressible gas flow in pipes has always been one of the major difficulties in predicting two-stroke engine performance. The project will also entail theoretical studies of the unsteady gas flow in a quasi one-dimensional pipe, along with its effect on gas exchange processes and engine performance. This is necessary because a critical part of the experimental program will be the design of an engine exhaust system and an accurate computer model is required for that purpose. A two-stroke engine simulation model originally proposed by Blair *et al* [8], but requiring revision, will be developed for the simulation. A solution of the equations which govern the unsteady pipe

flow can be developed, it would include an improved procedure to account for the varying geometry of the pipe and to determine the flow at the port/pipe boundary.

Account needs to be taken of temperature dependant gas properties in the cylinder. The dimensionless time step predicted by the Courant-Friedrichs-Lewy (CFL) stability criterion in the pipe flow model should be multiplied by a factor of 0.95 to ensure numerical stability. The proportionally related quantities, the crank angle step and the dimensional time step, should be multiplied by the same factor.

Also, the calculation needs resetting at the crank angle of the exhaust port open (EPO) after a cycle, that is, each cycle starts and ends at the same position. Control points are added across the engine model to examine the mass conservation which reflects the quality of the numerical solution.

1.4 Scope of the Study

The computer model to be developed would seek to predict the engine performance characteristics such as torque, fuel consumption, scavenging efficiency as well as simulating the dynamic pressure histories in various locations in a two-stroke engine with an extendable exhaust pipe configuration. A dynamometer rig with the necessary instrumentation, a suitable computerised data acquisition system and appropriate software will be developed. A number of simulations and experiments will be performed with a two-stroke engine operating at various conditions and pipe lengths.

Changes in engine performance will be interpreted by analysing the pressure history at the exhaust port, transfer port and in the cylinder. Results from the computer simulations will be compared with engine experimental data to determine the accuracy of the model. Optimisation of the exhaust pipe lengths will also be investigated.

1.5 Organisation of Thesis

Chapter 2 surveys the literature in relation to: 1) scavenging the two-stroke engine cylinders, both theoretical and experimental studies; 2) methods of increasing two-stroke engine performance by innovative gas exchange processes, and 3) utilisation of pressure wave energy to assist in scavenging. The difficulties in the scavenging process are first examined, followed by a review of research efforts aimed at gaining a better understanding of this kind of I.C. engine. Some important quantities which characterise the scavenging process are defined at the beginning of the chapter.

Chapter 3 contains the thermodynamic and gas dynamic analysis of unsteady gas flow in a quasi-one dimensional duct, the analysis of cylinder and crankcase during open and closed cycle, and the description of the flow at a port/pipe boundary. Computational problems encountered in the simulation are discussed.

Chapter 4 provides the description of the computer two-stroke engine simulation code and the simulation model assumptions. Extensive numerical data available from the simulations are presented and discussed. The application of the program is demonstrated by presenting an optimised exhaust pipe which may greatly increase the test engine's output at rated speed.

Chapter 5 describes the construction of the experimental apparatus and instrumentation. The description of the development of the simultaneous sample and hold fast data acquisition system and software, instrument calibration, and experimental procedures are given.

Chapter 6 presents the engine test results. The measured engine performance characteristics and pressure wave diagrams in the cylinder and at exhaust and transfer duct are compared with the predicted results available from the computer simulations. The results are then discussed.

Finally, the conclusions of this study are drawn in Chapter 7.

CHAPTER 2

MODELLING AND STUDIES OF SCAVENGING IN THE TWO-STROKE ENGINE - LITERATURE REVIEW

2.1 Scavenging

The geometric characteristics of a crankcase compressed, loop-scavenged Schnurle-type two-stroke I.C. engine are illustrated below. The opening and closing timing of various engine ports are symmetrical with respect to bottom dead centre (BDC), Fig. 2.1. The scavenging ports, A-C and A'-C', are symmetrically located at the same level on both sides of the exhaust port, Fig. 2.2(a)(b). The principle of operation is explained with reference to Fig. 1.1. As the piston travels upward toward the top dead centre (TDC), the inlet port is opened (IPO) by the piston skirt. Fresh charge enters into the crankcase through the inlet pipe, while the contents of the cylinder are compressed. Combustion is initiated just before TDC of the stroke leading to a significant increase of the cylinder gas pressure and temperature. The high pressure gas forces the piston downward toward bottom dead centre. Some of the fresh charge may escape to the environment through the inlet port when the crankcase volume is reduced (back flow). After this the inlet port closes (IPC) and the fresh charge in the crankcase is compressed.

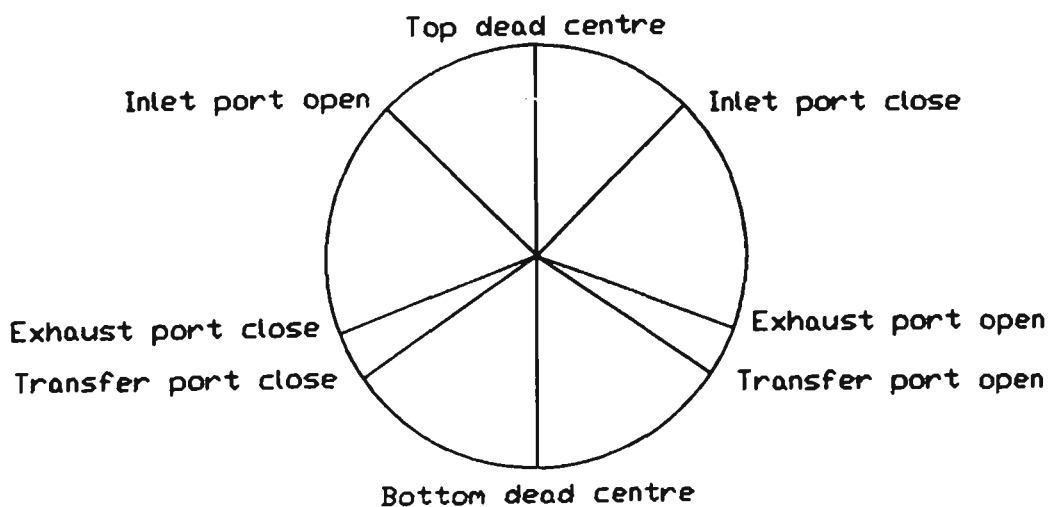
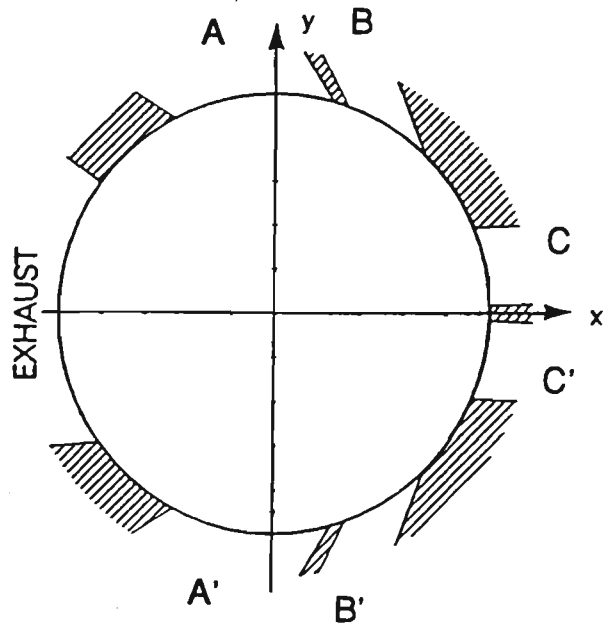
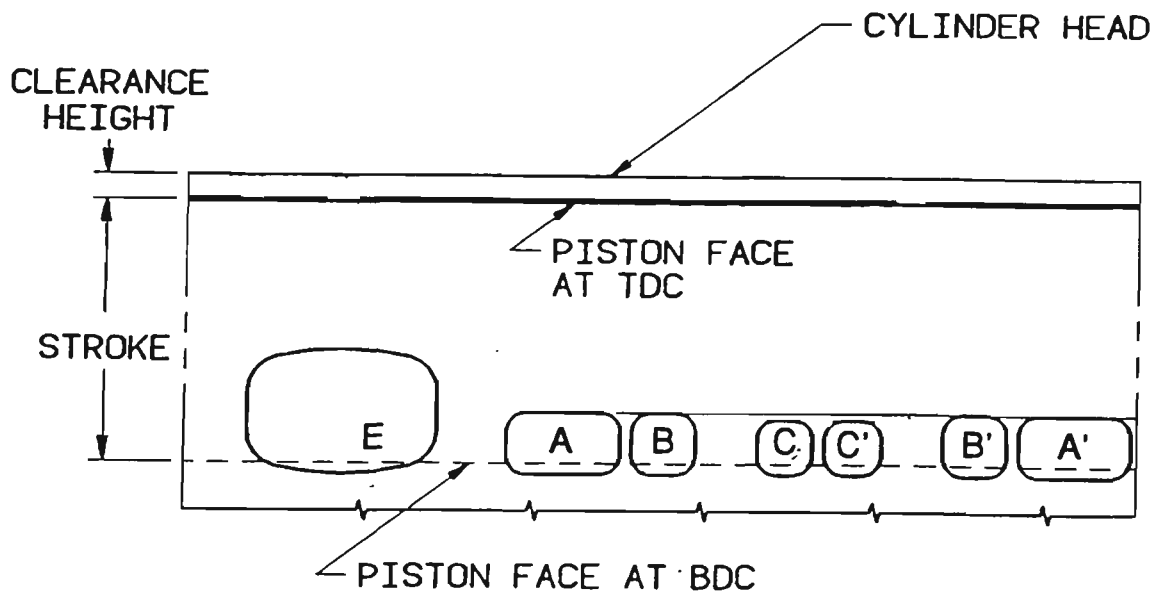


Fig. 2.1 Port timing characteristics of a simple two-stroke engine



(a)



(b)

Fig. 2.2 Port layout (a)(b) characteristics of a simple two-stroke engine

The gas exchange period begins as the exhaust port is opened (EPO). During this period the products of combustion are replaced by a fresh charge. In a carburetted engine the fresh charge consists of a mixture of fuel and air. This period may be divided into two sub-periods:

- 1) the exhaust blow down period - from the exhaust port open (EPO) to the transfer port open (TPO), and
- 2) the scavenging period - from the transfer port open (TPO) until the exhaust port close (EPC).

During the scavenging period, the compressed fresh charge in the crankcase flows through the transfer ducts into the cylinder and replenishes the combustion products through the exhaust port. The process is controlled by a pressure gradient across the cylinder, which governs the simultaneous inflow and outflow streams through the opened transfer and exhaust ports. As the piston passes BDC and travels upward, the crankcase volume increases, and another back flow from the cylinder to the crankcase through the transfer port may occur. After the transfer ports are closed (TPC), the fresh charge may escape through the exhaust port during the period TPC - EPC. In a conventional symmetrically timed two stroke engine where the opening and closing crank angle for each port is fixed and symmetrical with respect to the BDC , the TPC - EPC period is as long as the blowdown period. This is sufficiently long to lower the cylinder pressure at EPC with a corresponding decrease of engine performance due to a shortage of air/fuel mixture.

2.2 Definitions and Terminology

The performance, fuel economy and emission of any I.C. engine is heavily dependent on the thermodynamic properties of the mixture trapped inside the cylinder and its flow pattern at the commencement of the compression. In a two-stroke engine, these properties and velocity profiles are closely related to the effectiveness of the scavenging process[9], which in turn depends on the detailed geometrical layout of the port system, the combustion chamber shape and the configuration of pipes attached to the engine. The

parameters such as scavenging efficiency, charging efficiency, trapping efficiency and delivery ratio are employed to evaluate the effectiveness of this process. Their definitions follow the SAE Handbook[10]:

scavenging efficiency η_s :

$$\eta_s = \frac{m_a}{m_a + m_b} \quad (2.1)$$

trapping efficiency η_t :

$$\eta_t = \frac{m_a}{m_t} \quad (2.2)$$

charging efficiency η_c :

$$\eta_c = \frac{m_a}{\rho_a V_{cyl}} \quad (2.3)$$

delivery ratio λ_d :

$$\lambda_d = \frac{m_t}{\rho_a V_s} \quad (2.4)$$

also, volumetric scavenging ratio, λ_s :

$$\lambda_s = \frac{V_{tr}}{V_s} \quad (2.5)$$

The overall engine performance is mainly characterised by the following quantities:

brake specific fuel consumption (BSFC):

$$BSFC = \frac{\dot{m}_f}{P_b} \quad (2.6)$$

brake mean effective pressure (BMEP):

$$BMEP = \frac{P_b}{V_s n} \quad (2.7)$$

indicated mean effective pressure (IMEP):

$$IMEP = \frac{P_i}{V_s n} \quad (2.8)$$

where

- m_f - mean fuel flow rate (kg/s)
- P_b - brake power (kW)
- P_i - indicated power (kW)
- V_s - cylinder swept volume (m³)
- V_{cyl} - cylinder volume (m³)
- n - engine speed (rev/s)
- m_a - mass of supplied fresh charge trapped (kg)
- m_b - mass of trapped combustion residuals (kg)
- m_i - mass of fresh charge supplied by inlet port to the crankcase (kg)
- V_{tr} - volume of fresh charge supplied by transfer port to cylinder (m³)
- ρ_a - ambient density (kg/m³)

These quantities are used to compare the performance between different engines.

2.3 Experimental and Theoretical Evaluation of the Scavenging Process

Although the qualitative description of the scavenging process is straightforward, the quantitative determination of the scavenging parameters, as defined in section 2.2, is difficult. This is because there is no direct means of obtaining the amount of mass in the fresh charge trapped inside the cylinder during the gas exchange period and at the beginning of the compression (these mass quantities are the numerators in equations 2.1 - 2.3). Many experimental models have been proposed to evaluate the mass quantities. For example, the assessment of the composition of the trapped mass in the cylinder has been made using flow visualisation methods, and a prediction of short-circuiting has been made

from exhaust gas analysis.

Accurate theoretical descriptions of the gas dynamics are much more complicated. Recently, multi-dimensional computational fluid dynamic models based on the fundamental laws of mass, momentum and energy and particular relations which govern the fluid flow in the cylinder have been established. The results of such computations have shown details of the in-cylinder flow structure and development, and its influence on the gas exchange process. A proper description of the behaviour of the scavenging process not only improves the understanding of the mechanism of the in-cylinder gas exchange process, but is also essential for predicting the combustion and overall engine performance.

2.3.1 Experimental Studies of Scavenging

The internal mechanism of the gas exchange process and the improvement of the scavenging quality for a particular engine cylinder can be investigated by model testing. Many of the methods are based on flow visualisation which employ coloured liquids as tracers in "wet" tests and smoke or other visible particles in "dry" tests. Some original methods have been developed by Dedeoglu [11], Oka *et al* [12], Rizk [13], Ohigashi [14], Ohigashi [15] and Phatak [16].

Oka *et al* [12] investigated the relation between the scavenging flow of a looped two-stroke engine and its efficiency. Water in a transparent cylinder was scavenged by injection of dyed salt water. The specific gravity of the contents of the cylinder after scavenging was measured to calculate the scavenging efficiency. The authors concluded that the scavenging efficiency changes continuously with the delivery ratio, and the deterioration of scavenging efficiency was caused mainly by the short circuiting loss.

Martini and Oggero [17] employed a mixture of air and helium to simulate the burnt gases, while pure air was used as the fresh entering charge. Quantitative evaluation of the scavenging efficiency in the test was made through chemical analysis of a gas sample drawn from the cylinder at the end of the scavenging period. Reddy *et al* [18] have

measured the flow field inside a cylinder during the gas exchange period by using a motored Schnurle-type two-stroke engine and a hot-wire anemometry technique. A complete velocity field and turbulence parameter map has been generated for various operating conditions. These maps were used to study the effects of engine speed, throttle position and piston head shape.

Jante[19] proposed a technique for the improvement of the scavenging process in a particular two stroke engine cylinder. He found that the most efficient scavenging for a given cylinder can be obtained by designing the transfer ports according to tests with the cylinder head removed. The experimental apparatus described by Jante is illustrated in Fig. 2.3.

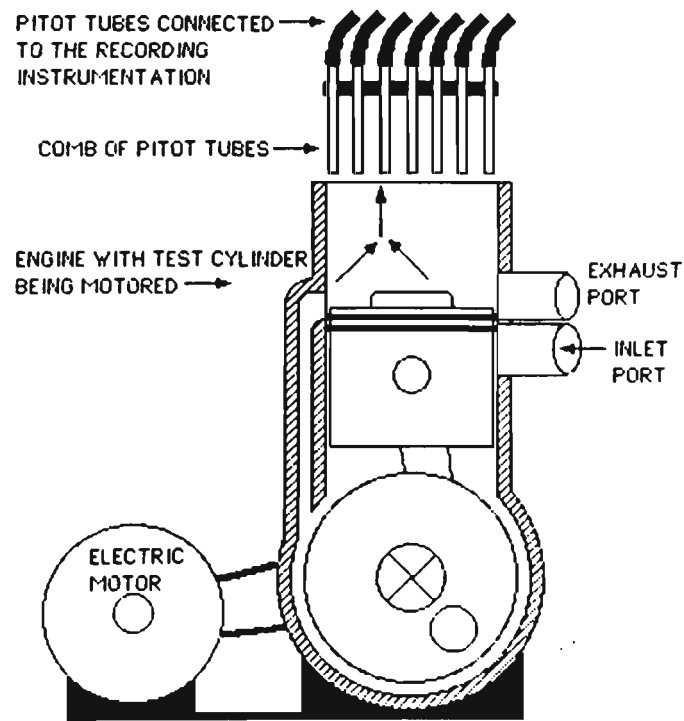


Fig. 2.3 The Jante Test Rig [8]

The engine without its cylinder head is motored at a constant speed. A number of Pitot tubes are located at the face of the cylinder head to measure the distribution of the scavenging air velocity just above the open cylinder. Based on the velocity contour so obtained, the author stated that:

"The scavenging currents must so interact with the piston crown and the cylinder wall that a stable closed rising current is obtained on the wall opposite to the exhaust ports, which has its maximum velocity at this wall and near zero velocities on the line perpendicular to plane of symmetry and the cylinder axis.", See Fig. 2.4.

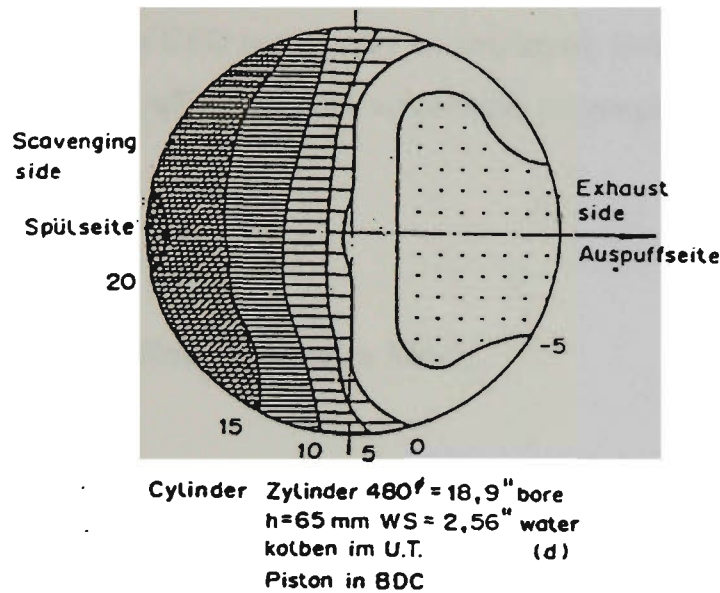


Fig. 2.4 Velocity contour of an optimum cylinder by Jante method [19]

The Jante method has proved to be an effective design tool over the past three decades and is still in use today, as reported by Ishihara *et al* [20,21,22,23]. However, this method provides no quantitative information about the constitution of the cylinder contents during the gas exchange period.

Full size firing engine tests are conducted under normal conditions of operation. Measurements of scavenging efficiency in a firing engine by exhaust gas analyses with or without a tracer have been demonstrated to be an effective research and development method by Killman *et al* [24], Hori [25] and Hashimoto *et al* [26]. The tests make it possible to study the influence of an improved port design (which is considered as having a better scavenging quality by means of static or dynamic model testing) on the overall performance of the real engine. Generally, such methods are used at the conclusion of the design phase to examine a newly developed engine cylinder.

2.3.2 Theoretical Modelling of the Scavenging Process

A reliable theoretical model of the gas exchange process in a two-stroke engine is a powerful tool for engine design and development. The optimisation of the geometry of a cylinder and ports system can be achieved with the help of a computational fluid dynamics model (CFD model). To predict the overall characteristics of a given engine under different operating conditions, a CFD model may be employed, however, a simple relation which describes the scavenging efficiency and volumetric scavenging ratio characteristics is often preferable.

2.3.2.1 Computational Fluid Dynamics Model

The best description of the scavenging process is obtained if the complete set of the partial differential equations which govern this process are solved to yield the time variation of the spatial profiles of the dependent variables, such as pressure, density, enthalpy, velocity and concentration of fresh charge, see Ahmadi-Berrui *et al*[27] and Schwarz[28]. These equations usually include the conservation laws of mass, momentum and energy, turbulence model, relations between transport coefficients and dependent variables, some additional auxiliary state equations (such as the isentropic and perfect gas laws) and the corresponding initial and boundary conditions. The CFD models are useful in providing a descriptive picture of the in-cylinder events, and identifying areas such as fresh mixture concentration, short circuiting and poorly scavenged regions for a given configuration of a cylinder and port assembly. Their applications to two-stroke engines have also led to significant progress in understanding of the gas exchange process. The optimisation of port timing and shape based on the extensive information provided by CFD models is possible and a great deal of time may be saved when compared to trial and error approaches.

A three-dimensional calculation of the flow processes in a two-stroke engine was carried by Ahmadi-Berrui *et al*[27]. It was aimed at investigating the flow and gas exchange processes under realistic operating conditions and providing a basic knowledge of the in-

cylinder flow structure and its development, as well as the influence of pressure wave oscillations in the scavenging port and exhaust port system on the in-cylinder flow processes. The cylinder has the port arrangement similar to Fig. 2.2(a). The calculation domain was confined to half the cylinder volume, partitioned by the geometrical plane of symmetry. The thermodynamic initial and the instantaneous boundary conditions in the scavenging and exhaust ports were pre-calculated by the authors using a separate unsteady gas dynamics model [29] to enable incorporation of the effect of the pressure waves which causes strong flow oscillations in the scavenge and exhaust ports. The instantaneous mass flows for the individual scavenging ports were proportional to their flow areas. Uniform and plug flow were assumed for time-dependent velocities and mass flow rates of the inflow streams at the scavenging ports. The main findings of the work were:

- (1). The basic in-cylinder flow structure, established early during the scavenging phase, comprises a three dimensional "loop" flow, Fig. 2.5(a), and a pair of toroidal vortices shown in Fig. 2.5(b).

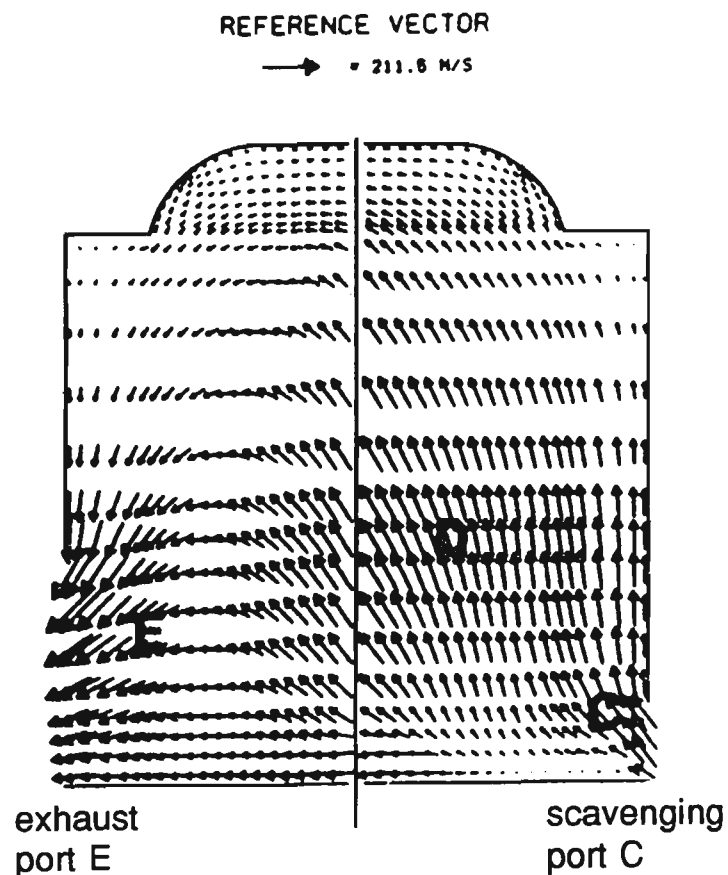
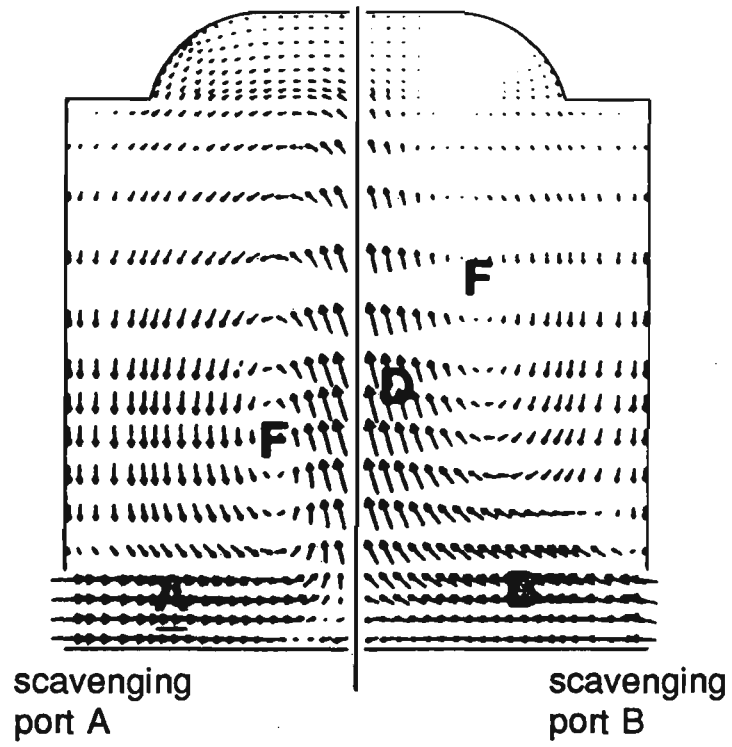
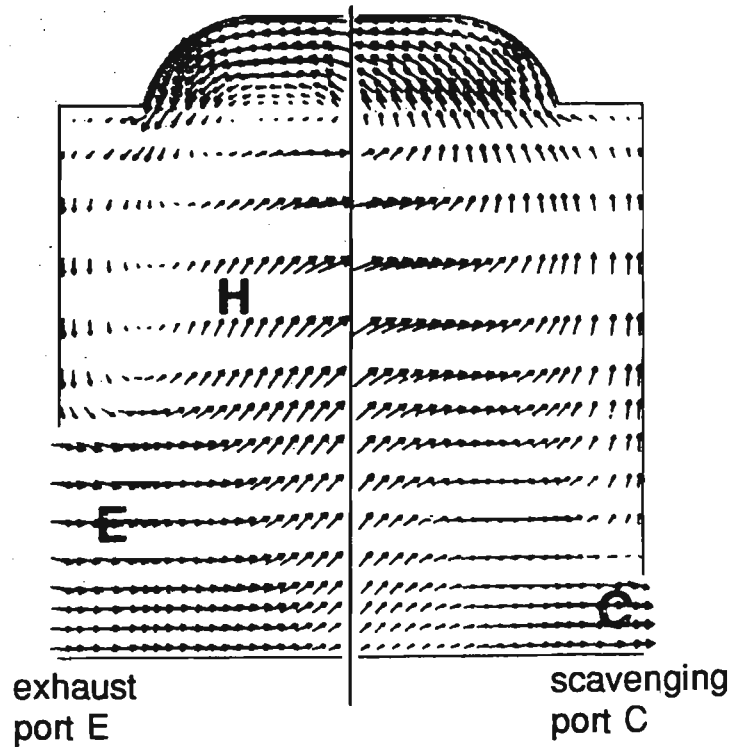


Fig. 2.5(a)



(b)

→ = 195.9 M/S



(c)

Fig. 2.5 In-cylinder velocity field at various crank angles
 (a)(b): at 145° crank angle; (c): at 215° crank angle

- (2). The vortex structure was responsible for the impairment of the scavenging efficiency.
- (3). The flow and the scavenging process were markedly affected by the pressure wave oscillations in the scavenging system, Fig. 2.5(c). The in-cylinder flow structure and charge distribution pattern established during the normal scavenging phase were significantly altered as a result of the oscillations of the intake and exhaust mass charge and discharge.

Recent research efforts using laser doppler velocimetry (LDV), for example, by Smyth *et al* [30] have found that the direction of inflow jets, particularly for the main transfer ports, deviated from the design direction of the port such that the plug flow assumption was inadequate. Moreover, the thermodynamic properties in the cylinder and at the ports (first node in pipes) were closely interdependent. Therefore, a better way to conduct this simulation is to execute iteratively the unsteady gas-dynamics program and the CFD program, that is, at each time step, solve the coupled in-cylinder equations and port boundary equations given by the pipe flow model. This may be computational intensive and would be prohibitive in terms of run time on anything other than a supercomputer.

2.3.2.2 Simple Theoretical Scavenging Model

Although a detailed computational fluid dynamics model can provide extensive information about in-cylinder flow patterns, the computation time for such a simulation can be huge. Therefore, such a model is considered impractical for engine modellers who wish to predict the overall performance characteristics of a given engine configuration under different operating conditions. For the later purpose, the relatively simple theoretical model which correlates the scavenging efficiency η_s against the volumetric scavenging ratio λ_s (or other similar parameters) is preferable.

The η_s - λ_s characteristics globally characterise the success of the scavenging process. For a given λ_s , the higher the η_s , the better the scavenging. The relationship is obtained based

on the assumptions that the replacement of products of combustion can be modelled by so called displacement scavenging, mixing scavenging, or a combination of both. In addition, some of the fresh air-fuel mixture may directly by-pass through the cylinder into the exhaust pipe and be wasted (short-circuiting). The following scavenging models can be found in literature.

(1) Perfect Displacement Model:

The idealised perfect displacement model apparently conceived by Hopkinson as stated by Blair[8] implies that the products of combustion are completely replaced by the fresh charge under constant cylinder volume, temperature and pressure, and there is no escape of fresh charge through the exhaust port. It is the upper bound efficiency for the scavenging process and the real process is never as efficient.

(2) Perfect Mixing Model:

The second notion conceived by Hopkinson about the way the cylinder was scavenged was perfect mixing. In a perfect mixing model, the scavenging process also occurs at constant cylinder volume and pressure. As the fresh charge enters the cylinder via the transfer ports, it is assumed that it instantaneously mixes with the cylinder contents to form a homogeneous mixture. The exhaust gas is therefore a mixture of combustible waste and fresh charge. For a modern two-stroke engine, the perfect mixing model underestimates the scavenging performance. However, it is still frequently quoted as a reference for comparison. Fig. 2.6 shows the $\eta_s - \lambda_s$ characteristics for perfect displacement and perfect mixing scavenging.

(3) The Combined Models:

Both perfect scavenging models are very simple to use but are not realistic.

Experimental modelling of the scavenging process using flow visualisation rigs by Dedeoglu [11] and Sher [31] revealed that the scavenging process may be depicted as proceeding in two or three principal phases: displacement, mixing and short-circuiting. Consideration of the actual process of scavenging led to the development of the multi-zone model. In such models the cylinder is subdivided into two, three or more zones. Fresh charge, burnt gas and the mixture of fresh charge and burnt gas occupies different zones. Some notable multi-zone models are: the isothermal two-zone model of Maekawa[32], the two-zone model of Benson and Brandham[33], the "S" shape model of Sher[34], and the scavenging model of Blair[8].

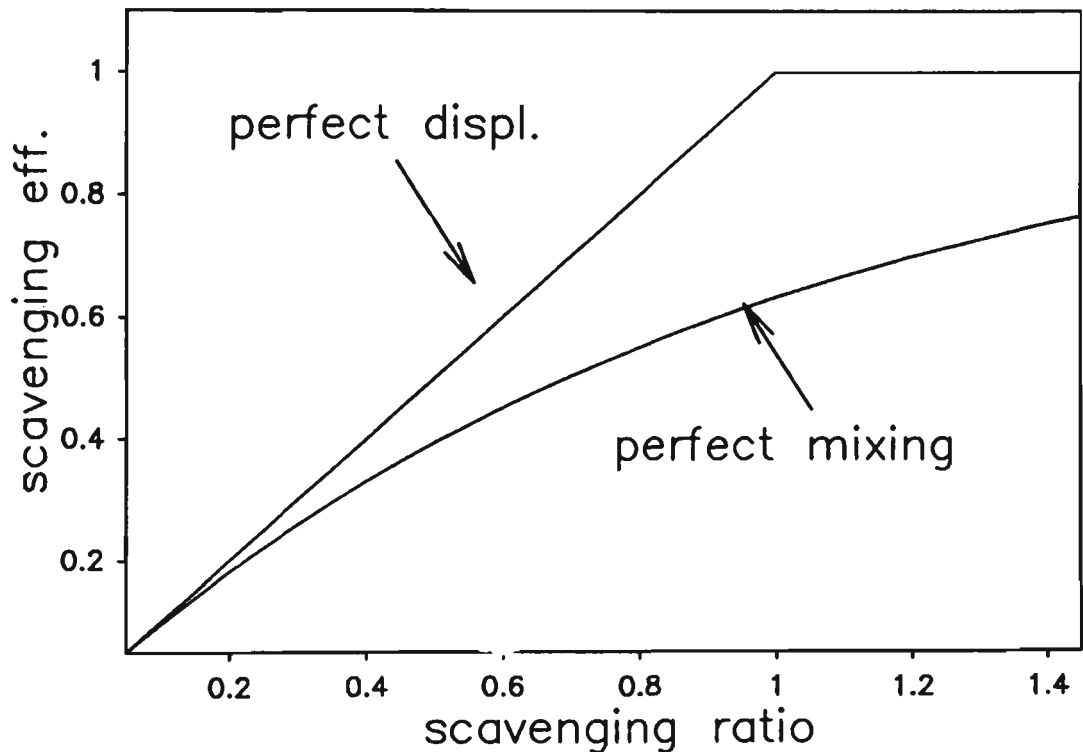


Fig. 2.6 $\eta_s - \lambda_s$ Characteristics for perfect scavenging

The Benson-Brandham model assumes the scavenging process occurs at a constant cylinder volume, pressure and temperature conditions. The fresh charge is assumed to split into two parts while it enters the cylinder via scavenging ports: one part to perfectly displace the burnt gas, and the other part to be directly short-circuited to the exhaust port.

When the volumetric scavenging ratio reaches a certain level, the undiluted fresh charge in the perfect displacement zone together with the incoming stream of fresh charge instantaneously mix with the remaining burnt gas in the cylinder to form a homogeneous mixture. The substance directed to the exhaust port is switched from pure burnt gas to this homogeneous mixture. The resulting scavenging efficiency-scavenging ratio relation is:

$$\eta_s = 1 - (1-x)\exp\{x - (1-y)\lambda\} \quad (2.9)$$

where x - the scavenging ratio at the transition point

y - the proportion of short-circuiting

λ_s - the scavenging ratio

η_s - the scavenging efficiency

Re-arranging equation (2.9) gives:

$$\ln(1 - \eta_s) = (y-1)\lambda + \ln(1-x) + x \quad (2.10)$$

This equation represents a straight line in the $\ln(1-\eta_s) - \lambda_s$ plane. The slope is $(y-1)$ and the intercept is $\ln(1-x)+x$. In Benson's model, it is apparent that the slope $(y-1)$ could not be less than -1 , as that would produce a negative value of short circuiting ratio y , which is physically impossible.

The experimental justification for such classical scavenging models is scant. Information of this kind was not available until the 1980's and probably the most appropriate experiments were conducted by researchers [8,22,35,36] at The Queen's University of Belfast (QUB) on the single cycle engine test rig. The concept of single cycle testing was first conceived by Sammons [37] in 1949 but was revived at QUB in the 1980's with significant modifications. The salient features of this apparatus are: the cylinder volume and the crankcase volume remains constant during its operation for one cycle from TDC to TDC at a known speed. The rig allows the scavenging process in a tested cylinder to be similar to what the theoretical assumptions of scavenging prescribe, that is, a constant volume, isobaric and isothermal process. As a consequence, the QUB single cycle gas scavenging

apparatus is able to provide verification of all theoretical scavenging models which are postulated under the constant volume, isobaric and isothermal assumption. More information on the QUB single cycle test rig may be found in Appendix A.

Blair *et al* [38] did extensive investigations on modelling the scavenging process with the aid of the single cycle gas scavenging rig. By means of measurements of the scavenging characteristics of a number of testing cylinders, the authors concluded that the measured scavenging efficiencies and scavenging ratios, when plotted as $\ln(1-\eta_s)$ vs. λ_s , do fall on straight lines. However, the slopes of these straight lines are all less than -1, which is in conflict with the Benson-Brandham theory. Moreover, the better the scavenging, the closer the value is to -2. This 1988 finding demonstrates that the Benson-Brandham scavenging model fails to correlate with relevant experiments. The reason is that the "step change" assumptions are not realistic in real scavenging processes.

The "S" shape scavenging model developed by Sher[34] is based on the observation, that the plot of mass fraction of fresh charge being detected in the exhaust gas passing through the exhaust port versus time, exhibits a "S" shape curve. By using an exponential function to fit this "S" shape curve, a mathematical relation for scavenging efficiency was derived. The model interprets the scavenging process as a superposition of a perfect displacement and a charging loss. Examination of the scavenging process in flow visualisation rigs revealed that there was no occurrence of an abrupt transition from one phase to another(step change), but rather a complex combination of the perfect displacement, perfect mixing and short-circuiting. Introducing a term which accounts for charging loss gives a more realistic correlation.

After the experimental refutation of the Benson-Brandham model, Blair [38] also discarded the step change characteristic which was a feature of earlier theoretical scavenging models. Blair allowed the scavenging process to evolve in a continuous way from the beginning to the end, to ensure the model contained the necessary elements of perfect displacement, mixing and short-circuiting. The model is based on the assumption that the scavenging process is conducted on a volumetric basis, following Dedeoglu [39]. That is, the replacement of volumes of exhaust gas by volumes of fresh charge. The

variation of the proportions of perfect scavenging and short-circuiting are regarded as functions of scavenging ratio. At any given level of scavenging ratio, a certain amount of the increment of the entering fresh charge is going to be short-circuited, while the remainder of the entering fresh charge goes into the perfect scavenging volume. For the charge which enters the perfect scavenging volume, a proportion of the total stays, and the rest joins the perfect mixing zone.

The ratio of the short-circuiting, perfect displacement and perfect mixing of the entering fresh charge increment are supposed to vary linearly as the scavenging ratio increases. The calculation proceeds to enter fresh charge volume increment as 1, up to any desired maximum value, with the cylinder volume set at 1000. The volumetric distributions of each distinctive portion are traced and accumulated at the end of every charging step. The resulting instantaneous scavenging efficiency and trapping efficiency are therefore based on these quantities.

According to the author, the model is relatively simple to "tune" for a particular engine cylinder, as there are usually only two parameters to be manipulated in order to achieve a good correlation with experiment. The model, after the correlation is achieved, provides preliminary information regarding the relative contributions of perfect displacement, perfect mixing or short-circuiting during the scavenging period for a tested cylinder. It is also interesting to note that by using Blair's model, the predicted exhaust gas purity versus time for different cylinders whose scavenging qualities have been ranked by experiments, show a more or less "S" shape profile, the more "S" like the profile the better the scavenging is, which is in line with Sher's finding described above.

In the preceding paragraphs, some theoretical models of the scavenging process have been reviewed. These models, depending on their different underlying assumptions, describe how a particular type of engine cylinder is scavenged under different operating conditions. The single cycle apparatus at QUB provided important experimental verification of such models. The accurate prediction of two-stroke engine performance as well as engine design is very dependent on the degree of success of the theoretical simulation of the scavenging process.

2.4 Improvement of the Scavenging Process

The ideal scavenging process for a simple naturally aspirated, crankcase-scavenged two-stroke engine has already been described as the perfect displacement process in which the entering fresh charge acts as a piston to push the burnt gases out of the cylinder without actually mixing with them and no fresh charge escapes from the exhaust port. However a carburetted two-stroke engine loses between 15% -20% of the fuel under normal operating conditions, Sher [2].

This is attributed to the fresh charge short-circuiting to the exhaust and back flow through the inlet and transfer ports. It results in high hydrocarbon emission levels, poor fuel economy, low performance figures and a wide spread of cycle to cycle variation. As the port timing and the pulsating effect of pressure waves in the intake and exhaust system are optimised to offer the best match with the engine at some well defined operating condition, the occurrence of short-circuiting, back flow and leakage through the exhaust port may have significant deleterious effects at off-design engine speeds or partial-open-throttle positions. It causes reduced engine performance characteristics, worse fuel economy and higher emission levels.

To overcome these shortcomings of the two-stroke engine, many approaches have been proposed. Among these, the non-symmetrical arrangement of the port timing has proved to be one of the more effective. The introduction of direct fuel injection systems and multi-stage scavenging activity also produces positive results.

2.4.1 Non-symmetric Port Timing

The installation of a reed valve, a rotary disk valve, a fluid diode or a scroll diode on the inlet or transfer port have been reported. A fluid diode is a chamber with no moving parts which allows fluid to pass through it with a relatively low pressure drop in the forward direction and a relatively higher resistance when the flow direction reverses. The higher resistance is produced due to the particular geometry of the chamber which permits

vorticity development. Nagao, *et al* [41] examined experimentally the presence of the scroll diode and the vortex diode at the inlet port on a motored engine. They claimed that the delivery ratio was increased considerably at low engine speeds with the installation of a scroll diode. The scroll diode was found to be more effective than the other types of diodes. Sher[42] studied the performance characteristic of a fired two-stroke engine with a scroll diode at the inlet port and found the engine torque was impressively improved by 30% at low engine speeds, while it deteriorated , by 20%, at higher engine speeds. A possible cause is that the diode generates high forward resistance at higher engine speeds and the delivery ratio consequently deteriorates.

A scroll diode was also installed in the scavenging port by Sher[43], and the influence of the diode presence on the engine performance was examined under the fired condition test. The torque curve becomes flatter while its maximum value appears slightly above the original curve at the same engine speeds. The improvement in the engine power achieved with the diode seems to be most significant near the lower and higher limits of the engine speeds. The increment may be high as 20%. A close examination of the cylinder and crankcase pressure history shows that at low engine speeds, the crankcase pressure is higher than the cylinder pressure at TPO, and the burnt gases are scavenged through the exhaust port by the fresh charge.

When the piston passes the BDC and moves upward, the crankcase volume increases while the pressure there is already low. The back flow from the cylinder to the crankcase through the transfer port in a simple engine occurs when the crankcase pressure is lower than the cylinder pressure. Consequently, the crankcase pressure may reach a higher value at TPC. With a scroll diode located at the transfer ports, the crankcase pressure record shows that the pressure at TPC remains at a lower value, which means that a back flow has been suppressed. At high engine speeds, the pressure inside the cylinder at TPO is still high and the crankcase pressure in a simple engine increases steeply due to the back flow, while in the diode-installed engine the crankcase pressure increases moderately which suggests that the backward flow has been reduced.

A simple and effective means to boost the performance of a crankcase-compressed, loop-

scavenged, two-stroke engine under off-design conditions is to control the pressure at the exhaust port by changing the exhaust pipe configuration. Dynamically, controlling the exhaust pressure at the port has a similar effect to modification of the port timing device, so an improved scavenging quality is achieved by the introduction of non-symmetric port timing. Changing the dimension of a particular section of the exhaust pipe is found to be an effective and practical method to improve two-stroke engine performance characteristics under off-design conditions. Fig. 2.7 depicts such an exhaust system.

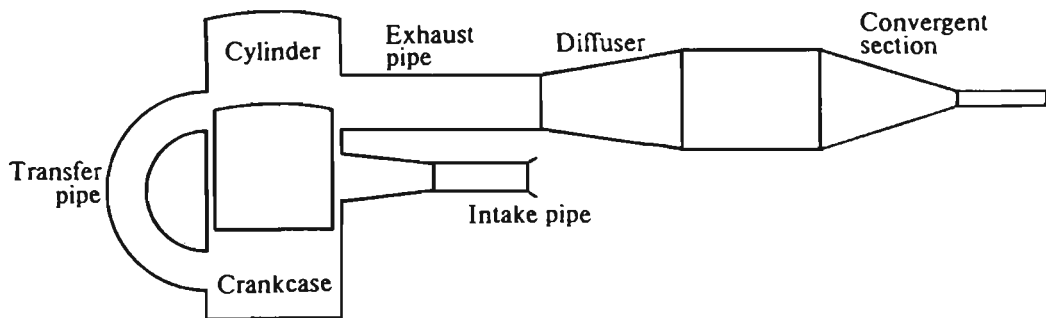


Fig. 2.7 An extendable exhaust configuration

When the exhaust port opens a pressure wave is transmitted down the exhaust pipe. This pulse is partially reflected by the diffuser as a negative (expansion) wave and partially transmitted. The expansion wave, on reaching the exhaust port, will assist scavenging of the cylinder by "drawing" gas through the exhaust ports. The transmitted pressure wave will eventually reach the converging section of the exhaust pipe and will be partially reflected and partially transmitted to atmosphere. The reflected positive (compression) pressure wave arrives back at the exhaust port to create a "blocking effect" in the TPC-EPC period. The working principle described, being translated into the pressure history at the exhaust port, is illustrated in Fig. 2.8.

Clearly a particular geometry will be optimal for only one engine speed, so it is necessary to change the geometry for optimal performance at different speeds. The extendable pipe ensures that the effect of pulsating pressure waves described above can be utilised for

various operating conditions. Detailed theoretical and experimental studies of an extendable exhaust constitute the core of this project and are presented in later chapters.

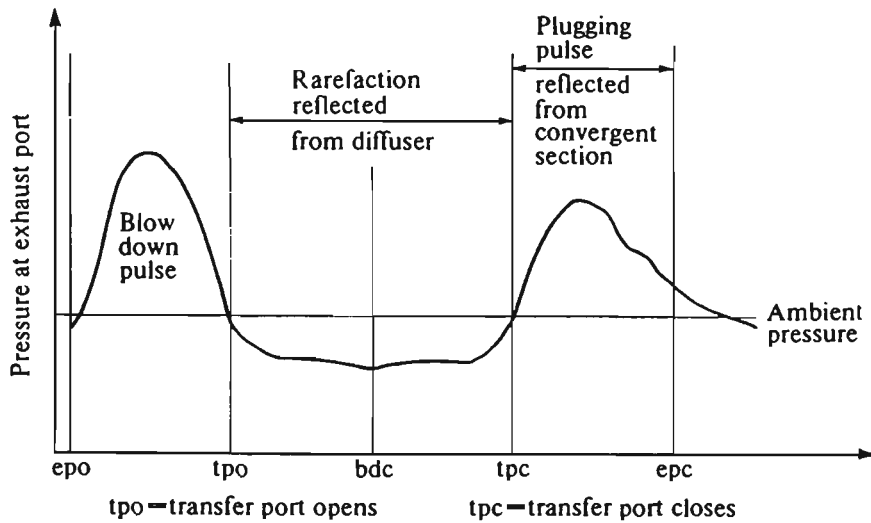


Fig. 2.8 Ideal dynamic pressure history at exhaust port [44]

2.4.2 Stratified Charging

Several other attempts have been made to overcome the drawbacks of a two-stroke engine by considering that the scavenging process should be carried out fully or at least partially with air alone instead of an air-fuel mixture. For this, efforts have been made in two parallel directions: the introduction of fuel by an injection system and the multi-staging of scavenging.

Studies carried out using fuel injection systems include in-cylinder direct injection, low pressure injection in transfer port or inside cylinder. More recently, pneumatic fuel injection systems have also been developed. These injection systems have produced large reductions in fuel consumption and emissions. However, they usually increase the production costs. New concept multi-stage scavenging systems layouts have been developed for carburettor-induced engines. In such systems, scavenging the cylinder

proceeds in two steps: the fresh air replaces the combustible products and then the fresh fuel-air mixture fills the cylinder. Considerable reduction in fuel consumption and exhaust emissions have been reported by employing such systems.

Fresh charge losses can be reduced by the selective exhaust gas recirculation (SEGR) method, developed by Saxena [45]. Investigations of fresh charge losses in the exhaust port showed that the HC concentration history decreases during the initial period of scavenging and the deepest trough appears between TPO and BDC. It then increases to a maximum level and practically remains constant around top-dead-centre or during the exhaust port closure. The SEGR method is based on this effect where the portion of the exhaust gases corresponding to the period it contains maximum HC concentration can be recirculated to aid scavenging the cylinder. As this period corresponds to the induction phase of engine operation, the crankcase suction can be used to draw this high HC concentration exhaust gas near the exhaust port. The induction system of the SEGR engine consists of two circuits. The primary circuit is similar to that of the conventional engine and supplies carburetted air-fuel mixture. The secondary circuit consists of a probe in the exhaust port connected to the upper part of the transfer passage through a reed-valve.

The operating principle of SEGR is: during the scavenging process, the recirculated exhaust gas enters the cylinder first and briefly scavenges the cylinder, and the fresh mixture from the crankcase flows to the transfer ports and starts to charge the cylinder subsequently. The influence of SEGR on emission and brake specific fuel consumption (BSFC) is quite pronounced. A reduction of 34% on HC emission and 12% on BSFC has been claimed. However, as the performance of a SEGR engine is dependent on the recirculation ratio, the air-fuel ratio, and the spark advance (due to the higher exhaust residual found at the commencement of compression), the SEGR system is not only complex in structure, but also complicated in operation.

Since the scavenging process is a volumetric process in which the incoming fresh air volume displaces the same volume of exhaust through the exhaust port, a higher scavenging air volume will therefore lead to better scavenging of the cylinder. In other

words, the scavenging air volume is an important factor in successful scavenging of the cylinder. This observation leads to the idea that the temperature of the fresh charge can be increased in order to obtain a better scavenging efficiency. However, the lowered density implies that less fresh charge will be trapped in the cylinder when the compression commences. Dedeoglu *et al*[39] suggested a two-stage scavenging model to improve the overall engine efficiency.

In the first stage of the scavenging process, a certain portion of the charge is warmed in a heat exchanger by exhaust gas as it is led into the cylinder. The charge expands in the cylinder and results in better scavenging. In the second stage, the rest of the high density scavenging air is then used to fill the cylinder. This results in a higher trapped mass. The authors reported that by using this two-stage scavenging system, the overall scavenging efficiency could be improved by 3 - 5%. The temperature of the cylinder contents increased by 8 - 22°C, which aids in more effective combustion.

CHAPTER 3

THEORETICAL CONSIDERATIONS AND DEVELOPMENT OF MODELLING A TWO-STROKE ENGINE

3.1 Introduction

Successful numerical modelling of a two-stroke internal combustion engine is highly dependent upon being able to model the compressible gas flows in the intake, transfer and exhaust pipes. As the timing of pressure wave arrival and departure at the exhaust port is critical to the performance of an engine equipped with a "tuned" exhaust pipe, an accurate model of the gas flow in this pipe is essential. Wallace *et al* [40,46], Benson [47] and Blair *et al* [8,48,49] have investigated this problem and concluded that quasi-one dimensional gas flow models which assume slowly varying pipe cross section and isentropic conditions are adequate.

Although pipe friction and heat transfer through the wall of the pipe are present, these effects are small by comparison with energy transport in the flow direction (especially when the pipe wall is insulated) and have been neglected in many previous studies. This study will make the same assumptions. In this chapter, the equations which govern such a flow are formulated and the solution procedures are derived. Different schemes to evaluate the variation of Riemann variables along the characteristic curves are proposed. Efforts are also made to properly evaluate the pressure wave reflection at engine port/pipe boundaries.

3.2 Fundamentals of Pressure Wave Theory

3.2.1 Basic Concepts

When the surrounding medium such as a gas, is disturbed, a pressure wave is generated. The disturbance then travels at the local velocity of sound (usually in the order of 300 -

500 m/s) through the surrounding gas, in general suffering reflection, rarefaction and attenuation. An example of a pressure wave (the propagation of a physical disturbance) is a sound wave (acoustic pressure wave), where the pressure amplitude of the wave is very small. Any pressure wave with a pressure amplitude greater than an acoustic wave is classified as finite amplitude wave. Its magnitude is often measured by two dimensionless parameters, namely:

Pressure ratio:

$$\Psi = \frac{p}{p_0} \quad (3.1)$$

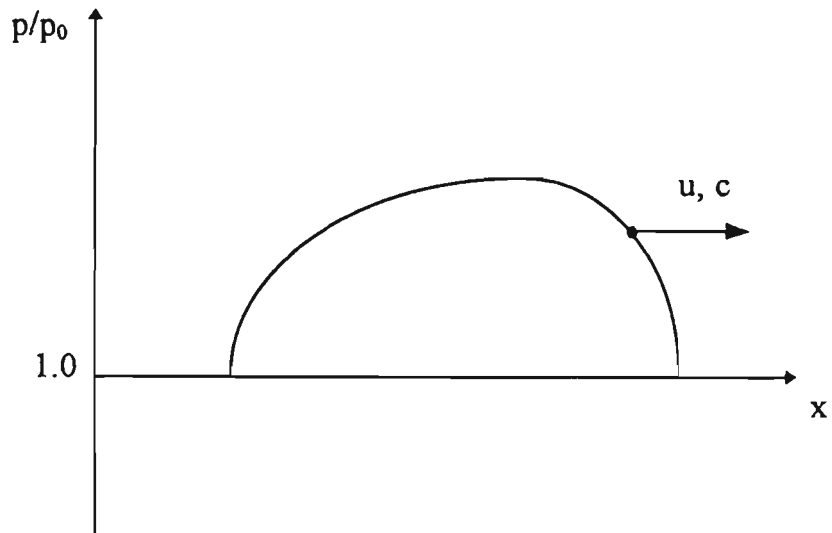
and pressure amplitude ratio:

$$X = \left(\frac{p}{p_0} \right)^{\frac{\gamma-1}{2\gamma}} \quad (3.2)$$

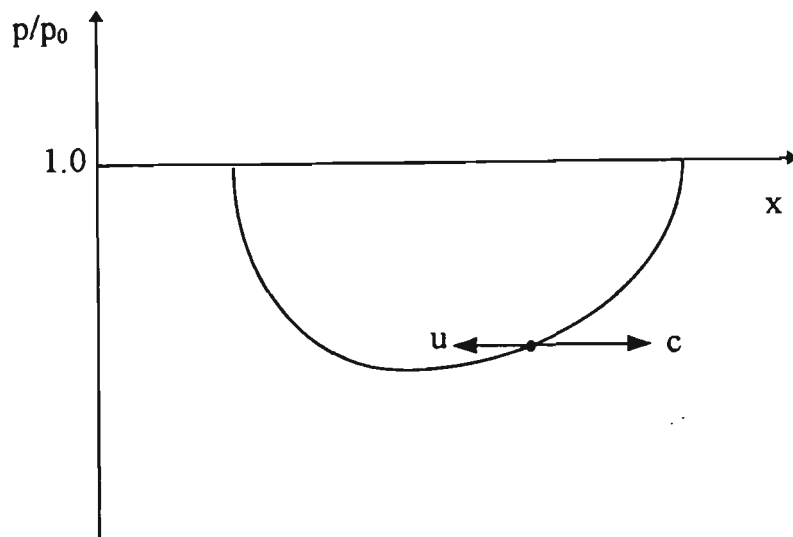
where p is the pressure at the point under consideration, p_0 is the undisturbed or reference pressure and γ is the specific heat ratio of the gas.

Two types of pressure wave exist: compression waves and expansion waves. A compression wave occurs when the pressure ratio Ψ is greater than 1 everywhere on the wave. The gas particle is moving in the same direction as the wave being propagated. An expansion wave exists when the pressure ratio Ψ is less than 1 everywhere on the wave. The gas particle is moving in the opposite direction to the direction of wave propagation. Fig. 3.1 illustrates both types of wave profiles. A wave profile is obtained by taking the pressure ratio Ψ at different values of distance x along the pipe at a fixed time.

In a two-stroke engine cylinder, the exposure of the exhaust port by the downward moving piston results in the release of high pressure gas. A compression wave of finite amplitude is then generated and propagates along the exhaust pipe. When this wave passes through the supporting medium (here the gas), it will enter the medium with a velocity u and will change the local thermodynamic properties of the gas as well. The gas particle velocity obtained from the pressure wave motion induces a local mass flow m . This mass



a) Compression wave propagates rightward



b) Expansion wave propagates rightward

Fig. 3.1 A pressure wave profile

flow forces the exhaust gas out of the exhaust pipe. When a single plane finite amplitude compression pressure wave with pressure p and density ρ enters a pipe containing gas at

reference pressure p_0 and density ρ_0 , Bannister [50] has shown that the gas particle velocity u is:

$$u = \frac{2}{\gamma-1} a_0 (X - 1) \quad (3.3)$$

where

a_0 - the reference sound velocity

$$a_0 = \sqrt{\gamma R T_0} \quad (3.4)$$

T_0 - reference temperature

X - pressure amplitude ratio

γ - specific heat ratio of gas

R - characteristic gas constant

The wave propagation velocity c :

$$c = \frac{a_0}{\gamma-1} \{(\gamma+1)X - 2\} \quad (3.5)$$

Local sound velocity:

$$\begin{aligned} a &= a_0 \sqrt{\frac{T}{T_0}} \\ &= a_0 \left(\frac{P}{P_0} \right)^{\frac{\gamma-1}{2\gamma}} = a_0 X \end{aligned} \quad (3.6)$$

Local gas density:

$$\rho = \rho_0 \left(\frac{P}{P_0} \right)^{\frac{1}{\gamma}} = \rho_0 X^{\frac{2}{\gamma-1}} \quad (3.7)$$

In Equation (3.7), ρ_0 is the reference gas density, where:

$$\rho_0 = \frac{P_0}{RT_0} \quad (3.8)$$

Local mass flow rate:

$$\dot{m} = \rho u A = u A \left(\rho_0 X^{\frac{2}{\gamma-1}} \right) \quad (3.9)$$

where A represents the flow passage area.

Local gas particle Mach number:

$$M = \frac{u}{a} = \frac{u}{a_0 X} \quad (3.10)$$

Equations (3.3)~(3.10) are identically applicable to an expansion wave. The negative sign of the gas particle velocity u (equation 3.3), as a result of $X < 1$, only signifies that the particle is moving oppositely to the wave propagation direction.

3.2.2 Superposition of Pressure Waves

As the outward moving exhaust pulse (compression pressure wave) arrives at the pipe exit, wave reflection occurs. The reflected pressure wave reverses its direction of propagation and will superimpose on the continuously outward running exhaust pulse. The reflections of pressure waves also occur at port/pipe interfaces and at any change of pipe diameter. Therefore at virtually all times except the very first cycle of engine operation, where the gas in the exhaust pipe is undisturbed, pressure waves propagate to and fro through each other because of wave reflections.

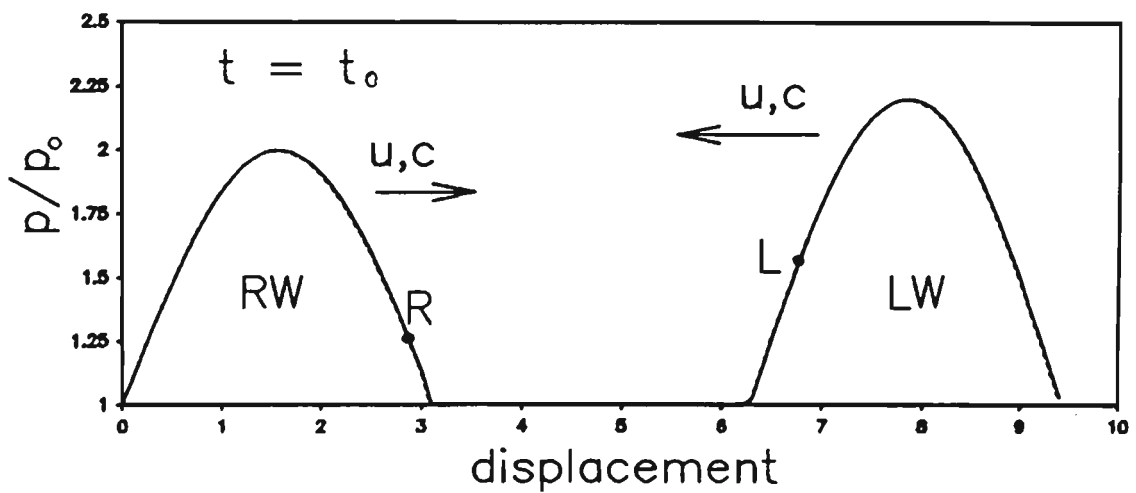
For the two imaginary observers R and L sitting on two oppositely moving pressure waves RW and LW in a one-dimensional flow passage, say, a pipe, Fig. 3.2(a) depicts two waves before superposition and Fig. 3.2(b) during superposition. Before superposition,

considering simple waves RW and LW, the gas particle velocity at point R on wave RW, and the particle velocity at point L on wave LW, are, from equation (3.3) :

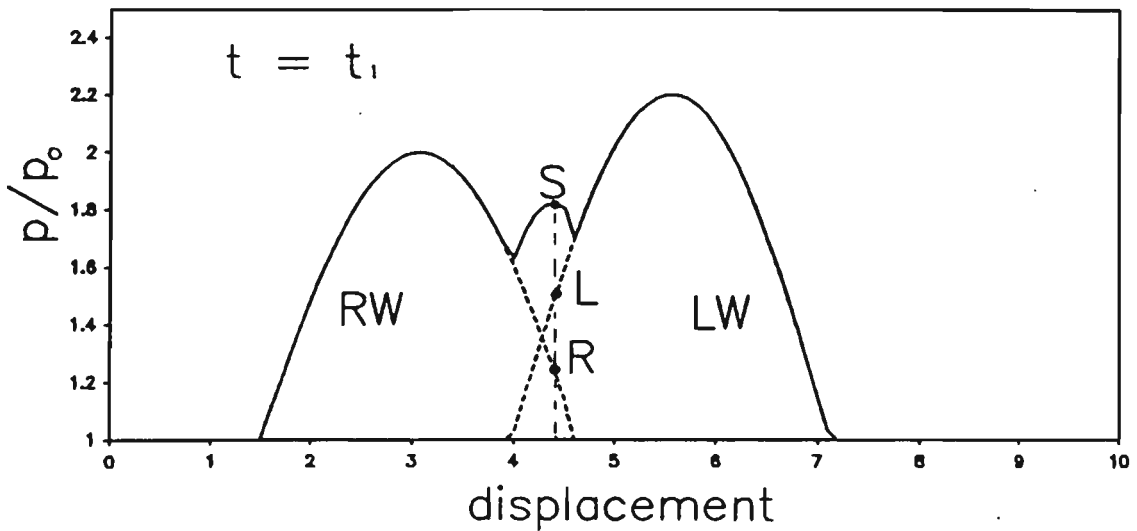
$$u_{R,E} = \frac{2a_0}{\gamma-1} \cdot (X_R - 1)$$

$$u_{L,E} = -\frac{2a_0}{\gamma-1} \cdot (X_L - 1)$$

Subscript E (earth) denotes that such velocity is relative to the stationary pipe wall, that is, absolute velocity.



(a) Before superposition



(b) During superposition

Fig. 3.2 Superposition of pressure waves

Suppose points R and L are now coincident during superposition. The observer R who moves with wave point R, upon entering the wave LW, will move with a velocity relative to observer L (who is sitting on wave point L), denoted as $u_{R,L}$,

$$u_{R,L} = \frac{2a_L}{\gamma-1} \left[\left(\frac{p_s}{p_L} \right)^{\frac{\gamma-1}{2\gamma}} - 1 \right] = \frac{2a_0}{\gamma-1} (X_s - X_L) \quad (3.11)$$

where p_s is the superposition pressure.

Superposition velocity (absolute velocity) at point R, $u_{(R,E)s}$, becomes the summation of $u_{R,L}$ and $u_{L,E}$:

$$\begin{aligned} u_{(R,E)s} &= u_{R,L} + u_{L,E} \\ &= \frac{2a_0}{\gamma-1} (X_s - X_L) - \frac{2a_0}{\gamma-1} (X_L - 1) \\ &= \frac{2a_0}{\gamma-1} (X_s - 2X_L + 1) \end{aligned} \quad (3.12)$$

Similarly, observer L who sits on wave point L is entering wave (RW) and will travel with a velocity relative to observer R on wave point R, $u_{L,R}$, during the superposition

$$\begin{aligned} u_{L,R} &= -\frac{2a_R}{\gamma-1} \left[\left(\frac{p_s}{p_R} \right)^{\frac{\gamma-1}{2\gamma}} - 1 \right] \\ &= -\frac{2a_0}{\gamma-1} (X_s - X_R) \end{aligned} \quad (3.13)$$

The superposition velocity at point L, $u_{(L,E)s}$, is therefore:

$$\begin{aligned} u_{(L,E)s} &= u_{L,R} + u_{R,E} \\ &= -\frac{2a_0}{\gamma-1} (X_s - X_R) + \frac{2a_0}{\gamma-1} (X_R - 1) \\ &= \frac{2a_0}{\gamma-1} (-X_s + 2X_R - 1) \end{aligned} \quad (3.14)$$

As point R and point L from wave RW and LW respectively are now coincident, $u_{(R,E)s}$ must be equal to $u_{(L,E)s}$. Equating equations (3.12) and (3.14) gives the superposition

pressure amplitude ratio, X_s :

$$X_s = X_R + X_L - 1 \quad (3.15)$$

Substituting equation (3.15) into (3.12) gives the superposition particle velocity, u

$$\begin{aligned} u &= \frac{2a_0}{\gamma-1}(X_R - X_L) \\ &= u_{R,E} + u_{L,E} \\ &= u_{(R,E)s} = u_{(L,E)s} \end{aligned} \quad (3.16)$$

that is, the particle velocities can be directly summed up to obtain the superposition particle velocity during wave superposition.

The absolute velocity of propagation of point R during superposition becomes the sum of the local acoustic and particle velocities corresponding to X_s ,

$$\begin{aligned} c_R &= a + u \\ &= a_0 X_s + \frac{2a_0}{\gamma-1}(X_R - X_L) \quad \text{to right} \quad (3.17) \\ &= a_0 \left[\left(\frac{\gamma+1}{\gamma-1} \right) X_R + \left(\frac{\gamma-3}{\gamma-1} \right) X_L - 1 \right] \end{aligned}$$

Similarly, for point L:

$$\begin{aligned} c_L &= -a + u \\ &= -a_0 X_s + \frac{2a_0}{\gamma-1}(X_R - X_L) \quad \text{to left} \quad (3.18) \\ &= -a_0 \left[\left(\frac{\gamma+1}{\gamma-1} \right) X_L + \left(\frac{\gamma-3}{\gamma-1} \right) X_R - 1 \right] \end{aligned}$$

3.2.3 Reflection of Pressure Wave at Port/Pipe Boundary

The release of high pressure gas from the engine cylinder through the exhaust port gives

rise to a pressure pulse which is reflected at the open end of the exhaust pipe and returns to the port as a rarefaction wave or scavenging wave. The arrival of this rarefaction wave at the exhaust port, if it takes place before port closure, leads to renewed discharge of gas from the cylinder, where a pronounced pressure drop occurs as a result. At the same time the rarefaction wave is reflected at the port with the port acting as a partially open or closed end. Fig. 3.3 illustrates such a pressure wave reflection process in an exhaust pipe. The arrival and the reflected outgoing waves have pressure ratios p_i/p_0 and p_r/p_0 , respectively.

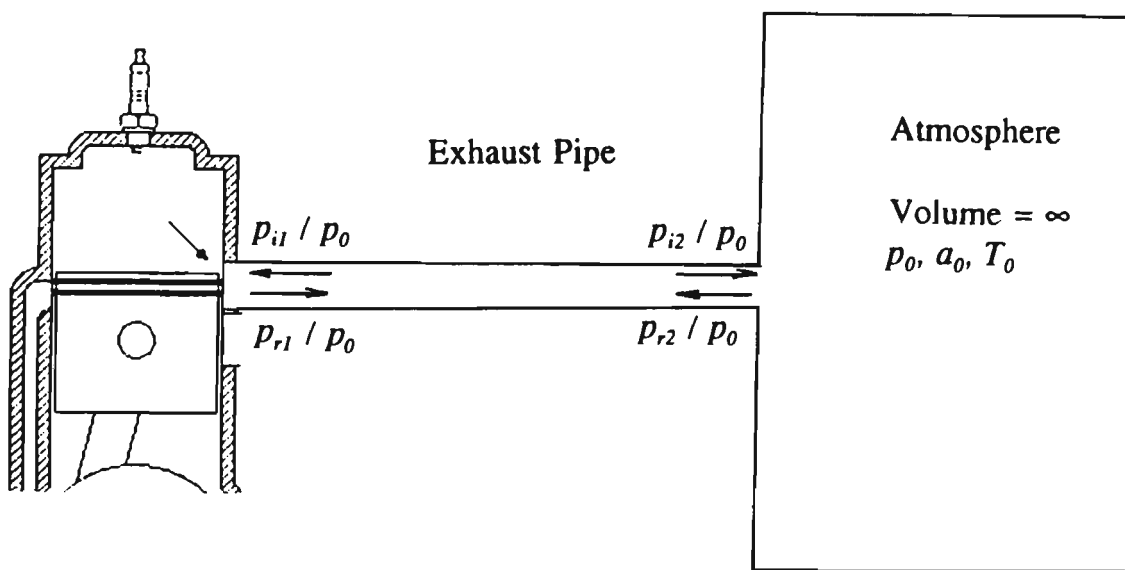


Fig. 3.3 Reflection of pressure wave at pipe boundary

The flow through the two-stroke engine ports may be analysed on a steady-flow basis. This is because of the fact that the local changes of pressure, density and velocity at the ports are very large compared with changes in time. The partial derivatives with respect to distance are much larger than the corresponding partial derivatives with respect to time. Therefore the time derivative may be neglected and the flow process can be considered as one dimensional and steady.

In order to determine the magnitude of the pressure wave reflection at the engine ports, Wallace [44] has formulated the governing equations for flows passing through the engine

port/pipe interface. By applying the fundamental laws of continuity, momentum and energy and taking the different pressure assumptions at the vena contracta, four sets of equations are derived for the four distinctive flow situations, namely the subsonic outflow, the subsonic inflow, the sonic outflow and the sonic inflow. The solutions of these equations shows that the magnitude of the reflected pressure wave, p_r/p_0 (X_r/X_0), is dependent on two independent parameters, namely,

(1). the group:

$$B = \frac{2 \left(\frac{P_t}{P_0} \right)^{\frac{\gamma-1}{2\gamma}} - 1}{\left(\frac{P_1}{P_0} \right)^{\frac{\gamma-1}{2\gamma}}}$$

or

$$B = \frac{2X_t - 1}{X_1}$$

(2). the instantaneous effective port/pipe area ratio k .

p_1 and p correspond to the instantaneous cylinder pressure and incident wave pressure, respectively.

For the flow at the pipe exit, the atmosphere may be considered as a cylinder with infinite volume. B is thus reduced to:

$$B = 2X_t - 1$$

and, if the pipe exit is not throttled, then $k=1$.

The original solutions to the flow equations for $\gamma=1.4$ are presented in a graphical form (see Fig. 3.4). They are applicable to inflow and outflow in an unsteady gas flow regime where a pressure wave in a pipe is incident into a pressure filled space. For any particular

calculation, B and k are always known, so the amplitude ratio of the reflection pressure wave, X_r , can be determined from the graph.

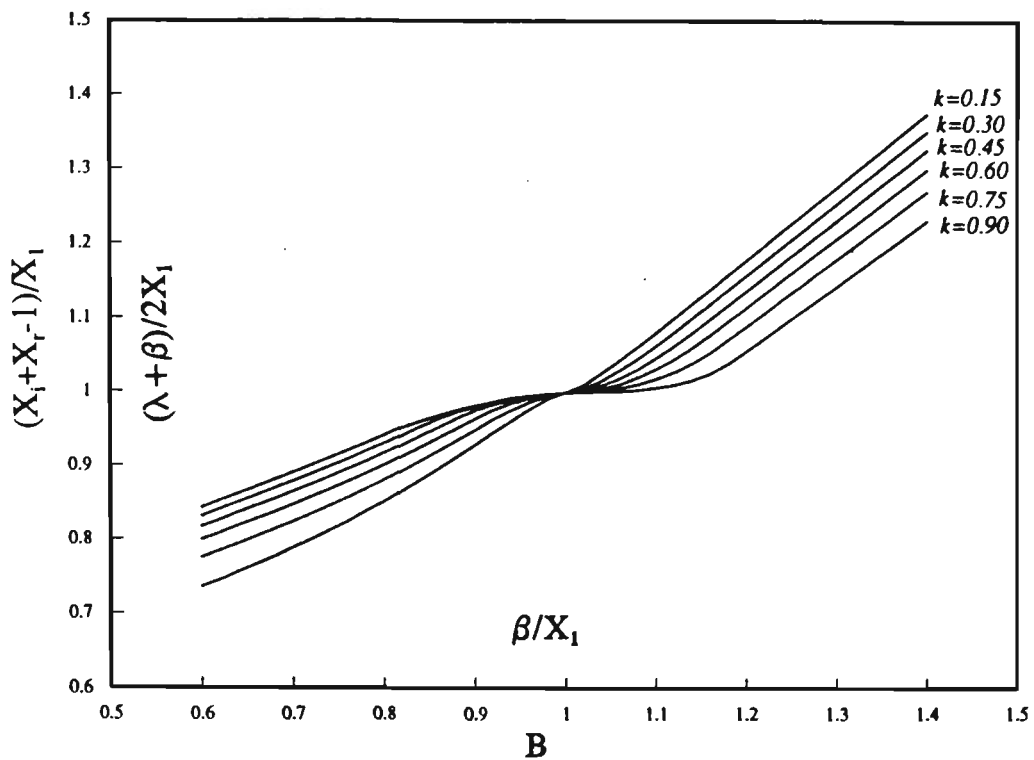


Fig. 3.4 Boundary condition chart for flow at port

3.3 The Method of Characteristics (MOC)

A characteristic curve, or characteristic for brevity, is a path of propagation of a physical disturbance. From a rigorous mathematical point of view, a characteristic is defined as a curve (known as the characteristic curve) along which the governing partial differential equations (PDE) reduce to ordinary differential equations (known as compatibility equations). The original partial differential equations may therefore be replaced by these ordinary differential equations written in co-ordinates which are the characteristics of the PDE. The solution of the partial differential equations is then achieved by simultaneously solving the ordinary differential equations which describe the paths of the characteristics, together with the ordinary differential equations which are the compatibility conditions written in terms of the characteristic co-ordinates. For quasi one dimensional flow in a

pipe, this may be carried out numerically. For example, consider a single first order partial differential equation.

$$A \frac{\partial f}{\partial t} + B \frac{\partial f}{\partial x} + D = 0 \quad (3.19)$$

The coefficients A, B and the non-homogeneous term D, may be functions of x, t and f.

If the dependent variable $f(x, t)$ is continuous everywhere within the calculation domain, then the total derivative of f with respect to x is:

$$\frac{df}{dx} = \frac{\partial f}{\partial x} + \frac{\partial f}{\partial t} \frac{dt}{dx} \quad (3.20)$$

The characteristic equation for the original partial differential equation (3.19) is defined as the curve in the x - t plane that has the slope given by:

$$\frac{dt}{dx} = \frac{A}{B} = C(x, y, f) \quad (\text{characteristic equation}) \quad (3.21)$$

at each point of its domain.

The original partial differential equation (3.19) then becomes:

$$B df + D dx = 0 \quad (\text{compatibility equation}) \quad (3.22)$$

since

$$B \left(\frac{\partial f}{\partial x} + \frac{A}{B} \frac{\partial f}{\partial t} \right) = B \frac{df}{dx}$$

along the curve

$$\frac{dt}{dx} = \frac{A}{B}$$

Equation (3.22) is an ordinary differential equation, valid only along the characteristic curve specified by equation (3.21). Equations (3.21) and (3.22) constitute an equivalent system of ordinary differential equations which may replace the original partial differential

equation, equation (3.19).

The system of quasi-linear non-homogeneous partial differential equations governing quasi one dimensional compressible flow in a pipe can be written as sets of equations like equations (3.21) and (3.22). This will be shown below.

3.4 Characteristic and Compatibility Equations for Quasi One Dimensional Flow in a Pipe

Gas flow in each two-stroke engine pipe may be regarded as unsteady quasi-one dimensional flow. Term quasi-one dimensional flow refers to a flow in a passage having a slowly varying cross-sectional area, so that flow in any non axial direction is negligible.

The conservation equations governing quasi-one dimensional unsteady isentropic (that is, neglecting the effect of friction and heat loss during the process) flow are,

Continuity equation:

$$\frac{\partial \rho}{\partial t} + u \frac{\partial \rho}{\partial x} + \rho \frac{\partial u}{\partial x} + \frac{d(\ln A)}{dx} \rho u = 0 \quad (3.23)$$

Momentum equation:

$$\rho \frac{\partial u}{\partial t} + \rho u \frac{\partial u}{\partial x} + \frac{\partial p}{\partial x} = 0 \quad (3.24)$$

Energy equation:

$$\frac{\partial p}{\partial t} + u \frac{\partial p}{\partial x} - a^2 \left(\frac{\partial \rho}{\partial t} + u \frac{\partial \rho}{\partial x} \right) = 0 \quad (3.25)$$

To develop the characteristic and compatibility equations corresponding to equation (3.23), (3.24) and (3.25) which is a system of quasi-linear non-homogeneous partial differential equations of the first order, we form a differential operator, which is a linear sum of the above three governing equations, using Zucrow's notion [51]:

$$L = \sigma_1 (\text{continuity equation}) + \sigma_2 (\text{momentum equation}) \\ + \sigma_3 (\text{energy equation}) = 0$$

that is,

$$(\rho \sigma_1 + \rho u \sigma_2) \left[\frac{\partial u}{\partial x} + \frac{\rho \sigma_2}{\rho \sigma_1 + \rho u \sigma_2} \cdot \frac{\partial u}{\partial t} \right] + (\sigma_2 + u \sigma_3) \left[\frac{\partial p}{\partial x} + \frac{\sigma_3}{\sigma_2 + u \sigma_3} \cdot \frac{\partial p}{\partial t} \right] \\ + (u \sigma_1 - a^2 u \sigma_3) \left[\frac{\partial \rho}{\partial x} + \frac{\sigma_1 - a^2 \sigma_3}{u \sigma_1 - a^2 u \sigma_3} \cdot \frac{\partial \rho}{\partial t} \right] + \sigma_1 \frac{\rho u dA}{A dx} = 0 \quad (3.26)$$

where the σ 's are arbitrary parameters.

The characteristics of the above equation (3.26) shall be of the form:

$$C = \frac{dt}{dx} \quad (3.21)$$

allowing quantities such as

$$\left[\frac{\partial u}{\partial x} + \frac{\rho \sigma_2}{\rho \sigma_1 + \rho u \sigma_2} \cdot \frac{\partial u}{\partial t} \right]$$

to take the form d/dx where

$$\frac{d}{dx} = \left[\frac{\partial}{\partial x} + \frac{\rho \sigma_2}{\rho \sigma_1 + \rho u \sigma_2} \cdot \frac{\partial}{\partial t} \right]$$

Thus

$$C = \frac{\sigma_2}{\sigma_1 + u \sigma_2} = \frac{\sigma_3}{\sigma_2 + u \sigma_3} = \frac{\sigma_1 - a^2 \sigma_3}{u \sigma_1 - a^2 u \sigma_3} \quad (3.27)$$

and equation (3.26) becomes

$$\rho(\sigma_1 + u\sigma_2)du + (\sigma_2 + u\sigma_3)dp + (u\sigma_1 - a^2u\sigma_3)d\rho + \sigma_1 \frac{\rho u}{A} dA = 0 \quad (3.28)$$

provided the dependent variables u , p and ρ are continuous within the whole calculation domain.

Equation (3.28) is the compatibility equation which is valid along the characteristic curve determined by equation (3.27). Equations (3.27) represent three linear simultaneous equations which can be solved for σ_1 , σ_2 and σ_3 . This is done by rearranging equation (3.27) and considering the σ 's as unknown variables. The following simultaneous linear equations then result:

$$\begin{cases} \sigma_1(C) + \sigma_2(uC-1) + \sigma_3(0) = 0 & (3.29) \\ \sigma_1(0) + \sigma_2(C) + \sigma_3(uC-1) = 0 & (3.30) \\ \sigma_1(uC-1) + \sigma_2(0) + \sigma_3 a^2(1-uC) = 0 & (3.31) \end{cases}$$

Since these equations are each homogeneous, the determinant of the coefficient matrix must be zero. Therefore

$$\begin{vmatrix} C & (uC-1) & 0 \\ 0 & C & (uC-1) \\ (uC-1) & 0 & -a^2(uC-1) \end{vmatrix} = 0$$

or:

$$(uC-1)^2 - a^2 C^2 (uC-1) = 0$$

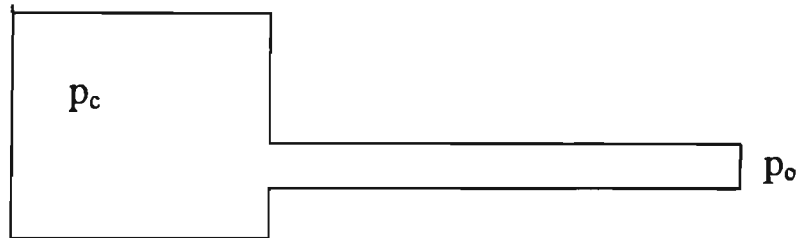
The roots of the above equation are :

$$C_0 = \left(\frac{dt}{dx} \right)_0 = \frac{1}{u} \quad (3.32)$$

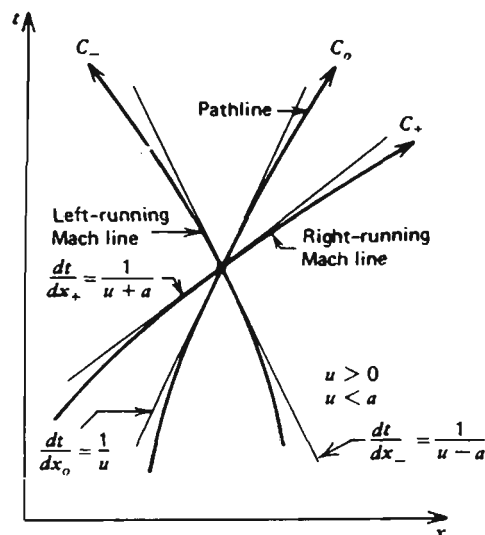
$$C_+ = \left(\frac{dt}{dx} \right)_+ = \frac{1}{u+a} \quad (3.33)$$

$$C_- = \left(\frac{dt}{dx} \right)_- = \frac{1}{u-a} \quad (3.34)$$

There are thus three families of characteristic curves in the t - x plane for quasi-one-dimensional pipe flow. C_0 , C_+ and C_- are termed path line, right-running Mach line and left-running Mach line, respectively. They are present in all flows, either subsonic or supersonic. For subsonic flow, C_+ and C_- are of opposite sign. However for supersonic flow, they have the same sign. Fig. 3.5 illustrates a subsonic flow from left to right in a pipe and its associated characteristics in the t - x plane.



a). An example of unsteady subsonic duct flow from left to right



(b). Characteristics for a wave point in flow in (a)

Fig. 3.5 Non-steady flow in a duct

The three compatibility equations corresponding to the three characteristic equations, equations (3.32)~(3.34), are obtained by solving for σ_1 , σ_2 and σ_3 and by substituting them into the general compatibility equation, equation (3.28).

For the path line characteristic, we already have

$$C_0 = \frac{1}{u} \quad (3.32)$$

Substituting equation (3.32) into the simultaneous linear equations (3.29)~(3.31) yields:

$$\sigma_1 = \sigma_2 = 0$$

The compatibility equation (3.28) becomes:

$${}_{(0)}\rho \frac{du}{dt} + \sigma_3 \frac{dp}{dt} + (0-a^2\sigma_3) \frac{d\rho}{dt} + {}_{(0)}\rho \frac{u}{A} \frac{dA}{dx} = 0$$

or

$$dp - a^2 d\rho = 0 \quad (3.35)$$

For the right-running Mach line characteristic:

$$C_+ = \frac{1}{u+a} \quad (3.33)$$

Substituting equation (3.33) into equations (3.29)~(3.31) yields:

$$\left\{ \begin{array}{l} \sigma_{1(c)} - \sigma_{2(ac)} = 0 \\ \sigma_{2(c)} - \sigma_{3(ac)} = 0 \\ \sigma_{1(ac)} - \sigma_{3(a^2c)} = 0 \end{array} \right.$$

thus

$$\sigma_1 = \sigma_3 a^2$$

and

$$\sigma_2 = \sigma_3 a$$

Now substituting σ_1 and σ_2 into the general compatibility equation, equation (3.28), and simplifying, we obtain:

$$dp + \rho a du = -a^2 \frac{\rho u}{A} \frac{dA}{dx} dt \quad (3.36)$$

Similarly, for the left running Mach line characteristic, the compatibility equation becomes

$$dp - \rho a du = -a^2 \frac{\rho u}{A} \frac{dA}{dx} dt \quad (3.37)$$

Summarising, the quasi-one dimensional unsteady isentropic pipe flow problem may be solved by the method of characteristics (MOC). There are three distinct characteristic curves: the path line C_0 and the two Mach lines C_+ and C_- . There is one compatibility equation valid for each of these three characteristic curves. These three sets of characteristic and compatibility equations may replace the original system of partial differential equations, equations (3.23), (3.24) and (3.25). The three sets of characteristic and compatibility equations are represented as follows

(1). For path line characteristic C_0 ,

$$\begin{cases} \frac{dt}{dx} = \frac{1}{u} \\ dp - a^2 d\rho = 0 \end{cases} \quad (3.38)$$

(2). For right-running Mach line characteristic C_+ ,

$$\begin{cases} \frac{dt}{dx} = \frac{1}{u+a} \\ dp + \rho a du = -a^2 \frac{\rho u}{A} \frac{dA}{dx} \cdot dt \end{cases} \quad (3.39)$$

(3). For left-running Mach line characteristic C_+ ,

$$\begin{cases} \frac{dt}{dx} = \frac{1}{u-a} \\ dp - \rho a du = -a^2 \frac{\rho u}{A} \frac{dA}{dx} \cdot dt \end{cases} \quad (3.40)$$

3.5 Solution of Equations with the Riemann Variable Technique

Along the characteristic C_+ , the compatibility equation is:

$$dp + \rho a du = -a^2 \frac{\rho u}{A} \frac{dA}{dx} \cdot dt \quad (3.39)$$

Equation (3.39) may be expressed in terms of gas particle velocity u and velocity of sound a . For an isentropic process, the velocity of sound is given by,

$$a^2 = \frac{dp}{d\rho} \quad (3.41)$$

For a perfect gas flow,

$$a^2 = \left. \frac{dp}{d\rho} \right|_s = \frac{\gamma p}{\rho}$$

$$\text{or } p = \frac{1}{\gamma} \rho a^2 \quad (3.42)$$

Differentiating both sides of equation (3.42) with respect to time t ,

$$\frac{dp}{dt} = \frac{1}{\gamma} \left(a^2 \frac{d\rho}{dt} + 2a\rho \frac{da}{dt} \right) \quad (3.43)$$

For isentropic flow:

$$\frac{p}{\rho^\gamma} = \text{const} \quad (3.44)$$

$$\text{or } \ln p - \gamma \ln \rho = \text{const} \quad (3.45)$$

Substituting (3.42) into (3.45) gives,

$$\ln \frac{\rho a^2}{\gamma} - \gamma \ln \rho = \text{const}$$

For a constant γ ,

$$(1-\gamma) \ln \rho + 2 \ln a = \text{const}'$$

Differentiating both sides:

$$(1-\gamma) \frac{d\rho}{\rho} + 2 \frac{da}{a} = 0$$

$$\text{thus, } d\rho = -\frac{2\rho}{a(1-\gamma)}da \quad (3.46)$$

Substituting (3.46) into (3.43) yields:

$$\begin{aligned} \frac{d\rho}{dt} &= \frac{1}{\gamma} \left\{ a^2 \left[-\frac{2\rho}{a(1-\gamma)} \right] \frac{da}{dt} + 2a\rho \frac{da}{dt} \right\} \\ &= -\frac{2a\rho}{1-\gamma} \frac{da}{dt} \end{aligned} \quad (3.47)$$

and substituting equation (3.47) into the compatibility equation (3.39) yields:

$$\left[\left(-\frac{2a\rho}{1-\gamma} \right) \frac{da}{dt} \right] + \rho a \frac{du}{dt} = -\frac{\rho u a^2}{A} \frac{dA}{dx}$$

Simplifying and re-arranging:

$$\frac{d\left(a + \frac{\gamma-1}{2}u \right)}{dt} = -\frac{\gamma-1}{2}u a \left(\frac{1}{A} \frac{dA}{dx} \right) \quad (3.48)$$

Let a_0 be the speed of sound corresponding to isentropic expansion or compression from the local pressure to a reference pressure, usually atmospheric pressure. Equation (3.48) may be non-dimensionalised by using the following non-dimensional parameters:

$$a^* = \frac{a}{a_0}, \quad U = \frac{u}{a_0}, \quad Z = \frac{a_0 \cdot t}{x_{ref}}, \quad X = \frac{x}{x_{ref}}$$

In an isentropic process, a_0 is constant with respect to space and time. Using x_{ref} as a reference length, equation (3.48) becomes,

$$\frac{d\left(a^* + \frac{\gamma-1}{2}U\right)}{dZ} = -\frac{\gamma-1}{2}U a^* \cdot \left(\frac{1}{A} \frac{dA}{dX}\right) \quad (3.49)$$

Defining,

$$\lambda = a^* + \frac{\gamma-1}{2}U \quad (3.50)$$

Equation (3.49) may be written

$$\frac{d\lambda}{dZ} = -\frac{\gamma-1}{2}U a^* \left(\frac{1}{A} \frac{dA}{dX}\right) \quad (3.51)$$

for the right-running Mach line characteristic.

Applying the same logic to the C_+ characteristic curve, the compatibility equation in equation (3.40) valid along this curve becomes,

$$\frac{d\left(a^* - \frac{\gamma-1}{2}U\right)}{dZ} = -\frac{\gamma-1}{2}U a^* \cdot \left(\frac{1}{A} \frac{dA}{dX}\right) \quad (3.52)$$

Defining

$$\beta = a^* - \frac{\gamma-1}{2}U \quad (3.53)$$

Substituting β into equation (3.52) gives,

$$\frac{d\beta}{dZ} = -\frac{\gamma-1}{2}U a^* \left(\frac{1}{A} \frac{dA}{dX}\right) \quad (3.54)$$

For the path line characteristic, it is apparent that the compatibility equation is identical to the definition of an isentropic process. Since the flow has been assumed isentropic in the preceding derivations, this equation is redundant.

λ and β are called Riemann Variables. They may alternatively represent any point on characteristic curve C_+ (or C_-) which satisfies the compatibility equation. The relation between Riemann variables and flow variables u , ρ , and p is sought in the next section.

3.6 Evaluation of Flow Variables in Terms of Riemann Variables

Consider again the theory of superposition of pressure waves presented in 3.2.2 and Fig. 3.2. Suppose at $t=t_0$, the wave point R on the right running wave RW and wave point L on the left running wave LW are about to meet, see Fig. 3.6. Characteristic curves C_+ and C_- emanating from point R and L respectively are to intersect at a later moment at S while point R and L coincide.

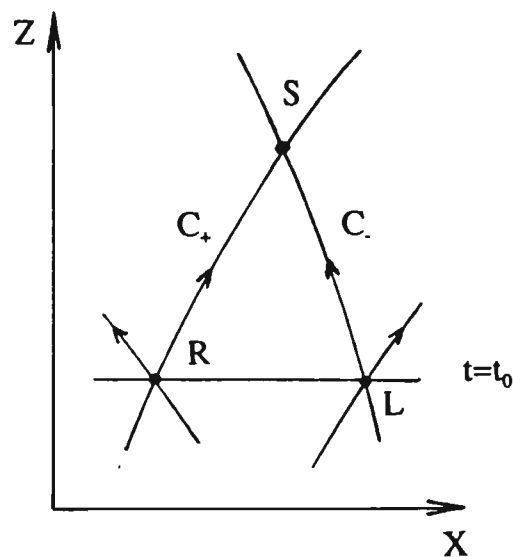


Fig. 3.6 Determination of flow variables

From equations (3.50) and (3.53), at point S, we have:

$$U = \frac{2}{\gamma - 1} (\lambda - a^*)$$

$$U = \frac{2}{\gamma - 1} (a^* - \beta)$$

Solving simultaneously for U and a^* gives,

$$U = \frac{\lambda - \beta}{\gamma - 1} \quad (3.55)$$

$$a^* = \frac{\lambda + \beta}{2} \quad (3.56)$$

As explained in section 3.2.2, equation (3.15), the superposition pressure amplitude ratio X at the location where two wave points from wave RW and wave LW coincide, is:

$$X_s = X_R + X_L - 1$$

Also, by definition:

$$\begin{aligned} X_s &= \left(\frac{p_s}{p_0} \right)^{\frac{\gamma-1}{2\gamma}} \\ &= \sqrt{\frac{T_s}{T_0}} = a^* \end{aligned} \quad (3.57)$$

where T_0 is the reference temperature corresponding to the reference pressure p_0 .

The dimensionless superposition particle velocity U may be written

$$\begin{aligned} U &= \frac{u}{a_0} \\ &= \frac{2}{\gamma - 1} (X_R - X_L) \end{aligned} \quad (3.58)$$

Substituting equations (3.15), (3.57) into (3.56) and (3.58) into (3.55), respectively, we obtain the right-ward running pulse pressure amplitude ratio:

$$X_R = \frac{\lambda + 1}{2} \quad (3.59)$$

The left-ward running pulse pressure amplitude ratio is

$$X_L = \frac{\beta+1}{2} \quad (3.60)$$

Superposition pressure amplitude ratio:

$$\begin{aligned} X_s &= X_R + X_L - 1 \\ &= \frac{\lambda + \beta}{2} \end{aligned} \quad (3.61)$$

Superposition particle velocity:

$$\begin{aligned} u &= a_0 U \\ &= \frac{a_0}{\gamma - 1} (\lambda - \beta) \end{aligned} \quad (3.62)$$

Superposition density:

$$\begin{aligned} \rho &= \rho_0 X_s^{\frac{2}{\gamma-1}} \\ &= \rho_0 \left(\frac{\lambda + \beta}{2} \right)^{\frac{2}{\gamma-1}} \end{aligned} \quad (3.63)$$

Superposition temperature:

$$\begin{aligned} T &= T_0 X_s^2 \\ &= T_0 \left(\frac{\lambda + \beta}{2} \right)^2 \end{aligned} \quad (3.64)$$

Resultant mass flow rate:

$$\begin{aligned} \dot{m} &= \rho u A \\ &= \frac{\lambda - \beta}{\gamma - 1} \cdot \left(\frac{\lambda + \beta}{2} \right)^{\frac{2}{\gamma-1}} \cdot (A \rho_0 a_0) \end{aligned} \quad (3.65)$$

3.7 Computation of Riemann Variables

In the foregoing paragraphs, the governing partial differential equations for unsteady quasi-one dimensional pipe flow have been presented in equations (3.23)-(3.25). The

corresponding characteristic and compatibility equations were presented in equations (3.38)-(3.40). The compatibility equations have been expressed in terms of dimensionless local sound speed A and dimensionless gas particle velocity U only. The Riemann variables were introduced during this mathematical manipulation. As all the relevant flow properties were shown as functions of the Riemann variables λ and β , the unsteady flow field may be obtained if λ and β over all space and time are solved.

The numerical solution for λ and β is performed in the dimensionless time-distance plane (Z - X plane). The Z - X plane is discretized into a rectangular grid system. The grid pattern is fixed in the X -direction (the pipe is equally divided into a number of meshes) but the Z -direction subdivisions are adjusted according to the Courant-Friedrichs-Lewy stability criterion discussed below. Each mesh point can then be indexed by two numbers, a number vertically and a number horizontally, as depicted in Fig. 3.7.

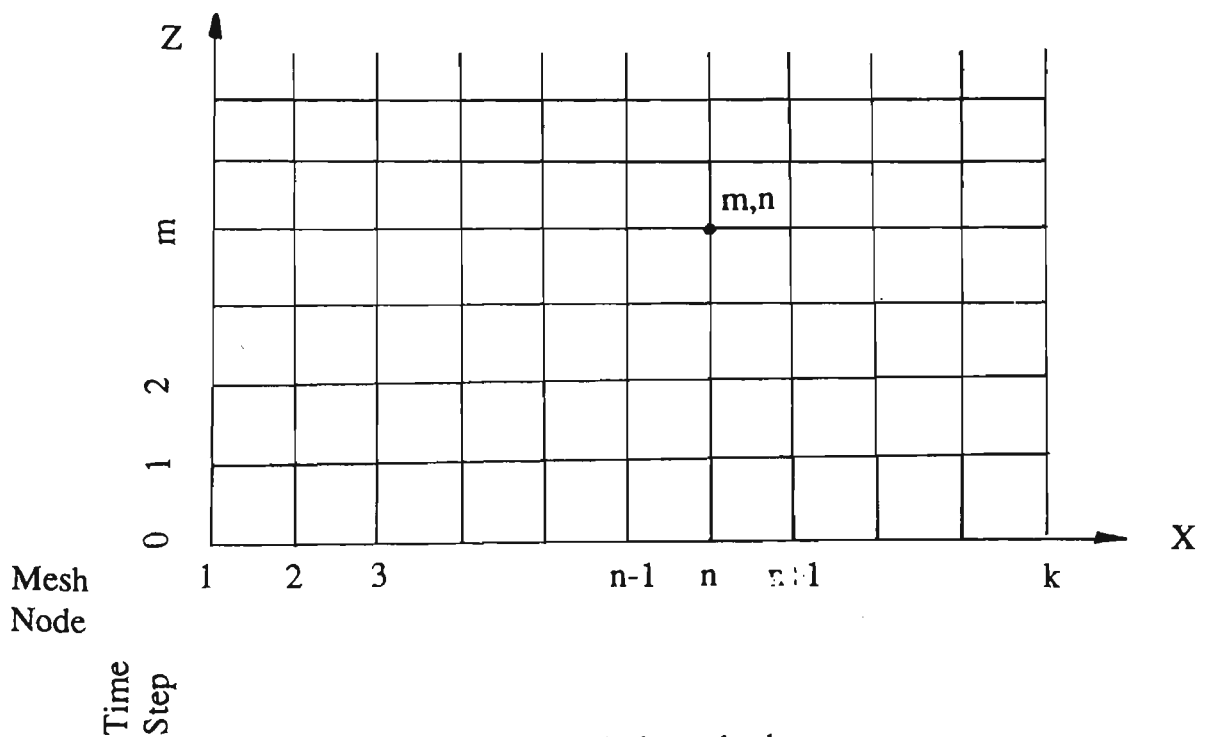


Fig. 3.7 Mesh method

At a given time $Z = Z_m$, the Riemann variables λ and β at each grid point along the pipe, such as $\lambda_{(m,1)}$, $\beta_{(m,1)}$, ..., $\lambda_{(m,n)}$ and $\beta_{(m,n)}$, etc, are known from the previous calculations. These values of λ and β are similar to the initial values at the grid points on an initial value curve $\Gamma(0,X)$ in an analytical solution to the PDE's and are used as initial values to determine all λ 's and β 's at the new time. To achieve this, two characteristic curves C_+ and

C. emanating from each grid point on row m are moving upwards in the Z - X plane by one row onto row $(m+1)$. However these characteristics do not in general pass through any of the mesh points on that row, as shown in Fig. 3.8, and it is the values on the grid points at $Z_{(m+1)} = Z_m + \Delta Z$ which are needed to continue the calculation.

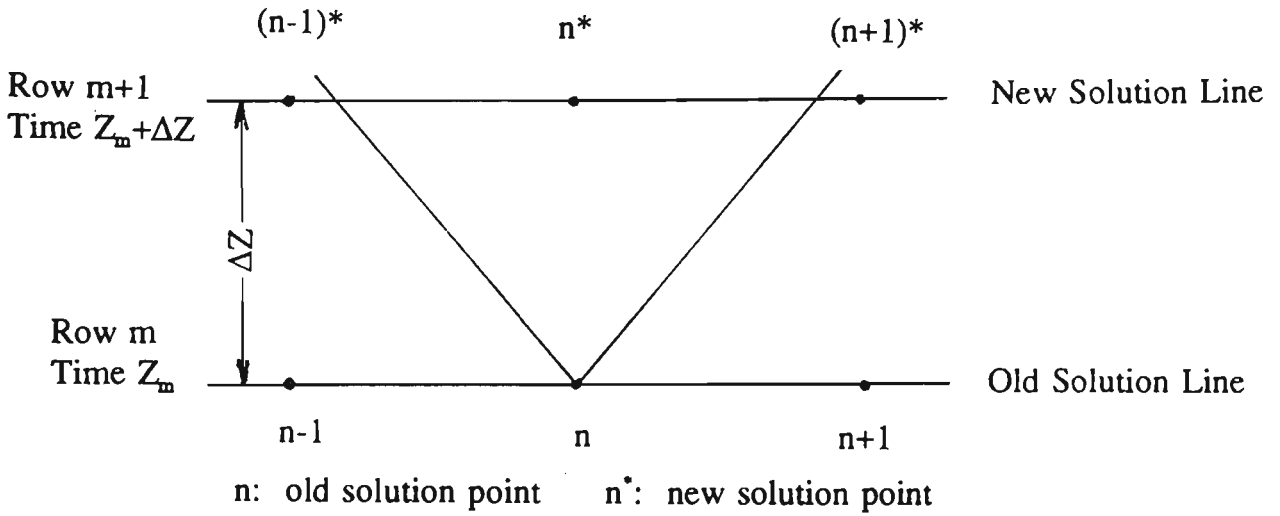


Fig. 3.8 Development of characteristics on discrete Z - X plane

The system used is therefore revised to choose characteristics from row m which just pass through the mesh points on row $(m+1)$. This is known as the inverse marching method. Linear interpolation is used to calculate approximately the values of λ and β between the mesh points at time $Z = Z_m$. Fig. 3.9 illustrates the grid allocation.

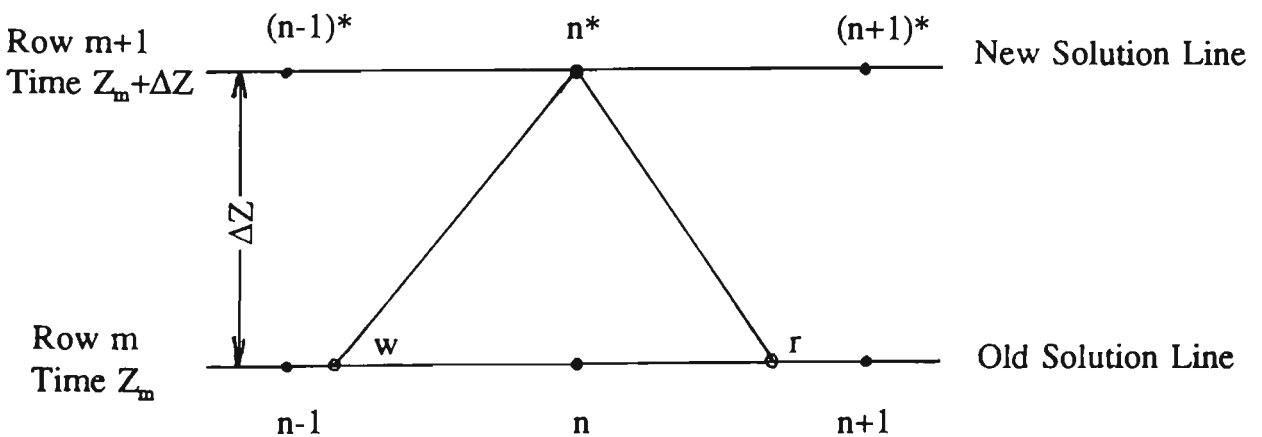


Fig. 3.9 Inverse marching method

To ensure that the solution is stable, the Courant-Friedrichs-Lewy (CFL) stability criterion [52] must be satisfied. The criterion requires that the initial data points (such as points w and r on Fig. 3.9) fall between the previous solution points $((n-1), (n+1))$ at $Z = Z_m$ that are employed in the interpolation for determining the Riemann variables at points w and r . Points such as $(n-1)^*$, n^* , $(n+1)^*$ and so on in that figure are equivalent to points $(n-1)$, n and $(n+1)$ at the new time step. The criterion is only satisfied by choosing the time step size ΔZ after the spatial mesh size is decided. The choice of ΔZ is made by the following procedure (refer Fig. 3.10):

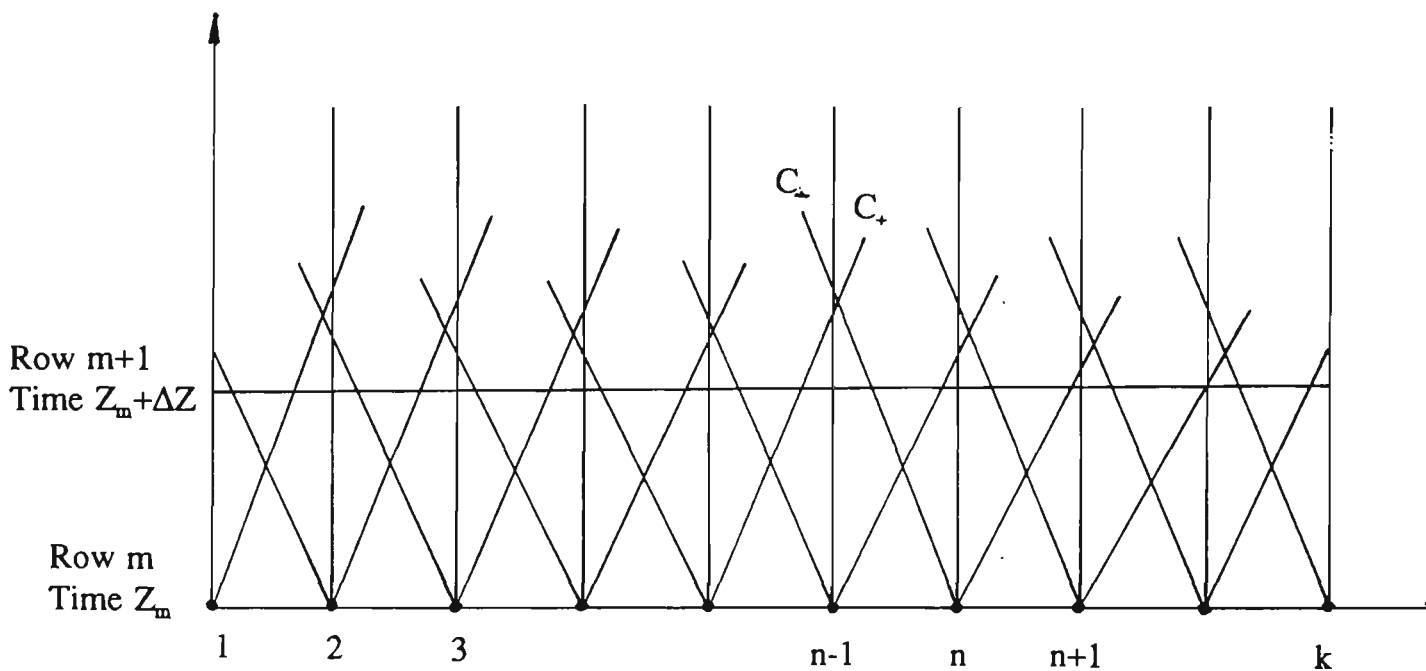


Fig. 3.10 Determination of the size of time step

1. For each mesh point on row m , calculate the slope of all characteristic curves. As the length of meshes is small, it is assumed here that the C_+ and C_- characteristics which emanate from grid points on row m and move toward row $(m+1)$ are straight lines with their slopes dependent on λ_n and β_n only. For C_+ characteristics, the slope at grid node n is:

$$\frac{dZ}{dX} = \frac{1}{U_n + a_n^*}$$

$$= \frac{2(\gamma-1)}{(1+\gamma)\lambda_n - (3-\gamma)\beta_n} \quad (3.66)$$

and for C_- characteristics:

$$\begin{aligned} \frac{dZ}{dX} &= \frac{1}{U_n - a_n^*} \\ &= \frac{2(\gamma-1)}{(3-\gamma)\lambda_n - (1+\gamma)\beta_n} \end{aligned} \quad (3.67)$$

$$(n=1,2,3,\dots)$$

2. Choose the absolute minimum slope $(dZ/dX)_{\min}$ among all slopes in the C_+ and C_- families determined in step (i).
3. The time step size ΔZ is then determined

$$\Delta Z \leq \left(\frac{dZ}{dX} \right) \cdot \Delta X \quad (3.68)$$

where ΔX is the dimensionless mesh length.

This calculation must be performed for all pipes in an engine as it is the "largest" allowable time step which must be chosen. It ensures that all the new solution points for points 2, 3 and so on in Fig. 3.10 are within their corresponding zone of influence determined by the previous solution points.

Finally, the solution of Riemann variables at a non-mesh-node is described. When the mesh size is chosen small, we may assume that the values of λ and β vary linearly between two neighbourhood mesh nodes. With reference to Fig. 3.11, the following simultaneous equations are established:

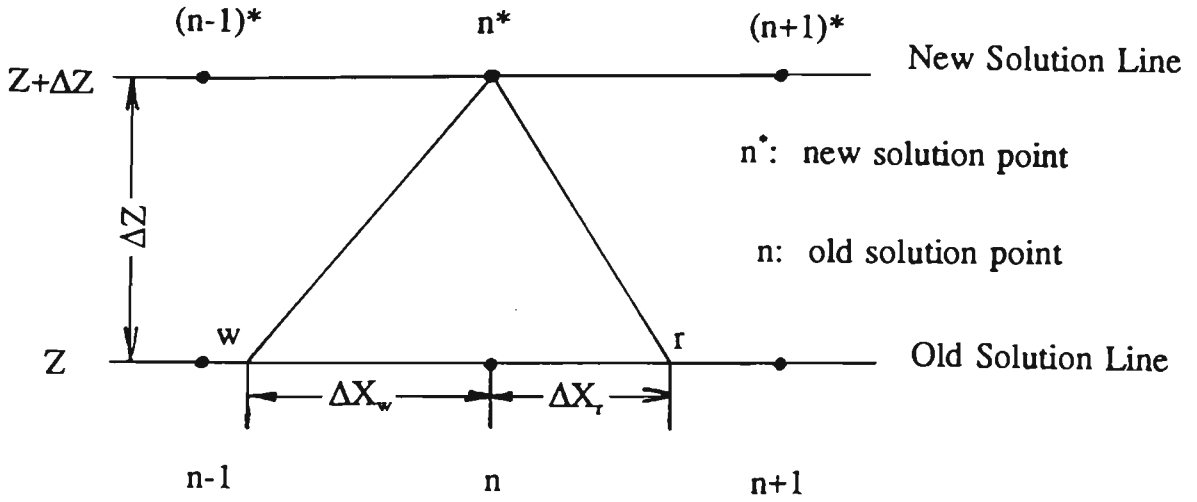


Fig. 3.11 Linear interpolation for non-mesh node values

For point w , with the assumption that the characteristic curve is a segment of a straight line and its slope evaluated at the old time step,

$$\lambda_w = \lambda_n - \frac{\Delta X_w (\lambda_n - \lambda_{n-1})}{\Delta X} \quad (3.69)$$

$$\beta_w = \beta_n - \frac{\Delta X_w (\beta_n - \beta_{n-1})}{\Delta X} \quad (3.70)$$

$$\frac{\Delta Z}{\Delta X_w} = \frac{1}{U_w + a_w^*} = \frac{2(\gamma - 1)}{(1 + \gamma)\lambda_w - (3 - \gamma)\beta_w} \quad (3.71)$$

Similarly, for point r ,

$$\lambda_r = \lambda_n + \frac{\Delta X_r (\lambda_{n+1} - \lambda_n)}{\Delta X} \quad (3.72)$$

$$\beta_r = \beta_n + \frac{\Delta X_r (\beta_{n+1} - \beta_n)}{\Delta X} \quad (3.73)$$

$$\frac{\Delta Z}{\Delta X_r} = \frac{1}{U_r - a_r^*} = \frac{2(\gamma-1)}{(1+\gamma)\beta_r - (3-\gamma)\lambda_r} \quad (3.74)$$

The solutions for equations (3.69)-(3.74) are as follows,

$$\lambda_w = \frac{2(\gamma-1)\lambda_n + (3-\gamma)(\lambda_n\beta_{n-1} - \lambda_{n-1}\beta_n) \cdot \Delta Z}{2(\gamma-1) + \Delta Z \cdot [(1+\gamma)(\lambda_n - \lambda_{n-1}) - (3-\gamma)(\beta_n - \beta_{n-1})]} \quad (3.75)$$

$$\beta_w = \frac{2(\gamma-1)\beta_n + (1+\gamma)(\lambda_n\beta_{n-1} - \lambda_{n-1}\beta_n) \cdot \Delta Z}{2(\gamma-1) + \Delta Z \cdot [(1+\gamma)(\lambda_n - \lambda_{n-1}) - (3-\gamma)(\beta_n - \beta_{n-1})]} \quad (3.76)$$

$$(n=2,3,\dots,k)$$

and

$$\lambda_r = \frac{2(\gamma-1)\lambda_n + (1+\gamma)(\lambda_{n+1}\beta_n - \lambda_n\beta_{n+1}) \cdot \Delta Z}{2(\gamma-1) + \Delta Z \cdot [(1+\gamma)(\beta_n - \beta_{n+1}) - (3-\gamma)(\lambda_n - \lambda_{n+1})]} \quad (3.77)$$

$$\beta_r = \frac{2(\gamma-1)\beta_n + (3-\gamma)(\lambda_{n+1}\beta_n - \lambda_n\beta_{n+1}) \cdot \Delta Z}{2(\gamma-1) + \Delta Z \cdot [(1+\gamma)(\beta_n - \beta_{n+1}) - (3-\gamma)(\lambda_n - \lambda_{n+1})]} \quad (3.78)$$

$$(n=1,2,\dots,k-1)$$

and

$$\Delta X_w = \Delta Z \left[\frac{(1+\gamma)\lambda_w - (3-\gamma)\beta_w}{2(\gamma-1)} \right] \quad (3.79)$$

$$\Delta X_r = \Delta Z \left[\frac{(1+\gamma)\beta_r - (3-\gamma)\lambda_r}{2(\gamma-1)} \right] \quad (3.80)$$

3.8 Integration of Riemann Variables Along the Direction of Characteristics

To evaluate the Riemann variables λ and β at the new solution points, the compatibility equations, equations (3.51) and (3.54) should be integrated along their characteristic curves. The integration of the compatibility equation (3.51) along a C_+ characteristic curve from w to n^* in Fig. 3.11 leads to:

$$\int_w^{n^*} d\lambda = \int_w^{n^*} \left(-\frac{\gamma-1}{2} \right) U a^* \left(\frac{1}{A} \frac{dA}{dX} \right) dZ$$

that is,

$$\begin{aligned} \lambda_{n^*} &= \lambda_w + \int_w^{n^*} \left(-\frac{\gamma-1}{2} \right) U a^* \left(\frac{1}{A} \frac{dA}{dX} \right) dZ \\ &= \lambda_w + \int_w^{n^*} \left(-\frac{\gamma-1}{2} \right) \left(\frac{\lambda-\beta}{\gamma-1} \right) \left(\frac{\lambda+\beta}{2} \right) \left(\frac{1}{A} \frac{dA}{dX} \right) dZ \\ &= \lambda_w - \frac{1}{4} \int_w^{n^*} (\lambda^2 - \beta^2) \left(\frac{1}{A} \frac{dA}{dX} \right) dZ \end{aligned} \quad (3.81)$$

Also, from integrating equation (3.54) along its C_- characteristics r - n^* in Fig. 3.11,

$$\beta_{n^*} = \beta_r - \frac{1}{4} \int_r^{n^*} (\lambda^2 - \beta^2) \left(\frac{1}{A} \frac{dA}{dX} \right) dZ \quad (3.82)$$

The integrals in equations (3.81) and (3.82) involve values of λ , β , A and $\frac{1}{A} \frac{dA}{dX}$ evaluated at the points w , r and n^* . Unfortunately, λ and β at n^* are the

unknowns, so a correct numerical evaluation would involve an iterative solution. Applying the trapezoidal rule of integration to equations (3.81) and (3.82) leads to equations (3.83) and (3.84):

$$\lambda_{n^*} - \lambda_w = -\frac{\Delta Z}{8} \left[(\lambda_w^2 - \beta_w^2) \left(\frac{1}{A} \frac{dA}{dX} \right)_w + (\lambda_{n^*}^2 - \beta_{n^*}^2) \left(\frac{1}{A} \frac{dA}{dX} \right)_{n^*} \right] \quad (3.83)$$

$$\beta_{n^*} - \beta_r = -\frac{\Delta Z}{8} \left[(\lambda_r^2 - \beta_r^2) \left(\frac{1}{A} \frac{dA}{dX} \right)_r + (\lambda_{n^*}^2 - \beta_{n^*}^2) \left(\frac{1}{A} \frac{dA}{dX} \right)_{n^*} \right] \quad (3.84)$$

λ_w , β , λ and β are obtained from equations (3.75) - (3.78). The size of the time increment ΔZ is determined by the Courant-Friedrichs-Lewy (CFL) stability criterion. Equations (3.83) and (3.84) can be solved for λ_{n^*} and β_{n^*} using the Euler predictor-corrector algorithm. However such a procedure can be quite complicated and involves heavy computation. An approximation was made to evaluate all functions involving λ and β inside the integrals in equations (3.81) and (3.82) at the known points such as w and r , but to treat the more crucial area change term $\left(\frac{1}{A} \frac{dA}{dX} \right)$ correctly. Equation (3.81) thus

becomes

$$\begin{aligned} \lambda_{n^*} &= \lambda_w - \frac{1}{4} \int_w^{n^*} (\lambda^2 - \beta^2) \left(\frac{1}{A} \frac{dA}{dX} \right) dZ \\ &\approx \lambda_w - \frac{1}{4} (\lambda_w^2 - \beta_w^2) \int_w^{n^*} \left(\frac{1}{A} \frac{dA}{dX} \right) dZ \end{aligned} \quad (3.85)$$

where λ and β have been approximated at point w .

Applying the trapezoidal rule of integration, the integral in equation (3.85) can be approximated as:

$$\int_w^{n^*} \left(\frac{1}{A} \frac{dA}{dX} \right) dZ \approx \frac{\Delta Z}{2} \left[\left(\frac{1}{A} \frac{dA}{dX} \right)_w + \left(\frac{1}{A} \frac{dA}{dX} \right)_{n^*} \right] \quad (3.86)$$

when the time step ΔZ is small.

The term in the square brackets in equation (3.86) may be further approximated by $\left(\frac{1}{A} \frac{dA}{dX} \right)_M$, where M is the mid-point between w and n^* , as depicted in Fig. 3.12. Thus,

$$\lambda_{n^*} \approx \lambda_w - \frac{\Delta Z}{4} (\lambda_w^2 - \beta_w^2) \cdot \left(\frac{1}{A} \frac{dA}{dX} \right)_M \quad (3.87)$$

Similarly, from equation (3.82), we obtain:

$$\beta_{n^*} \approx \beta_r - \frac{\Delta Z}{4} (\lambda_r^2 - \beta_r^2) \cdot \left(\frac{1}{A} \frac{dA}{dX} \right)_N \quad (3.88)$$

where N is the mid-point between n^* and r.

The evaluation of the crucial area change term, $\frac{1}{A} \frac{dA}{dX}$, is carried out by one of

following two methods (refer to Fig. 3.12):

1. Mean value evaluation

(a). Evaluate pipe area at each mesh node.

(b). Use the linear interpolation method to find out A_M and A_N .

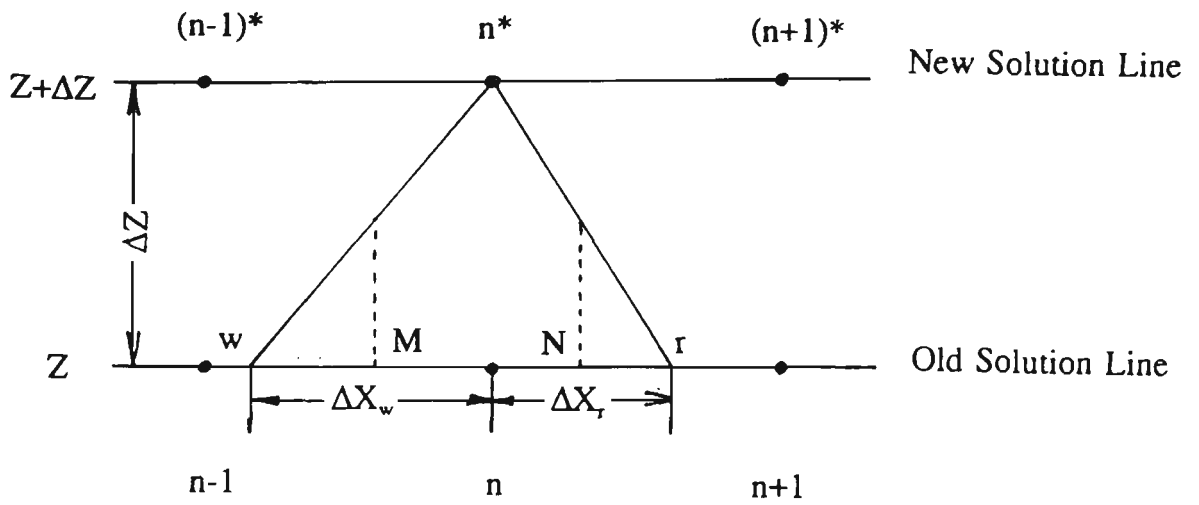


Fig. 3.12 Evaluation of $\frac{1}{A} \frac{dA}{dX}$ at points M and N

(c). Area change terms are found as follows,

$$\left(\frac{1}{A} \frac{dA}{dX} \right)_M = \frac{1}{A_M} \frac{A_n - A_w}{\Delta X_w}$$

and

$$\left(\frac{1}{A} \frac{dA}{dX} \right)_N = \frac{1}{A_N} \frac{A_r - A_n}{\Delta X_r} \quad (3.89)$$

where

$$A_M = \frac{A_w + A_n}{2};$$

$$A_N = \frac{A_r + A_n}{2};$$

2. Analytical evaluation

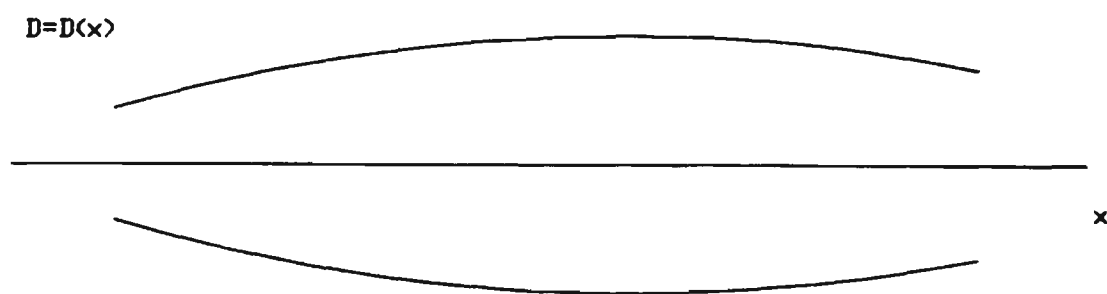
- (a). Assume pipe diameter D is a function of pipe length x , as shown in Fig. 3.13(a), then

$$D = D(x)$$

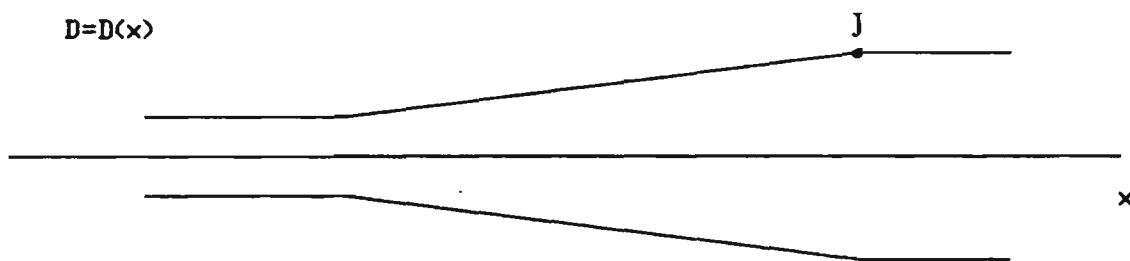
$$A = \frac{\pi D^2}{4}$$

therefore

$$\frac{1}{A} \frac{dA}{dx} = \frac{2}{D} \frac{dD}{dx} \quad (3.90)$$



(a) One-dimensional pipe



(b) A tapered pipe

Fig. 3.13 Geometric consideration for quasi-one dimensional flow model

If D is a linear function of x , Fig. 3.13(b), that is, a tapered pipe, as is commonly found in engine pipe sections, then

$$D = ax + b \quad (3.91)$$

and

$$\frac{1}{A} \frac{dA}{dx} = \frac{2a}{ax + b} \quad (3.92)$$

a and b are determined from the pipe geometry. It will be assumed that all pipes are composed of linearly tapered sub-sections for which the appropriate values of a and b can be obtained for use in equation (3.92).

(b). At points like J in Fig. 13(b), $\frac{1}{A} \frac{dA}{dX}$ has two values - a positive value to the left

and a zero value to the right. Area change is discontinuous. In a numerical solution, it is best to take an average of the two values at point J to smear the geometrical

discontinuity. If $\frac{1}{A} \frac{dA}{dX} \Big|_{J^-} = t_1$ and $\frac{1}{A} \frac{dA}{dX} \Big|_{J^+} = 0$, then

$$\frac{1}{A} \frac{dA}{dx} \Big|_J = \frac{t_1 + 0}{2} \quad (3.93)$$

(c). Compute the area change term $\frac{1}{A} \frac{dA}{dX}$ at each mesh node.

(d). Using linear interpolation, find $\frac{1}{A} \frac{dA}{dX} \Big|_M$ and $\frac{1}{A} \frac{dA}{dX} \Big|_N$ and substitute them into

equations (3.87) and (3.88). The Riemann variables λ and β at the new time step,

λ^* and β^* , are therefore determined.

The approximation outlined gave satisfactory results so the iterative solution was not pursued.

In Blair's [24] two-stroke engine simulation model (PROG5.2), the pipe flow model is contained in sub-program PIPE. It has been found, however, in Blair's work (refer to Fig.

3.12) that the area change term $\frac{1}{A} \frac{dA}{dX}$ was treated by taking the area term A from the

pipe area at grid node n, and the area derivative dA/dX was evaluated at the mid-point of two neighbouring mesh nodes, say node (n-1) and node n. Thus:

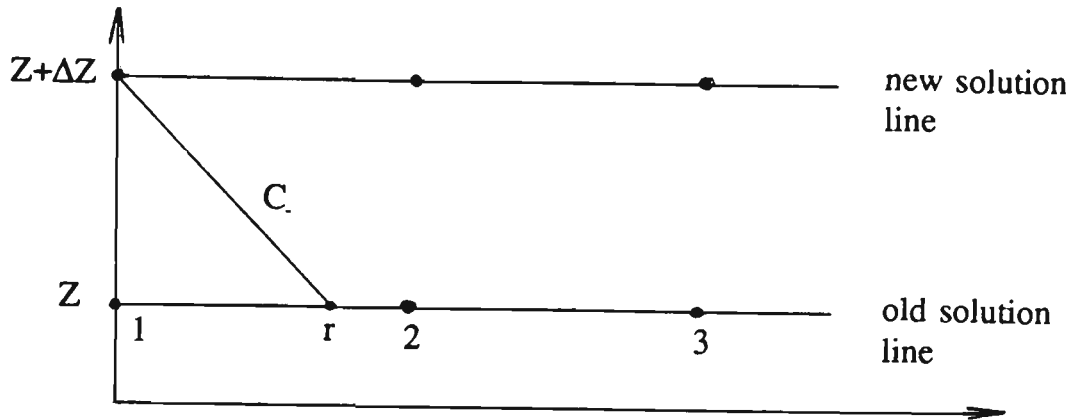
$$\frac{1}{A} \frac{dA}{dX} \approx \left(\frac{A_n - A_{n-1}}{\Delta X} \right) \frac{1}{A_n}$$

As this evaluation of the area change term uses a value which is out of the domain of dependence of grid node n*, and thus not in keeping with the correct numerical integration of equation (3.87), this may cause numerical instability, even though the choice of the time step ΔZ did satisfy the CFL stability criterion. Blair's program has therefore been modified according to the aforementioned derivations. A copy of the modified code may be found in Appendix B.

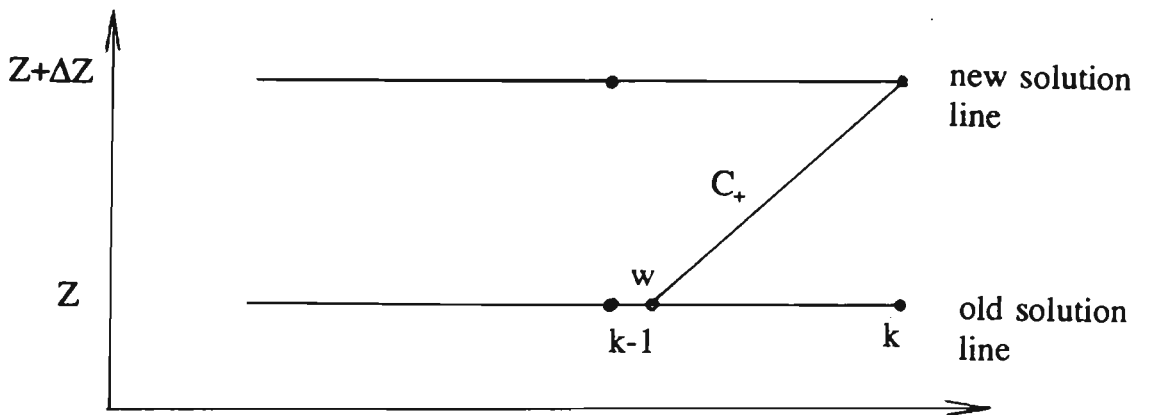
3.9 Calculation of Riemann Variables At Pipe Ends

The value of λ or β at the extreme ends of the pipe, either at the port/pipe interface boundary or at the pipe exit boundary, cannot be determined by using the method of characteristics described in the previous sections. This is because, depending on the flow Mach number, two, one or no characteristic curves may intersect the first mesh node at such boundaries and except for the first case, additional conditions must be supplied. Fig.

3.14 illustrates the case for a subsonic flow where only one characteristic is available from the previous calculation as presented in section 3.7.



(a) Incident characteristics (C_-) at LHS pipe end



(b) Incident characteristics (C_+) at RHS pipe end

Fig. 3.14 Incident characteristics at pipe ends for a subsonic flow from left to right

To calculate the wave reflections, the boundary conditions (the four sets of governing equations for subsonic outflow, subsonic inflow, sonic outflow and sonic inflow, whichever is appropriate, as described in 3.2.3) must be computed. The solution of the equations presented in Fig. 3.4 has shown that the reflection of pressure wave at the pipe

ends is dependent on the instantaneous cylinder pressure, incident wave pressure and the port/pipe area ratio. When the Riemann variable technique is used, the pressure in the pipes is not directly solved and Fig. 3.4 cannot be employed directly. Nevertheless, a simple transform of coordinates makes Fig. 3.4 applicable for the Riemann variable technique. Assuming the incident wave is left-running and the reflected wave is right-running, then from the derivations in section 3.6, we have,

For the vertical axis in Fig. 3.4:

$$\begin{aligned} \frac{X_i + X_r - 1}{X_1} &= \frac{X_L + X_R - 1}{X_1} \\ &= \frac{\lambda + \beta}{2X_1} \end{aligned} \quad (3.94)$$

And for the horizontal axis in Fig. 3.4,

$$\begin{aligned} B &= \frac{2X_i - 1}{X_1} = \frac{2X_L - 1}{X_1} \\ &= \frac{\beta}{X_1} \end{aligned} \quad (3.95)$$

Thus for particular values of B and k , Fig. 3.4 can be used to find $(\lambda + \beta)/2X_1$, from which the appropriate values of λ can be recovered.

Blair [47] solved four sets of governing equations for small increments of k and B using the Newton-Raphson method. The outputs are basically digitisations of Wallace's graphs [45] and are stored in a two-dimensional array. In this array, B ranges from 0.6 to 1.4 in steps of 0.02 whilst k ranges from zero to 1.0 in steps of 0.05. Two dimensional linear interpolation is used in the engine computer model, Blair [24], to find values of reflected wave pressure X_r for given values of k and B .

The problem associated with the solutions of boundary condition is that the values are valid only for $\gamma = 1.4$. γ may vary between the exhaust port and the inlet port so it really needs to be a parameter in the solution. Such computations would have required considerable further effort and as satisfactory agreement between the predicted engine performance and experiments were eventually obtained, the boundary conditions pertaining to a constant value of γ were retained.

3.10 Determination of In-Cylinder Thermodynamic State During the Scavenging Process: Open Cycle Analysis

3.10.1 Energy Equation for Cylinder/Crankcase

If, at any time, λ and β at the pipe ends have been determined, the cylinder gas properties which are related to the last time step cylinder state and dynamic pressure wave action in the inlet, transfer and exhaust pipes can be obtained through a thermodynamic analysis of an open system. The choice of control volumes is illustrated in Fig. 3.15. Control volumes 1 and 2 are connected to each other through a transfer pipe during the scavenging period.

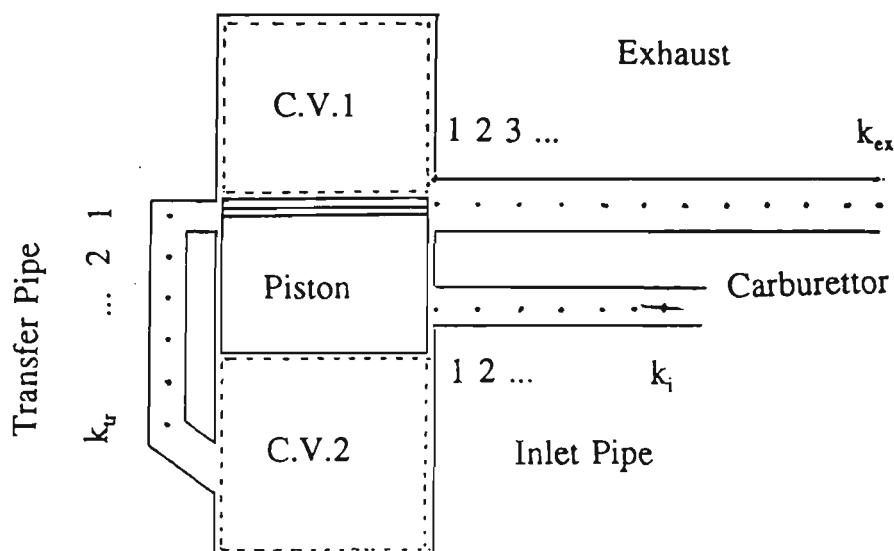


Fig. 3.15 Control volume for open thermodynamic and gas dynamic cycle analysis

First law applied to C.V.1 (that is, the engine cylinder) during the open cycle:

$$\frac{dQ}{dt} = \frac{dE_{cv1}}{dt} + \left(h_e + \frac{1}{2}u_e^2 \right) \frac{dm_e}{dt} - \left(h_{tr} + \frac{1}{2}u_{tr}^2 \right) \frac{dm_{tr}}{dt} + \frac{dW}{dt} \quad (3.96)$$

The discretized form of equation 3.96 during a particular time step (1-2) may be approximated as:

$$\Delta Q^{(1-2)} = \Delta E_{cv1}^{(1-2)} + \left[h_e^{(2)} + \frac{1}{2}(u_e^{(2)})^2 \right] \Delta m_e^{(1-2)} - \left[h_{tr}^{(2)} + \frac{1}{2}(u_{tr}^{(2)})^2 \right] \Delta m_{tr}^{(1-2)} + \Delta W \quad (3.97)$$

where

Q	=	heat transferred to or from the system (J/kg)
E	=	system internal energy (J/kg)
h	=	specific enthalpy of gas (J/kg)
u	=	gas particle velocity (m/s)
m	=	mass (kg)

the subscript

CV	=	state in control volume
e	=	state of exhaust gas
tr	=	state of scavenging gas
e _{pipe}	=	state in exhaust pipe
0	=	reference state

and superscript

(1-2)	=	during time step 1 to 2
(1)	=	at time step 1 (old)
(2)	=	at time step 2 (new)

In equation (3.97), the specific enthalpy and the specific kinetic energy at time step 2 are

used to represent the mean specific enthalpy and kinetic energy during time step (1-2), that is,

$$h_e^{(2)} \approx \frac{h_e^{(1)} + h_e^{(2)}}{2}$$

$$h_{tr}^{(2)} \approx \frac{h_{tr}^{(1)} + h_{tr}^{(2)}}{2}$$

$$\frac{1}{2}(u_e^{(2)})^2 \approx \frac{1}{4}[(u_e^{(1)})^2 + (u_e^{(2)})^2]$$

$$\frac{1}{2}(u_{tr}^{(2)})^2 \approx \frac{1}{4}[(u_{tr}^{(1)})^2 + (u_{tr}^{(2)})^2]$$

The evaluation of each term in equation (3.97) is detailed below:

3.10.1.1 Evaluation of Heat Transfer to the System During Time Step (1-2), $\Delta Q^{(1-2)}$

$\Delta Q^{(1-2)}$ is zero when the system is adiabatic. It may be specified further by an equation proposed by Annand [53]. As the heat transfer during the gas exchange period is small compared with the combustion period, it is assumed that $\Delta Q^{(1-2)} = 0$ in this study.

3.10.1.2 Evaluation of System Internal Energy Change During Time Step (1-2), $\Delta E_{cv1}^{(1-2)}$

Assuming the gas we deal with is a perfect gas and its specific heat is temperature dependent only, this term is then evaluated as

$$\Delta E_{cvl}^{(1-2)} = C_{v,cv1}^{(2)} \cdot m_{cv1}^{(2)} \cdot T_{cv1}^{(2)} - C_{v,cv1}^{(1)} \cdot m_{cv1}^{(1)} \cdot T_{cv1}^{(1)} \quad (3.98)$$

where C_v is the specific heat at constant volume,

$$C_{v,cv1} = f(T_{cv1})$$

3.10.1.3 Evaluation of Specific Outflow Enthalpy at $t = t_2$, $h_e^{(2)}$

As the flow through port can be approximately treated as steady flow, the energy equation which governs port/pipe flow may be expressed as

$$h_{cv1}^{(2)} + \frac{1}{2}(u_{cv1}^{(2)})^2 = h_e^{(2)} + \frac{1}{2}(u_e^{(2)})^2 \quad (3.99)$$

As the gas particle velocity in the cylinder is much less compared to the velocity in the pipe, the cylinder state can be regarded as stagnation. For a perfect gas, equation (3.99) becomes

$$C_{p,cv1}^{(2)} \cdot T_{cv1}^{(2)} = C_{p,e}^{(2)} \cdot T_e^{(2)} + \frac{1}{2}(U_e^{(2)})^2 \quad (3.100)$$

C_p is the specific heat of gas at constant pressure.

If λ and β are Riemann variables at t_2 , at the first mesh node in the exhaust pipe, then from equation (3.62), the velocity of exhaust gas, $u_e^{(2)}$, is:

$$u_e^{(2)} = \left(\frac{\lambda - \beta}{\gamma - 1} \right) a_{0,e}^{(2)} \quad (3.101)$$

The superposition temperature of exhaust, $T_e^{(2)}$, is determined by equation (3.64)

$$\begin{aligned}
T_e^{(2)} &= T_{0,e}^{(2)} \left(\frac{\lambda + \beta}{2} \right)^2 \\
&= \frac{(a_{0,e}^{(2)})^2}{\gamma R} \left(\frac{\lambda + \beta}{2} \right)^2
\end{aligned}
\tag{3.102}$$

Substituting $u_e^{(2)}$ and $T_e^{(2)}$ into equation (3.100), gives the reference speed of sound in the exhaust, $a_{0,e}^{(2)}$,

$$a_{0,e}^{(2)} = \sqrt{\frac{4 \gamma R \cdot C_{p,cvl}^{(2)} \cdot T_{cvl}^{(2)}}{C_{p,e}^{(2)} \cdot (\lambda + \beta)^2 + 2 \gamma R \left(\frac{\lambda - \beta}{\gamma - 1} \right)^2}}
\tag{3.103}$$

The superposition temperature of the exhaust is found by substituting equation (3.103) into (3.102):

$$T_e^{(2)} = \frac{C_{p,cvl}^{(2)} \cdot T_{cvl}^{(2)} \cdot (\lambda + \beta)^2}{C_{p,e}^{(2)} \cdot (\lambda + \beta)^2 + 2 \gamma R \left(\frac{\lambda - \beta}{\gamma - 1} \right)^2}
\tag{3.104}$$

Therefore, the specific enthalpy at t_2 may be expressed as

$$\begin{aligned}
h_e^{(2)} &= C_{p,e}^{(2)} \cdot T_e^{(2)} \\
&= \frac{C_{p,e}^{(2)} \cdot C_{p,cvl}^{(2)} \cdot T_{cvl}^{(2)} \cdot (\lambda + \beta)^2}{C_{p,e}^{(2)} \cdot (\lambda + \beta)^2 + 2 \gamma R \left(\frac{\lambda - \beta}{\gamma - 1} \right)^2}
\end{aligned}
\tag{3.105}$$

The exhaust reference temperature at t_2 , $T_{0,e}^{(2)}$, is:

$$T_{0,e}^{(2)} = \frac{T_e^{(2)}}{\left(\frac{\lambda + \beta}{2}\right)^2} \quad (3.106)$$

The exhaust reference temperature $T_{0,e}^{(2)}$ obtained from equation (3.106) is used to calculate the gas density and velocity so that the mass flow out of the cylinder can be calculated. This temperature is calculated at each time step. However, as the pipe flow is assumed isentropic, the reference temperature in the exhaust pipe, $T_{0,epipe}$, is constant and cannot vary with time and space. There is thus a discontinuity in the reference temperature between the port/pipe interface (first node in the pipe) and the rest of the pipe. For a realistic mass flow estimation for cylinder (or crankcase) inflow and outflow, in this study, $T_{0,epipe}$ is kept constant but $T_{0,e}^{(2)}$ is allowed to change as the cylinder state changes. This assumption is identically applicable to all other port/pipe interfaces and pipes attached to them.

3.10.1.4 Evaluation of Specific Kinetic Energy of Exhaust at $t=t_2$, $0.5[u_e^{(2)}]^2$

The exiting velocity of gas at the exhaust port $u_e^{(2)}$, based on equation (3.101) and (3.103), may be evaluated using

$$u_e^{(2)} = \frac{(\lambda - \beta)}{\gamma - 1} \cdot \sqrt{\frac{4\gamma R \cdot C_{p,cvI}^{(2)} \cdot T_{cvI}^{(2)}}{C_{p,e}^{(2)} \cdot (\lambda + \beta)^2 + 2\gamma R \left(\frac{\lambda - \beta}{\gamma - 1}\right)^2}} \quad (3.107)$$

λ and β are Riemann variables at t_2 , at the first mesh node in the exhaust pipe. The specific kinetic energy of exhaust gas is determined by using this velocity of the exhaust stream.

3.10.1.5 Evaluation of Outflow Mass Increment During the Time Step (1-2).

$$\Delta m_e^{(1-2)}$$

The superposition density of the exhaust is found by equation (3.63),

$$\begin{aligned} \rho_e^{(2)} &= \left(\frac{\lambda + \beta}{2} \right)^5 \cdot \rho_{0,e}^{(2)} \\ &= \left(\frac{\lambda + \beta}{2} \right)^5 \frac{P_0}{R \cdot T_{0,e}^{(2)}} \end{aligned} \quad (3.108)$$

therefore

$$\Delta m_e^{(1-2)} \approx C_D \cdot \rho_e^{(2)} \cdot u_e^{(2)} \cdot A_e \cdot \Delta t \quad (3.109)$$

In the last equation, C_D is the coefficient of discharge and A_e is the exhaust pipe area at the port.

3.10.1.6 Evaluation of Specific Inflow Enthalpy at $t = t_2$, $h_{tr}^{(2)}$

Since the length of the transfer paths is relatively short and the cross sectional area change of this path is insignificant, with the assumption of steady flow in transfer pipes, the energy equation for the transfer pipe reduces to:

$$h_{tr}^{(2)} \approx h_{cv2}^{(2)} \quad (3.110)$$

For a perfect gas

$$T_{tr}^{(2)} = T_{cv2}^{(2)}$$

Inflow gas reference temperature, $T_{0,tr}^{(2)}$:

$$T_{0,tr}^{(2)} = \frac{T_{cv2}^{(2)}}{\left(\frac{\lambda + \beta}{2}\right)^2} \quad (3.111)$$

λ and β are Riemann variables at t_2 , at the first mesh node in the transfer pipe, Fig. 3.15.

The reference sound velocity of gas in the transfer pipe at t_2 , $a_{0,tr}^{(2)}$, is:

$$a_{0,tr}^{(2)} = \sqrt{\gamma \cdot R \cdot T_{0,tr}^{(2)}} \quad (3.112)$$

3.10.1.7 Evaluation of Specific Kinetic Energy of Scavenging Air at $t=t_2$, $0.5[u_{tr}^{(2)}]^2$

The entering velocity of the fresh charge at the transfer port $u_{tr}^{(2)}$, based on equation 3.62, is given by

$$u_{tr}^{(2)} = \frac{(\lambda - \beta)}{\gamma - 1} \cdot a_{0,tr}^{(2)} \quad (3.113)$$

λ and β are Riemann variables at t_2 , at the first mesh node in the transfer pipe. The specific kinetic energy of transfer gas is determined by this velocity of fresh charge stream.

3.10.1.8. Evaluation of Inflow Mass Increment During Time Step 1-2, $\Delta m_{tr}^{(1-2)}$

As the reference density of inflow gas, $\rho_{0,tr}^{(2)}$, is:

$$\rho_{0,tr}^{(2)} = \frac{P_0}{R \cdot T_{0,tr}^{(2)}}$$

and

and

$$\begin{aligned} \rho_{tr}^{(2)} &= \left(\frac{\lambda + \beta}{2} \right)^5 \cdot \rho_{0,tr}^{(2)} \\ &= \left(\frac{\lambda + \beta}{2} \right)^5 \cdot \frac{P_0}{R \cdot T_{0,tr}^{(2)}} \end{aligned} \quad (3.114)$$

thus

$$\Delta m_{tr}^{(1-2)} \approx C_D \cdot \rho_{tr}^{(2)} \cdot C_{tr}^{(2)} \cdot A_{tr} \cdot \Delta t \quad (3.115)$$

The new cylinder mass $m_{cvl}^{(2)}$ in equation (3.98) is now

$$m_{cvl}^{(2)} = m_{cvl}^{(1)} + \Delta m_{tr}^{(1-2)} - \Delta m_e^{(1-2)} \quad (3.116)$$

3.10.1.9 Evaluation of Work Done on or by Piston During Time Step (1-2), $\Delta W^{(1-2)}$

$$\begin{aligned} \Delta W^{(1-2)} &\approx \bar{p} \Delta V \\ &= \frac{1}{2} (p_{cvl}^{(1)} + p_{cvl}^{(2)}) \cdot (V_{cvl}^{(2)} - V_{cvl}^{(1)}) \end{aligned} \quad (3.117)$$

3.10.1.10 Final Determination of Cylinder State

By substituting equations (3.98)-(3.117) into the energy equation, (3.97), the new cylinder state is determined by:

$$T_{cvl}^{(2)} = \frac{\Delta Q^{(1-2)} + \Delta H_{tr}^{(2)} - \Delta H_e^{(2)} + m_{cvl}^{(1)} \cdot C_v^{(1)} \cdot T_{cvl}^{(1)} - 0.5 (p_{cvl}^{(1)} + p_{cvl}^{(2)}) \cdot (V_{cvl}^{(2)} - V_{cvl}^{(1)})}{m_{cvl}^{(2)} \cdot C_v^{(2)}} \quad (3.118)$$

and

$$P_{cv1}^{(2)} = \frac{m_{cv1}^{(2)} \cdot R \cdot T_{cv1}^{(2)}}{V_{cv1}^{(2)}} \quad (3.119)$$

where

$$\Delta H_e^{(2)} = [h_e^{(2)} + 0.5(u_e^{(2)})^2] \cdot \Delta m_e^{(1-2)} \quad (3.120)$$

$$\Delta H_{tr}^{(2)} = [h_{tr}^{(2)} + 0.5(u_{tr}^{(2)})^2] \cdot \Delta m_{tr}^{(1-2)} \quad (3.121)$$

The above analysis is almost exactly applicable to the second control volume, the crankcase.

3.10.2 Reflections Due to Non-Isentropic Behaviour at the First Node

The non-uniform distribution of gas reference temperatures in the pipe causes the non-uniform distribution of the reference speed of sound, hence pressure waves may suffer partial reflections as they traverse such regions of non-uniform reference temperature. This is illustrated in Fig. 3.16. Assuming that the gas superposition pressure and particle velocity on each side of a fluid in the region are identical, following Zucrow *et al* [51], the equations given below hold:

$$\lambda' = \lambda + d\lambda \quad (3.122)$$

$$\beta' = \beta + d\beta \quad (3.123)$$

$$\frac{\lambda' + \beta}{2} = \frac{\lambda + \beta'}{2} \quad (3.124)$$

(pressure assumption)

$$a_0 \frac{\lambda - \beta'}{\gamma - 1} = (a_0 + da_0) \frac{\lambda' - \beta}{\gamma - 1} \quad (3.125)$$

(velocity assumption)

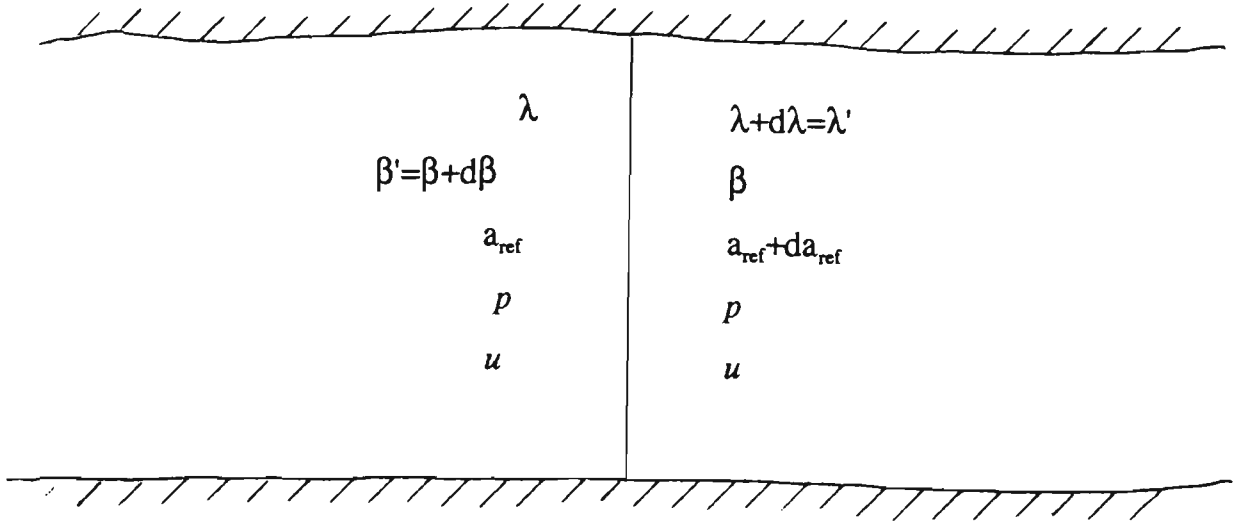


Fig. 3.16 Pressure wave reflection at reference temperature non-uniformity

Equations (3.122)-(3.125) are a set of linear simultaneous equations. From equations (3.122)-(3.124), we obtain:

$$d\lambda = d\beta \quad (3.126)$$

From equations (3.125) and (3.126), neglecting the second order term, we get

$$d\lambda = \frac{\beta - \lambda}{2a_0} \cdot da_0 \quad (3.127)$$

$$d\beta = \frac{\beta - \lambda}{2a_0} \cdot da_0 \quad (3.128)$$

The effect of the non-uniformity of the reference temperature over a finite mesh volume is then found by integrating equations (3.127) and (3.128) over their respective characteristics, see Fig. 3.17.

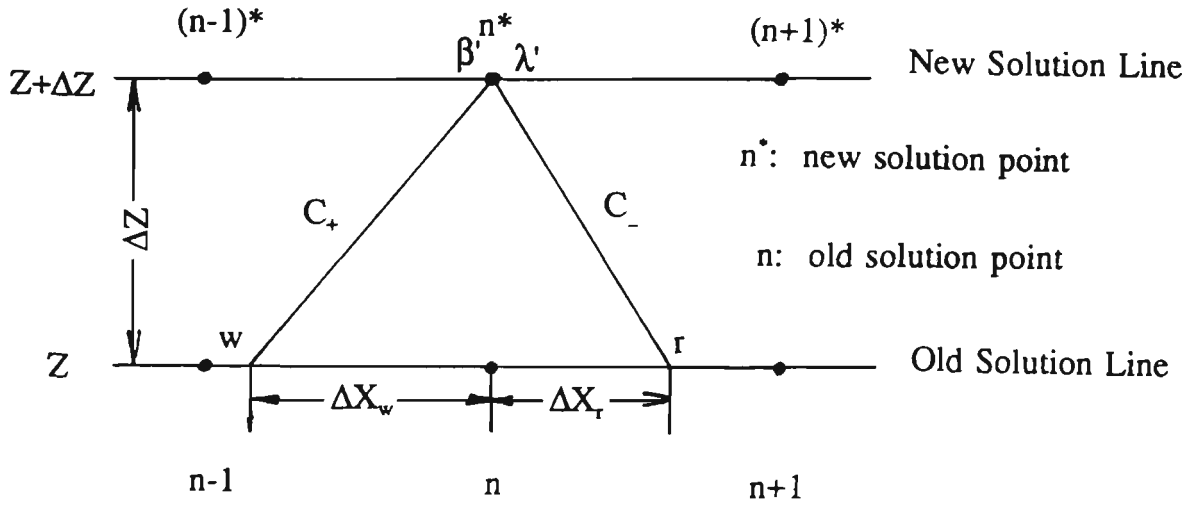


Fig. 3.17 Evaluation of the effect of non-uniform temperature.

Along the C_+ characteristic,

$$\begin{aligned}\Delta \lambda &= \int_w^{n^*} d\lambda \\ &= \int_w^{n^*} \frac{\beta - \lambda}{2a_0} \cdot da_0\end{aligned}\quad (3.129)$$

Similarly, along the C_- characteristic,

$$\begin{aligned}\Delta \beta &= \int_r^{n^*} d\beta \\ &= \int_r^{n^*} \frac{\beta - \lambda}{2a_0} \cdot da_0\end{aligned}\quad (3.130)$$

Hence the new Riemann variables after reflections at a mesh node become:

$$\lambda' = \lambda + \Delta \lambda \quad (3.131)$$

$$\beta' = \beta + \Delta \beta \quad (3.132)$$

where λ and β are already evaluated by equations (3.87) and (3.88) (as λ_n and β_n in those equations). $\Delta \lambda$ and $\Delta \beta$ are evaluated using equations (3.129) and (3.130).

Equations (3.131) and (3.132) imply that the final value of the Riemann variable at a mesh node is the sum of its "normal" value plus the modification caused by the non-uniform distribution of reference temperatures. Apparently, when a_0 is the same everywhere in the pipe, $\Delta \lambda = \Delta \beta = 0$.

As the gas reference temperature at the first node (port/pipe interface) is different from the other mesh nodes of the pipe, the partial reflections of C_- pressure wave (C_+ pressure wave), upon the C_- (C_+) characteristic's arrival at the first mesh node (the second mesh node), are taken into account. This is demonstrated in Fig. 3.18.

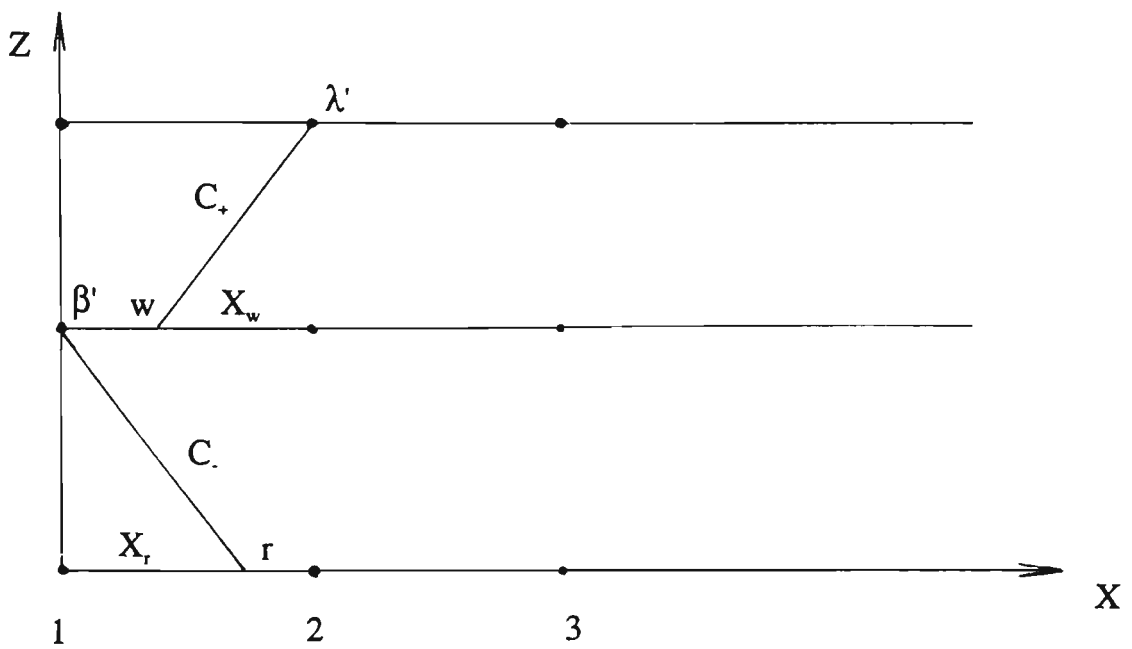


Fig. 3.18 Characteristics at port

We next assume that the reference speed of sound at node 1 varies linearly to the reference sonic speed at node 2, as illustrated in Fig. 3.19.

As X_r is known from equation (3.82), a_0 at r is found by linear interpolation:

$$a_{0,r} = a_{0,e} + \frac{X_r}{X} \cdot (a_{0,pip} - a_{0,e}) \quad (3.133)$$

Equation (3.130) then becomes:

$$\begin{aligned}\Delta \beta &= \int_r^{1'} \frac{\beta - \lambda}{2a_0} \cdot da_0 \\ &\approx \frac{1}{4} \left[\left(\frac{\beta - \lambda}{a_0} \right)_r + \left(\frac{\beta - \lambda}{a_0} \right)_{1'} \right] (a_{0,1'} - a_{0,r})\end{aligned}\quad (3.134)$$

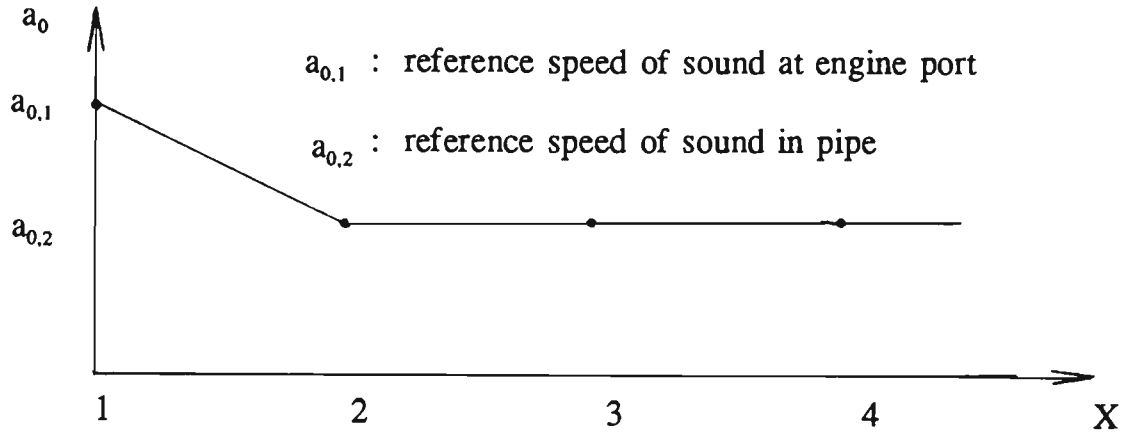


Fig. 3.19 Variation of reference speed of sound in exhaust pipe

Substitute equation (3.134) into equation (3.132) and β' is finally determined.

Taking the same action to find X_w by equation (3.81), then linear interpolation to find a_0 at w gives:

$$a_{0,w} = a_{0,pipe} - \frac{X_w}{X} (a_{0,pipe} - a_{0,e}) \quad (3.135)$$

$\Delta \lambda$ is thus

$$\begin{aligned}\Delta \lambda &= \int_w^{2''} \frac{\beta - \lambda}{2a_0} \cdot da_0 \\ &\approx \frac{1}{4} \left[\left(\frac{\beta - \lambda}{a_0} \right)_w + \left(\frac{\beta - \lambda}{a_0} \right)_{2''} \right] (a_{0,2''} - a_{0,w})\end{aligned}\quad (3.136)$$

Substituting equation (3.136) into equation (3.131) determines λ' .

3.10.3 Computational Procedure for Flow at Port/Pipe Boundary

The solution of $p_{cv1}^{(2)}$ and $T_{cv1}^{(2)}$ (pressure and temperature in control volume 1 at the new time step) relies heavily on the solution of λ and β (Riemann variables at engine ports at the new time step). However as discussed in section 3.9, the solution of the characteristics at the engine ports is dependent on the instantaneous cylinder state. Therefore, $p_{cv1}^{(2)}$, $T_{cv1}^{(2)}$ and λ are interconnected and cannot be solved for directly. Iteration is used to solve for $p_{cv1}^{(2)}$, $T_{cv1}^{(2)}$ and λ . The computation procedure used was as follows:

- 1 Assuming $p_{cv1}^{(2)} = p_{cv1}^{(1)}$, $\beta_1' = \beta_1$, use the method outlined in section 3.9 to calculate λ at t_2 , $\lambda^{(2)}$.
- 2 Calculate β_1' using equations (3.130) and (3.132).
- 3 Use $p_{cv1}^{(1)}$, $p_{cv2}^{(1)}$ and $T_{cv1}^{(1)}$ to evaluate $h_c^{(2)}$, $h_{tr}^{(2)}$, $u_c^{(2)}$, $u_{tr}^{(2)}$, $T_{ref,c}^{(2)}$, $T_{ref,tr}^{(2)}$, $\Delta m_c^{(1-2)}$, $\Delta m_{tr}^{(1-2)}$ and $\Delta W^{(1-2)}$.
- 4 Compute $T_{cv1}^{(2)}$ and $p_{cv1}^{(2)}$ by substituting all terms obtained from step 3 into equations (3.118) and (3.119).
- 5 Use renewed $p_{cv1}^{(2)}$ and β_1' to calculate newer λ .
- 6 Use renewed $p_{cv1}^{(2)}$, $p_{cv2}^{(2)}$ and $T_{cv1}^{(2)}$ to calculate all terms listed in step 3 again.
- 7 Compute newer $p_{cv1}^{(2)}$ and $T_{cv1}^{(2)}$ by substituting all terms from step 6 into equations (3.118) and (3.119).
- 8 If $p_{cv1}^{(2)}$ between two successive iterations falls below the specified tolerance, stop iteration or
- 9 Repeat steps 5-8.
- 10 Calculate λ_2' using equations (3.129) and (3.131).

3.11 Verification of Mass Balance

To avoid an erroneous conclusion being drawn from the calculation, the conservation of mass must be examined to ensure the numerical correctness of the solution. The law of continuity requires that when the calculation reaches its steady state, the mass the engine intakes and discharges over one complete simulation cycle should be identical. In the program, six control points were added at the locations indicated in Fig. 3.20 to evaluate the quality of the numerical solution for port/pipe flow.

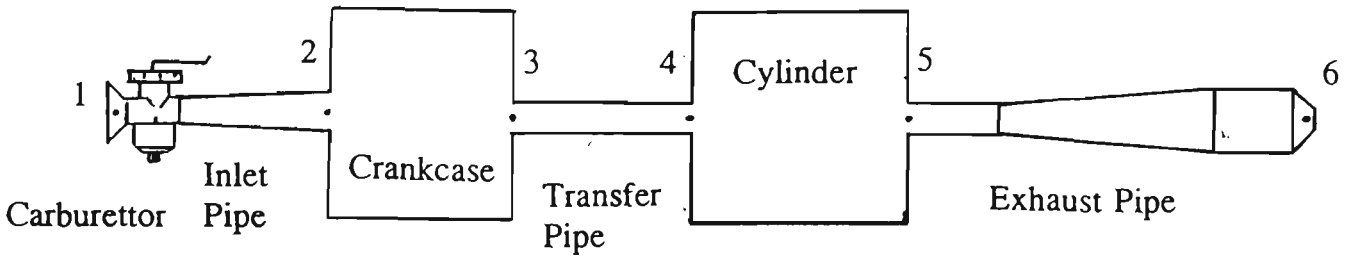


Fig. 3.20 Control points for mass balance check

3.11.1 Mass Flow Balance in Pipes

The mass entering and leaving the ends of a pipe during any time step is:

$$(\Delta m_i)_{end1} = (\rho u A)_{end1} \Delta t_i \quad (3.137)$$

$$(\Delta m_i)_{end2} = (\rho u A)_{end2} \Delta t_i \quad (3.138)$$

ρ, u and A are gas density, velocity and pipe area at the appropriate end, where (when $\gamma=1.4$):

$$\rho = \left(\frac{\lambda + \beta}{2} \right)^5$$

$$u = \frac{\lambda - \beta}{\gamma - 1}$$

The sums for $(\Delta m_i)_{end1}$ and $(\Delta m_i)_{end2}$ over a complete engine cycle should be equal,

$$\sum_{i=1}^k (\Delta m_i)_{end1} = \sum_{i=1}^k (\Delta m_i)_{end2} \quad (3.139)$$

k is the total time step for one engine cycle,

$$\sum_{i=1}^k \Delta t_i = \frac{60}{RPM} \quad (3.140)$$

Define the mass flow imbalance in pipes, ϵ ,

$$\epsilon = 1 - \frac{\sum_{i=1}^k (\Delta m_i)_{end2}}{\sum_{i=1}^k (\Delta m_i)_{end1}} \quad (3.141)$$

Ideally, ϵ for every pipe should approach zero.

3.11.2 Mass Balance Across Engine Ports

Define mass flow ratio at port K as:

$$K = \frac{\sum_{i=1}^k (\Delta m_i)_{port}}{m_0} \quad (3.142)$$

where m_0 is the air mass in sweep volume at reference condition.

The summation for every port over a complete engine cycle should be equal in an ideal situation, that is,

$$K_{delivery} = K_{scavenging} = K_{exhaust}$$

CHAPTER 4

COMPUTER SIMULATION

4.1 Model Description

The computer two-stroke engine simulation model is based on that developed by Blair [8] with the modifications which have been addressed in Chapter 3. The modified coding is capable of simulating a crankcase compressed, piston port timed, two-stroke engine equipped with expansion chambers under various operating conditions. The engine performance characteristics, pressure-crank angle history, mass imbalance and the one dimensional unsteady flow field variables in pipes can be predicted.

To begin the calculation, one must first input a detailed description of engine and related pipe geometry data which characterises the real engine configuration as well as the operating condition data under which the engine is designed to run. In this work, all such data was measured from the YAMAHA MT-110 two-stroke engine test rig. All input data are classified into following groups:

1. Geometric data, which include:
bore, stroke, connecting rod length, port configuration and timing, model for scavenging, pipe dimensions;
2. Gas flow and operating condition data, including:
combustion data, air-fuel ratio, engine speeds, throttle position, coefficient of discharge, initial conditions in cylinder, crankcase and pipes, boundary conditions at cylinder/pipe, crankcase/pipe and atmosphere/pipe interfaces.

The program can predict various parameters such as:

1. Static engine performance data, for example, scavenging efficiency, torque and BSFC.

2. Dynamic data, such as, thermodynamic property histories and mass flow rates.
3. Mass imbalance and so on.

4.2 Model Assumptions

Some assumptions and simplifications have been made in order that they best reflect the characteristic aspects of the real engine and suit the theoretical model as well. The necessary assumptions made for carrying out the calculations are listed below:

1. The pipe is straight and its length is defined as the distance between the two boundaries:
 - a) For the exhaust pipe, the two boundaries refer to the piston face and the exhaust pipe exit.
 - b) For the transfer pipe, the boundaries refer to the piston face and the transfer pipe entrance which is located in the crankcase.
 - c) For the inlet pipe, the boundaries are taken as the piston face and the throttle body in the carburettor.
2. For a curved header pipe which is commonly found in motorcycle and go-kart engine exhaust systems, the pipe centre line length between the two end sections is regarded as an equivalent length.
3. In the case of a multiple, parallel pipe system, such as the transfer pipes, the areas of the corresponding sections are summed up to give an equivalent area.
4. The flow through the pipe boundaries is treated as flow through an orifice. The coefficient of discharge C_D is conventionally defined as:

$$C_D = \frac{\textit{real mass flow}}{\textit{theoretical mass flow}}$$

Annand [54] has demonstrated that the coefficient of discharge C_D is a function of port

opening fraction and pressure ratio. However in the current study, C_D is simplified as much as possible by regarding it as constant for all the pipe boundaries considered, following Blair in [8]. Tables 4.1 summarise the values of C_D employed in the program.

Table 4.1. Coefficient of discharge at engine port

PORT	NORMAL	REVERSE
EXHAUST	0.75	0.75
TRANSFER	0.75	0.75
INLET	0.75	0.90

- The shape of the port is rectangular with rounded corners. The axial inclination angle θ_{ax} , and the tangential inclination angle θ_{tan} are taken as the inflow jet angles, as depicted in Fig. 4.1.
- The flow through the port is one-dimensional uniform and plug flow. The effective port area is defined as the area which is perpendicular to the flow jets. It is the product of the effective port height h and the effective port width l , which are the projection of the geometric port height h_0 and width l_0 in the assumed flow direction, less the area of the rounded corners:

$$h = h_0 \cos \theta_{ax}$$

$$l = l_0 \cos \theta_{tan}$$

$$A_{port} = hl - 0.858r^2$$

In the above equations,

θ_{ax} = axial inclination angle

θ_{tan} = tangential inclination angle

r = corner radius of port

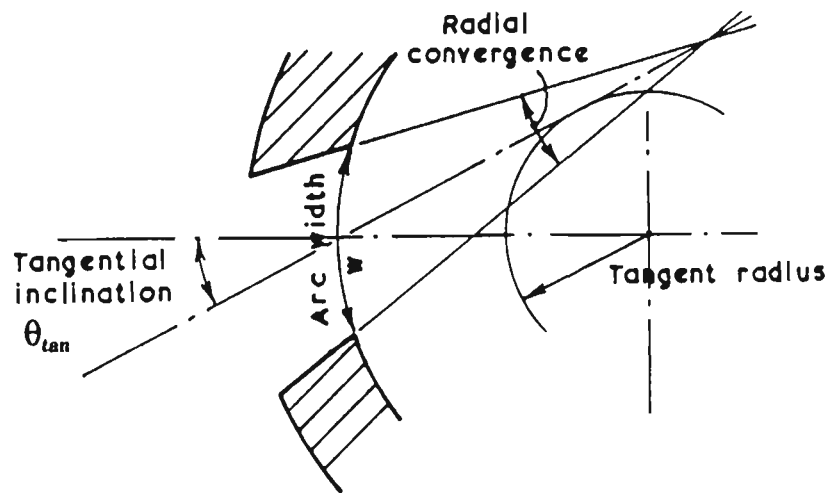
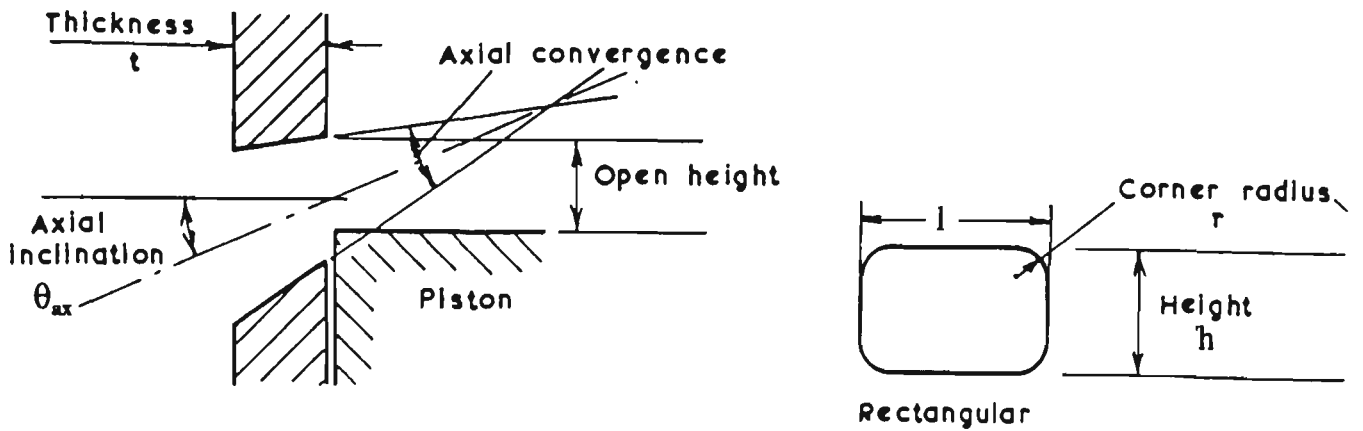


Fig. 4.1 Geometric parameter of engine port

7. The exhaust port and transfer ports are fully exposed by the piston's timing edge at BDC, while the inlet port is fully opened at TDC by the piston skirt.
8. The information of the in-cylinder scavenging quality (scavenging quality without the influence of wave action) is obtained from the "single cycle test", as suggested by Blair [8]. As first hand information of this kind was not readily available, the selection of the scavenging type was based on the results from the single cycle test published in [8]. Because the test engine cylinder has a two-scavenging port layout, YAM6 scavenging type was chosen for the computer simulation.

The selected scavenging type was used through the entire speed range during the numerical modelling of engine performance. This is because the published experiments of Sher [34] showed that the scavenging efficiency - scavenging ratio characteristic does not depend on engine speed very much but on the engine design. The primary parameter which affects the scavenging efficiency is the scavenging ratio and the mechanism of scavenging does not seem to change with engine speed, concluded also by Sher in another work [55].

9. As the exhaust temperature is dependent on engine speed, different values of exhaust temperature data for different speeds should be entered into the program during calculation. However, as the speed of sound is a square root function of temperature, it is simply assumed here that the gas temperature in the exhaust pipe, T_{ex} , is:

$$T_{ex} = 350 \text{ }^{\circ}\text{C for the speed range} = 2200 - 2900 \text{ RPM}$$

$$T_{ex} = 450 \text{ }^{\circ}\text{C for the speed range} = 3000 - 4400 \text{ RPM}$$

10. To ensure numerical stability, the dimensionless time step predicted by the Courant-Friedrichs-Lewy (CFL) stability criterion (see section 3.6) was multiplied by a factor less than one, in this study 0.95. This ensures numerical stability. The proportionally related quantities, the crank angle step and the dimensional time step were multiplied by the same factor.
11. The choice of the mesh length Δx has an important influence on the pipe flow calculation. Although a large mesh length may reduce computation time, it may introduce more computational errors. As the derivations in section 3.7 show, an accurate application of the trapezoidal rule of integration depends on the choice of the dimensionless time increment ΔZ , it is thus understandable that Δx should be kept as small as feasible. A number of runs has been performed with the same input data file except for the mesh length. By comparing the outcomes for different mesh lengths, a mesh length of 10 mm, rather than 30 mm as recommend by Blair [8] was selected.

12. The combustion process was simplified as a heat addition process in a closed thermodynamic system. A simple combustion model adequate for engine simulation is the heat release model which correlates the heat release rate and the crank angle. The model was deduced from the cylinder pressure trace analysis and was used by Blair[8]. Corrections and modifications were made to Blair's model, because part of the assumed combustion profile discussed by Blair [8] was omitted from the code. This meant that 17% of the total heat input had not been taken into account in Blair's thermodynamic calculations. Furthermore, a constant specific heat ratio for air was used in closed thermodynamic system calculations where temperature variations between 2000K and 3000K were common. Blair's code was thus modified to include the missing profile and introduce a temperature dependent specific heat ratio.

The modified engine simulation program can continuously calculate the model engine performance characteristics. The speed range of 2200 - 4400 RPM and marching step of 100 RPM have been used in the calculations. The reason that the calculation stops at 4400 RPM was due to the limitation of the dynamometer capacity at the test throttle position used in the experiment.

4.3 Discussion of the Computer Simulation Results

The dimension of the exhaust pipe for both experimental and numerical simulation in this project is illustrated in Fig. 4.2. The mid-parallel section, L_3 , is extendable.

Table 4.2 The dimensions of the exhaust pipe for simulation and experiment

	L_1	L_2	L_3	L_4	L_5
Length	130	281	various	352	152
Diameter	30	30 - 99	99	99 - 20	20

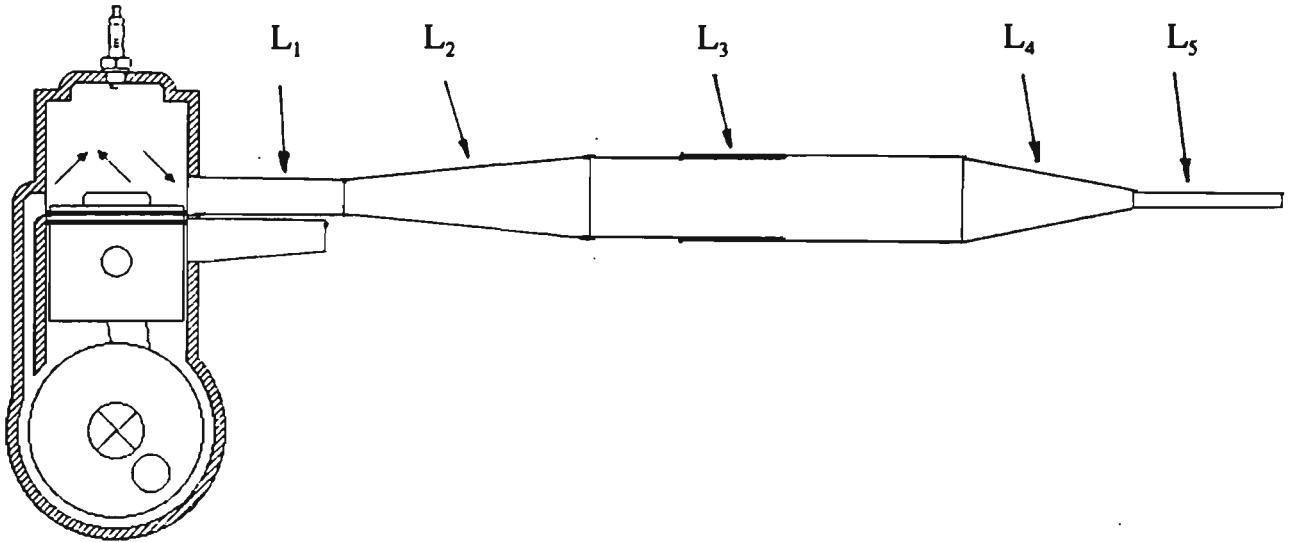


Fig. 4.2. The exhaust pipe for simulation and experiment

The engine torque curves for different lengths of expansion chamber (calculated) and for the box silencer (measured) are presented in Fig. 4.3. The lengths of L_3 were set to 240 mm, 330 mm, 400 mm, 480 mm and 550 mm, respectively.

It may be clearly seen that with an expansion chamber, the engine torque was significantly increased within the entire speed range simulated. The measure of such improvement is shown in Fig. 4.4. It was equally clear that the peaks of engine torque moved towards higher engine speeds when the length of the pipe was reduced. In contrast, there was no control to modify the engine external characteristics during engine operation with the original box silencer. As the engine and exhaust are usually designed for working under some well defined operating conditions, low performance figures and/or high fuel consumption results when the engine works under off-design conditions.

With an extendable exhaust expansion chamber, the speed range for high engine torques was widened as shown in Fig. 4.3. This demonstrates that the engine works effectively and efficiently at both high speeds and low speeds and its speed adaptability was much improved. According to Fig. 4.3, it is a simple matter to determine the length of L_3 to obtain the best engine performance when the speed requirement is known.

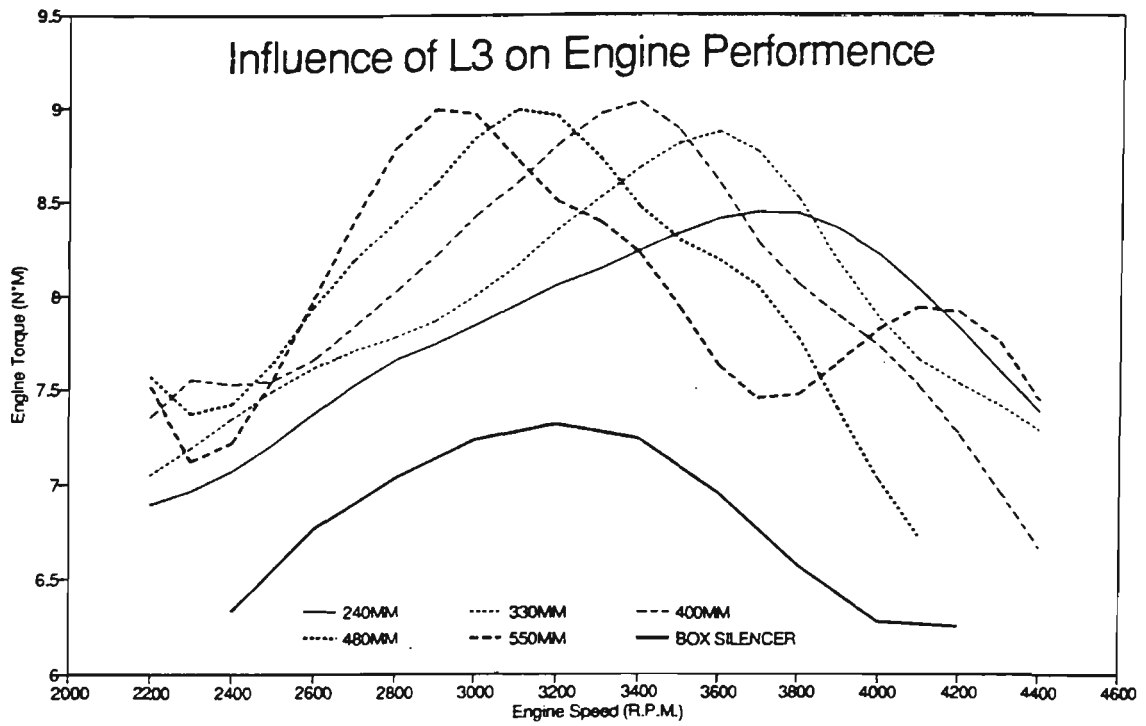


Fig. 4.3 Torque curve for various L3 settings

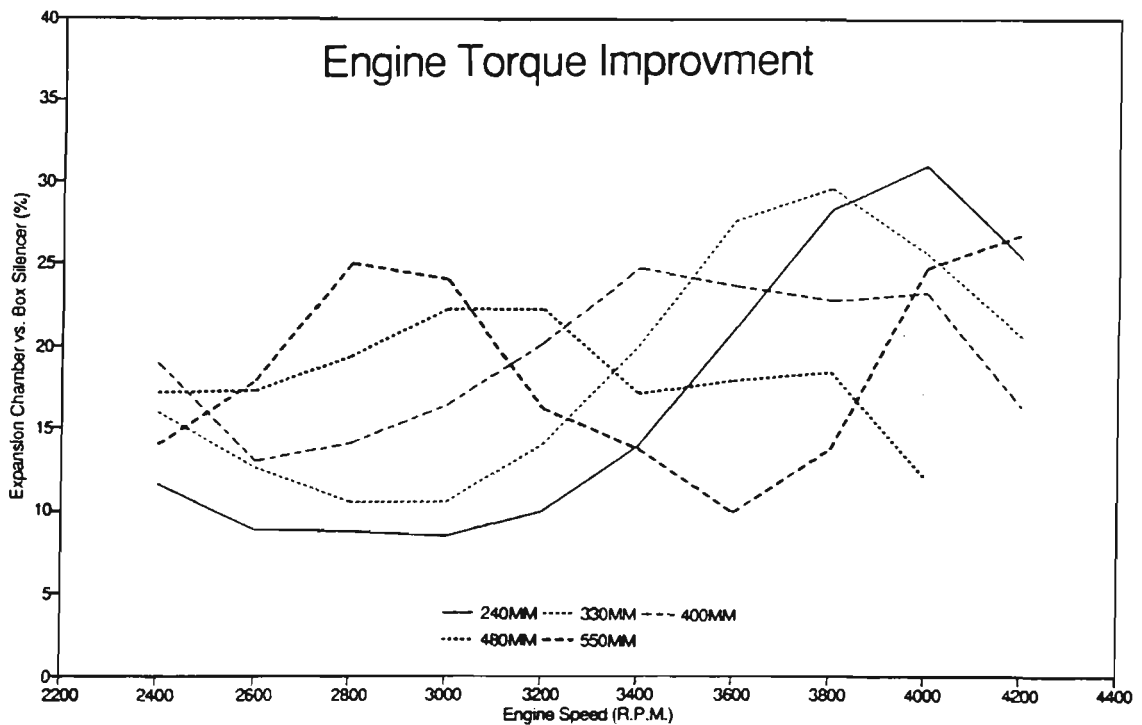


Fig. 4.4 Performance improvement (%) - extendable pipe vs. box silencer

The phenomenon is attributed to the unsteady gas dynamic effect in the two-stroke engine pipe/duct. The dynamic pressure wave action improves the scavenging quality hence engine performance can be explained by referring to the pressure trace analysis recorded at some sensitive locations. Fig. 4.5-4.9 shows calculated pressure versus crank angle diagrams. In the calculations, the mid-parallel section length L_3 was fixed at 400 mm, and the engine speeds are 2800, 3400 and 4400 revolutions per minute, respectively. In each diagram, the solid line represents the simulation of the engine running at 3400 RPM, the dashed line was for 2800 RPM and the dotted line for 4400 RPM. The performance data for all three speeds available from the calculation are listed in Table 4.2 below:

Table 4.3

SPEED (RPM)	POWER (kW)	BMEP (100kPa)	BSFC (g/kWH)	λ_d (%)	λ_s (%)	η_s (%)	η_s (%)
2800	2.4	4.8	520	76%	111%	74%	43%
3400	3.2	5.4	515	83%	118%	77%	48%
4400	3.0	3.9	629	73%	101%	71%	35%

4.3.1 Discussion of Calculated Wave Diagrams

Fig. 4.5 to 4.7 show records of the calculated instantaneous pressure in transfer duct and cylinder for a complete cycle and the pressure difference between the crankcase and the cylinder $p_{cc} - p_{cyl}$ from transfer port open to transfer port closed.

The pressure difference, $p_{cc} - p_{cyl}$, is the driving force for the scavenging flow. From Fig. 4.7, for speed = 3400 RPM, the cylinder blowdown period is not sufficient and at the moment of transfer port open, the cylinder pressure is still higher than the crankcase pressure. Therefore, there is a back flow of exhaust gas from the cylinder into the transfer duct.

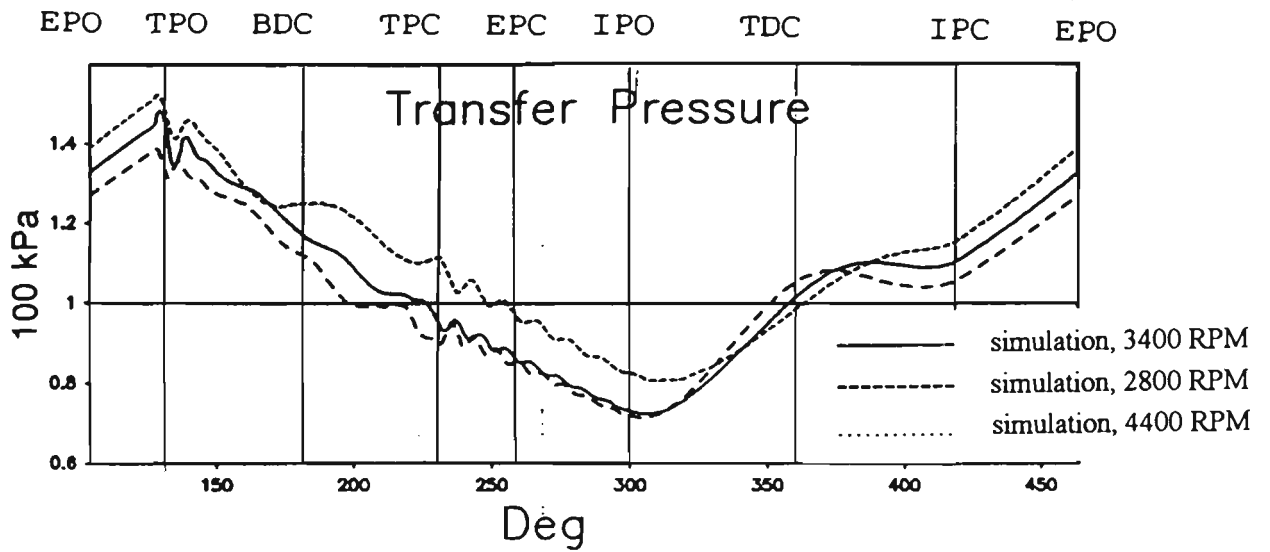


Fig. 4.5 Pressure variations at transfer port

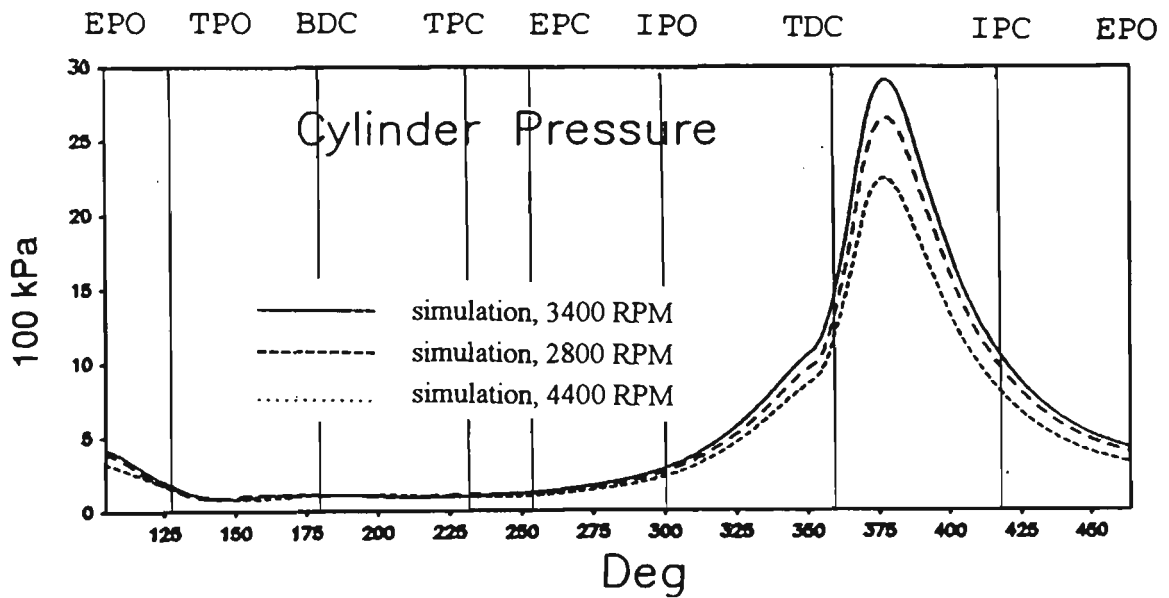


Fig. 4.6 Pressure variations in engine cylinder

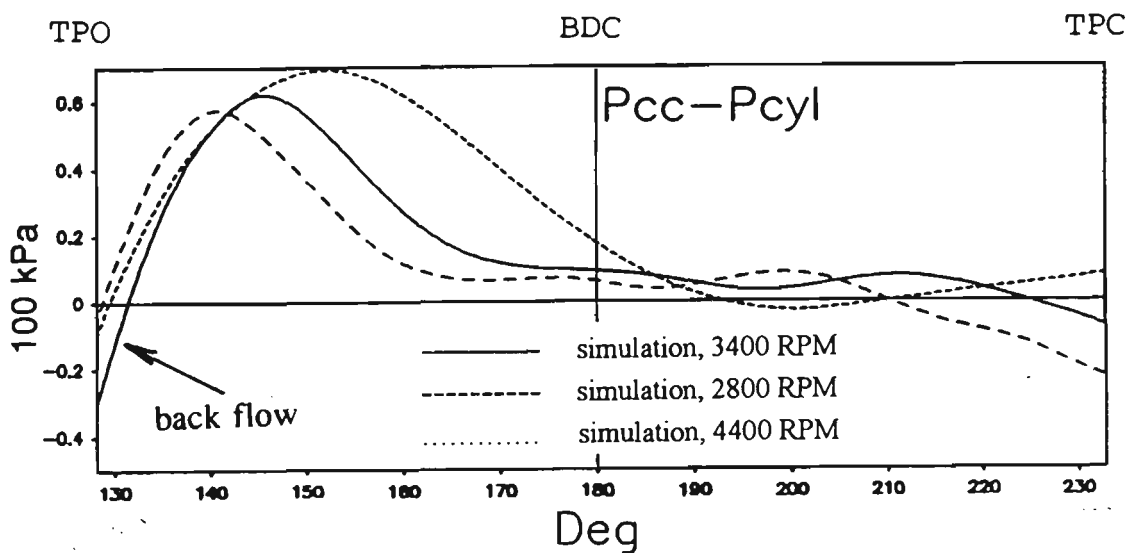


Fig. 4.7 Pressure difference $p_{cc} - p_{cyl}$ during TPO to TPC

The back flow finally ceases as the cylinder volume increase and the crankcase volume decrease, and the flow reverses its direction at about 5 degrees crank angle after the transfer port opens. The exhaust gas leaks into the transfer duct and is then forced back into the cylinder, followed by the actual commencement of the fresh charge scavenging the engine cylinder.

The pressure difference, $p_{cc} - p_{cyl}$, as well as the flow rate of the fresh charge keep increasing as the piston moves downwards; the pressure difference reaches its peak at about 35 degrees crank angle before bottom dead centre. At this crank angle, the cylinder pressure is virtually at its minimum, see Fig. 4.6, as a result of the valley of the suction pressure wave generated by the exhaust diffusive cone arriving at the exhaust port, helping extract the burnt cylinder contents from the previous engine cycle. This suction wave is superposed on the outgoing exhaust pulse (compression wave) and brings the pressure at the exhaust port down to about 25% lower than the atmospheric pressure as shown in Fig. 4.8. The $p_{cc} - p_{cyl}$ pressure difference then decreases as the filling and emptying process continues, however a positive pressure difference is always maintained. The fresh charge continues to enter the cylinder, but with a weakened strength until the transfer port closes.

By comparing with the one of the other two case from Fig. 4.7, at 2800 RPM, although the back flow at the commencement of the transfer port open is not evident, the pressure difference $p_{cc} - p_{cyl}$ reverses sign at 22 degrees crank angle before the transfer port closure. At this moment, as the velocity fields in both the transfer ducts and the cylinder are both well developed, back flow is unlikely. However, a significant amount of fresh air - fuel mixture may still be spilled into the transfer duct with a phase lag, subjected to the strong pressure gradient across the transfer port. Although this amount of charge is not lost and will return to the cylinder in the next engine cycle, the possible trapped cylinder content does fall and a lower engine torque /BMEP results.

At 4400 RPM from Fig. 4.7, the pressure difference between the crankcase and the cylinder, $p_{cc} - p_{cyl}$, is greater than it at both 2800 and 3400 RPM across a wide range of crank angle, which suggests a more effective scavenging process at this speed. However, at about 35 degrees before the transfer port closes, the pressure difference reduces to zero

and stays at zero for 20 degrees of crank angle. Although this cannot be simply interpreted as the transfer port being temporarily closed (due to the same reason stated above for 2800 RPM), it is clear that the flow rate of transferred charge may drop as a result of lack of driving force before the port is geometrically shut by the piston timing edge. It greatly impairs the process of scavenging the cylinder.

The reason for this zero $p_{cc} - p_{cyl}$ pressure difference may be attributed to two factors. The first is the continuous transferring of mass from the crankcase to the cylinder and the change of crankcase volume causes the crankcase pressure decrease. The second is the cylinder pressure increase similar to the above, plus the strong plugging pressure wave generated by the exhaust reverse cone arriving too early at the exhaust port which blocks the port, see Fig. 4.8, which eventually raises the cylinder pressure. It is clear that the early return of the plugging wave at this operating speed is responsible for such zero pressure difference across the transfer port.

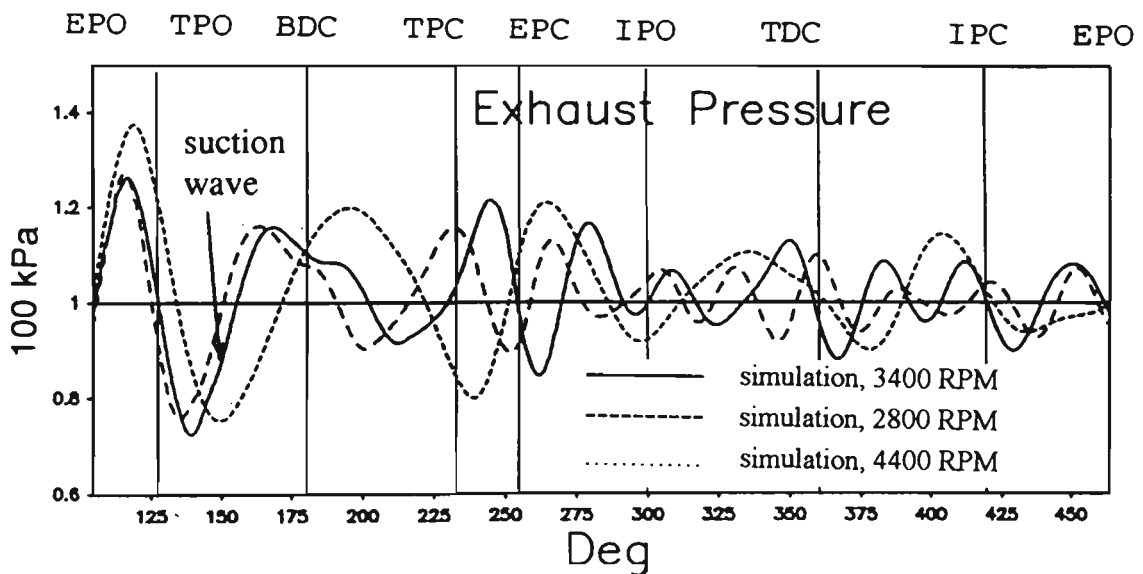


Fig. 4.8 Pressure variations at exhaust port

As the port timing of the conventional two-stroke engine is symmetric with respect to the bottom dead centre, the exhaust port is still open after the transfer port is closed. As the period between the transfer port close and the exhaust port close is as long as the cylinder blow down period, considerable fresh charge may escape to the surroundings via the

exhaust port as the piston moves towards the top dead centre. A properly phased plugging wave which is generated by the reverse cone of an expansion chamber can reduce such an escaping charge to a minimum and retain the cylinder pressure as high as possible at the trapping point (exhaust port close). A higher trapping pressure translates to a higher mass of trapped fresh mixture as long as the charge temperature at the trapping point does not vary significantly. Fig. 4.8 shows the pressure history for $L_3 = 400$ mm at the exhaust port for one engine cycle (exhaust port open - exhaust port open).

At 3400 RPM, a plugging pulse (compression wave) arrives at the exhaust port before the port closes. It acts as a closed port, raising the port pressure to about 30% above the ambient pressure and reduces the amount of fresh charge in the cylinder to be spilled out by the moving piston. As discussed in the early paragraphs, the scavenging quality at 3400 RPM is superior to that at 2800 and 4400 RPM before transfer port closes. Combining with this correctly phased plugging wave, the cylinder pressure at the commencement of compression reaches 135 kPa.

At 2800 RPM, however, the plugging pulse arrives at the exhaust port fractionally early and the blocking effect is therefore not as effective as the 3400 RPM situation. The cylinder pressure at trapping is 122 kPa.

At 4400 RPM, the wave phasing is incorrect according to the ideal wave form illustrated in Chapter 2, Fig. 2.8. It is seen that during the period between the transfer port close and the exhaust port close, there appears a negative pressure wave valley at the exhaust port which extracts the cylinder contents into the exhaust. The cylinder pressure at the trapping point is down to 108 kPa, the lowest of the three engine speeds analysed. This results in poor engine performance and high specific fuel consumption.

Finally, the calculated instantaneous mass flow rate in the exhaust and transfer system are presented in Fig. 4.9 and 4.11. The effect of unsteady gas dynamics in the pipes on the mass flow rate may be observed from these two figures. The plotted mass flows indicate, at the engine speed of 2800 RPM, for example, the arrival of the second positive pressure wave at the exhaust port takes place before the transfer port closure (TPC) thus creating

back flow through the exhaust port and transfer ports.

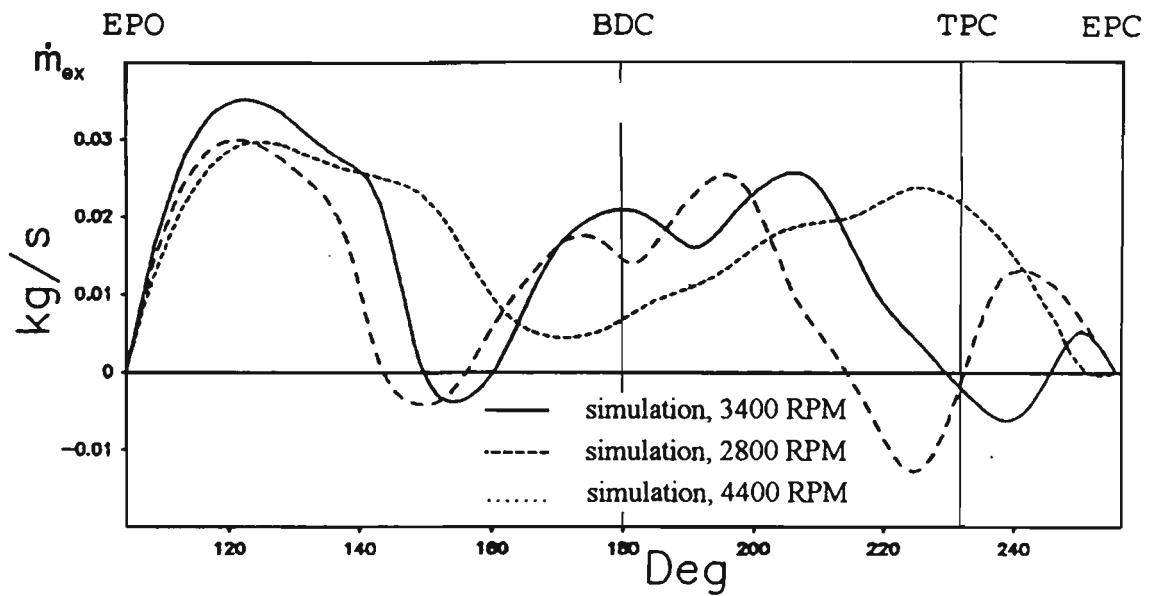


Fig. 4.9 The mass flow rate through the exhaust port

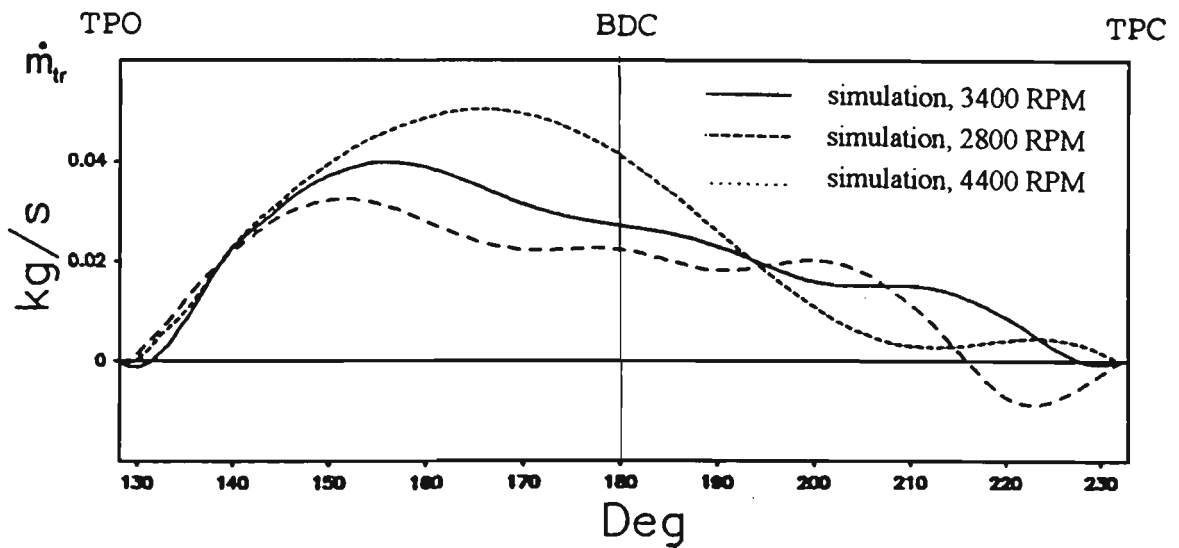


Fig. 4.10 The mass flow rate through the transfer port

4.3.2 The Analysis of Scavenging Quality

The calculated parameters for scavenging qualities, here the charging efficiencies and scavenging efficiencies, are plotted in Fig. 4.11 and 4.12, respectively. The curves show the instantaneous scavenging qualities in one engine simulation cycle. The influence of the

unsteady gas dynamic effect on two-stroke engine scavenging is demonstrated in these figures. The charging efficiency versus crank angle is displayed in Fig. 4.11. The influences of the suction wave and plugging wave are evident. The decrease of η_c after the transfer port closure at 4400 RPM is due to the delay of a plugging pulse.

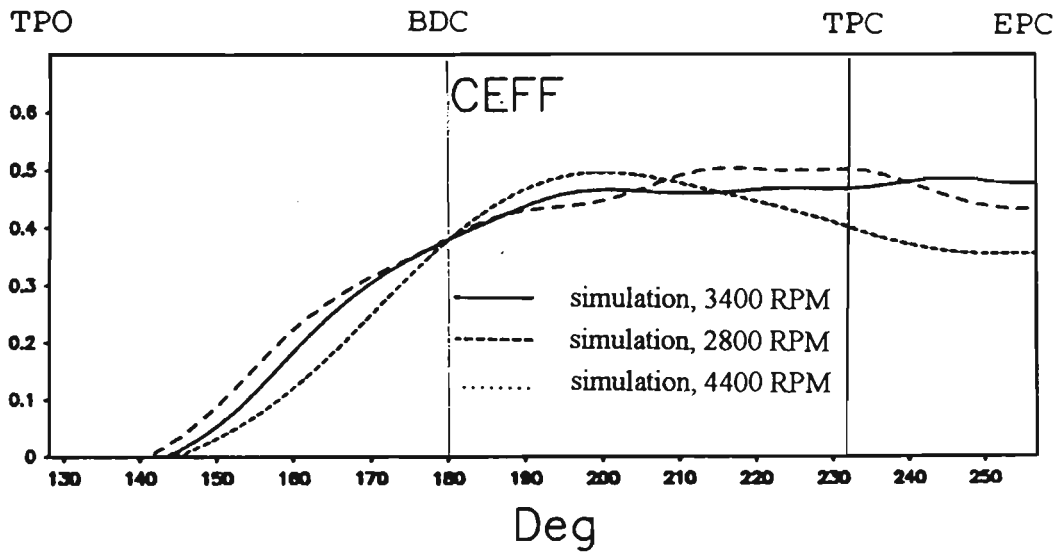


Fig. 4.11 The charging efficiency variations during the scavenging process

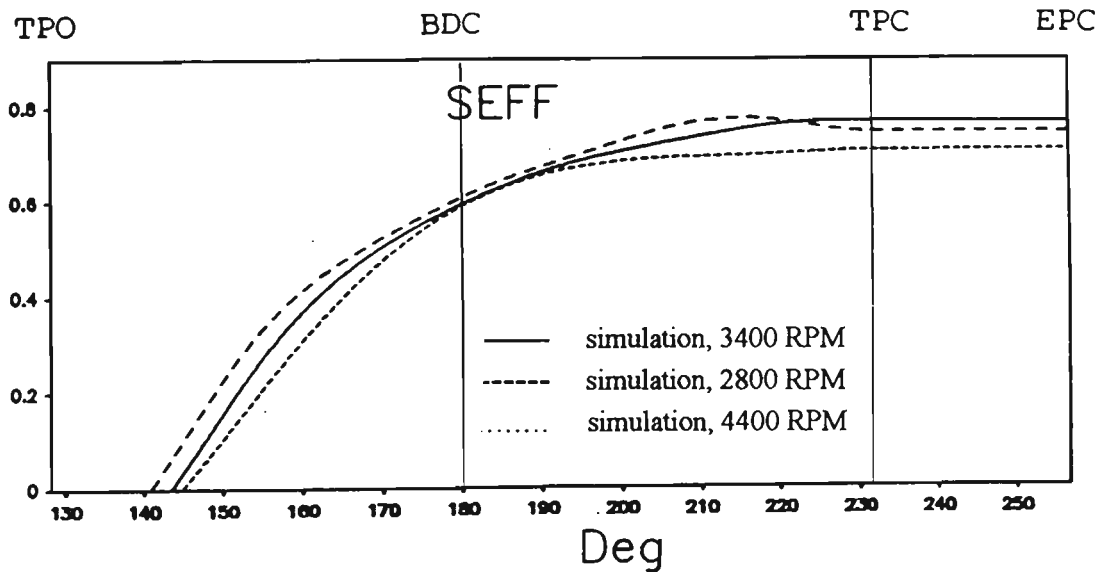
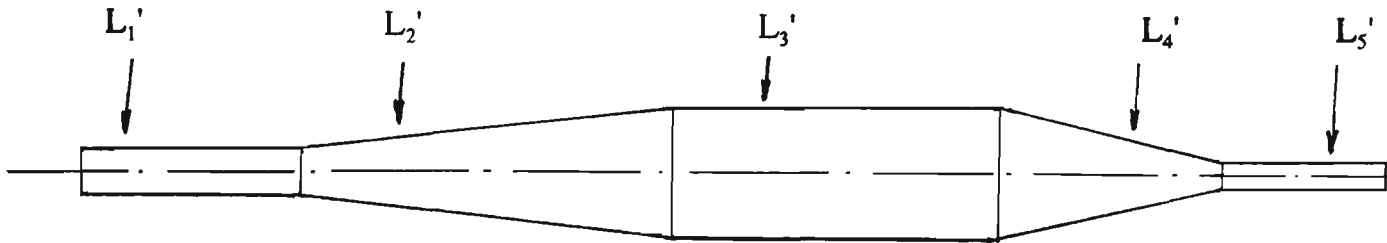


Fig. 4.12 The variations of the scavenging efficiency during the scavenging process

4.3.3 Optimisation of Exhaust Pipe for Rated Output Condition

The objective of this section is to demonstrate a further optimisation of the expansion

chamber so that the engine delivers an improved performance at the manufacturer's recommended rated continuous operating speed. The recommended rated continuous operating speed for the original engine employed in this study was 3800 RPM. To maximise its power output at this speed without disturbing the port timing and configuration, use was made of the computer program to search for the optimum dimension of each section of the pipe. The new exhaust configuration increased the engine power by 70% compared with the original box silencer exhaust. The sketch of the pipe is illustrated in Fig. 4.13:



	L_1'	L_2'	L_3'	L_4'	L_5'
Length	360	498	456	302	152
Diameter	30	30 - 99	99	99 - 20	20

Fig. 4.13. The dimension of an exhaust pipe optimised at 3800 RPM

The calculated performance data are listed below in Table 4.4:

Table 4.4

SPEED	POWER	BMEP	BSFC	λ_d	λ_s	η_s	η_c
(RPM)	(KW)	(100kPa)	(g/kWH)	(%)	(%)	(%)	(%)
3800	4.71	7.01	417	87%	131%	81%	61%

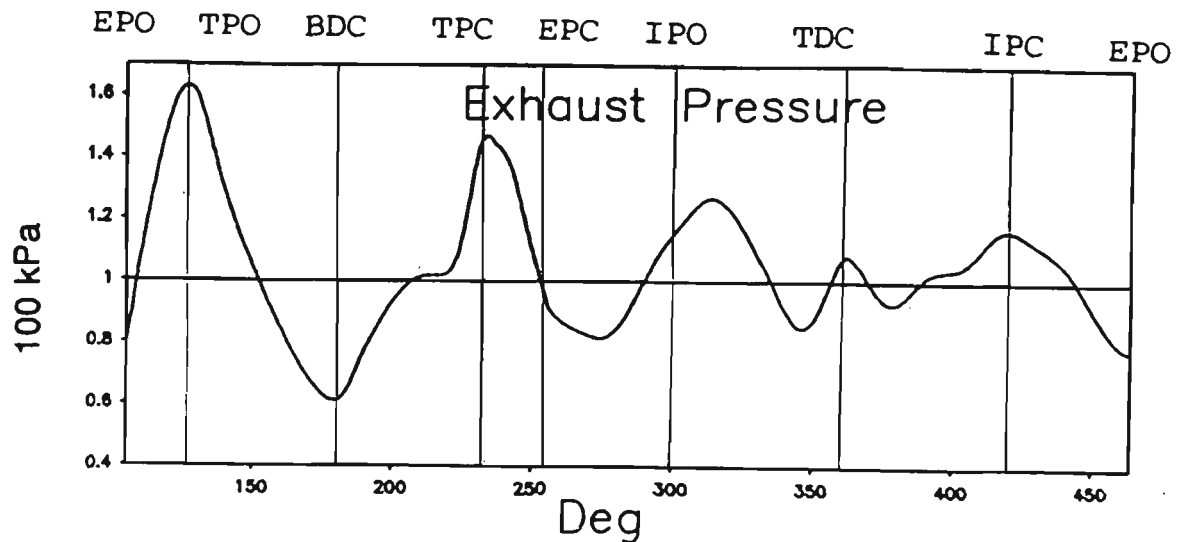


Fig. 4.14 Cyclic pressure variation at exhaust port at 3800 RPM

The exhaust pressure history at the port, as displayed in Fig. 4.14, is close to the ideal situation, see Fig. 2.8, that is, low pressure around BDC but high pressure after the transfer port closure. An alternative interpretation of Fig. 4.14 is to split the pressure trace into two superposed components, namely the "outflow" wave and the "inflow" wave. The term outflow and inflow used here are only for identifying the wave propagating directions and are irrelevant to real gas particle motion. Fig. 4.15 and 4.17 show such "outflow" and "inflow" pressure waves - the exhaust pulses, the scavenging waves and the residual waves are clearly identified.

Compared with Fig. 4.14, Fig. 4.15 and 4.16 provide more information on the wave phase and intensity, so that the level of contribution of each wave to the engine performance is recognised. It may be seen from Fig. 4.15 that after the exhaust port opens, a positive exhaust pulse is entering the pipe. This pulse, according to gas dynamic theory, propagates toward the exit of the exhaust pipe, but reflects at any change of pipe area. When it arrives at the diffusion cone, it partially reflects as an expansion wave. A compression wave will be generated when the exhaust pulse reaches the reverse cone. These two waves all travel toward the exhaust port, but arrive at the port at different times. As defined, they are "inflow" waves and are shown in Fig. 4.16.

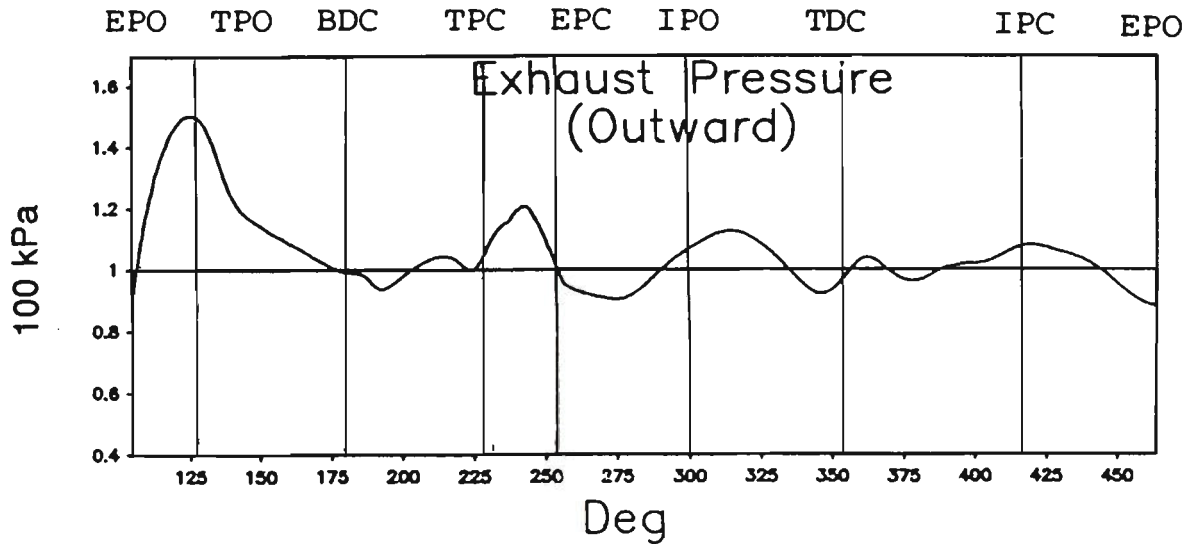


Fig. 4.15 "Outflow" pressure wave at exhaust port

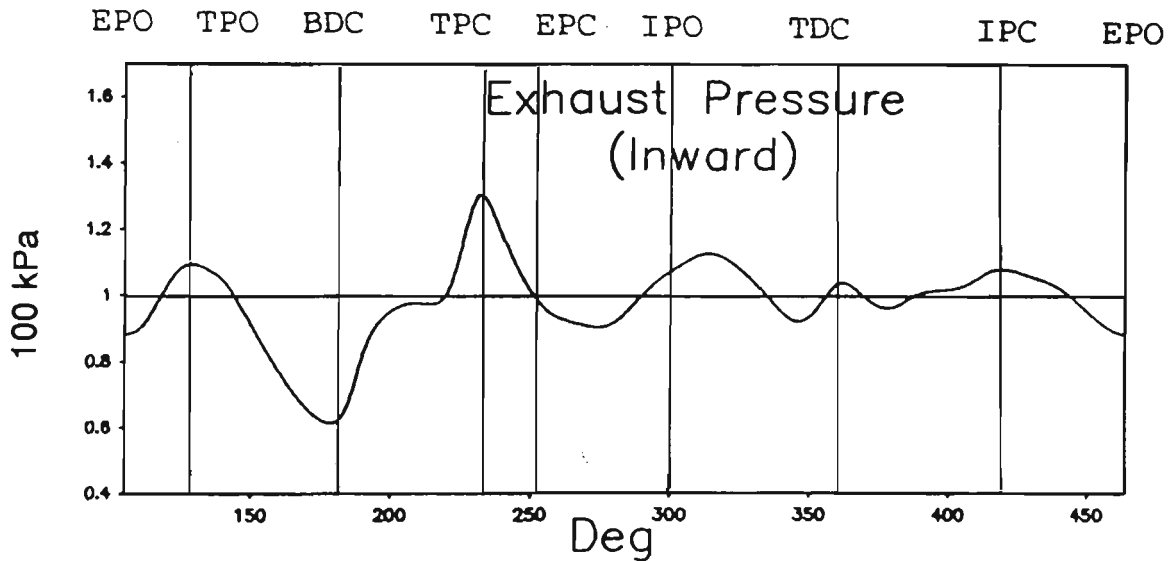


Fig. 4.16 "Inflow" pressure wave at exhaust port

Fig. 4.16 indicates that at the exhaust opening, as the exhaust pulse has just started to move out, the wave front has not yet arrived at the diffusion cone, hence no reflection occurs; the inflow wave is very weak. The small oscillation in pressure is due to the residual wave from the previous cycle. Fifty degrees crank angle after the exhaust port opens, the reflected expansion wave front arrives at the exhaust port and reduces the pressure there to considerably below atmospheric. This assists the evacuation of burnt gas from the cylinder greatly. The followed compression wave created by the reverse cone

arrives at the port shortly after the expansion wave passes. The peak of this wave lies between the transfer port closure and the exhaust port closure. The rise in pressure at the exhaust port occurring at this moment reduces the pressure difference across the port, hence reducing the loss of fresh charge through the exhaust port.

It is interesting to note that in Fig. 4.15, there appears a positive outflow pressure wave between TPC and EPC. This wave, however, is not created by the discharge of the cylinder mass, as at the opening of exhaust port. It is actually the reflection of the plugging pulse on the partially closed exhaust port. After the port closure, the characteristics of "inflow" and "outflow" waves are almost identical; this is due to the echo effect.

4.3.4 Mass Balance Examination

With the optimised exhaust pipe configuration, the mass imbalance exhibited at the pipe ends and mass ratio at the ports, as defined in section 3.11, have been calculated. The results are listed in table 4.5.

Table 4.5

ϵ_{ex}	ϵ_{tr}	ϵ_{in}	K_{in}	K_{tr}	K_{ex}
4.90 %	0.0035%	-0.11%	0.880	0.916	0.916

The mass balance data must be taken into account when evaluating the effectiveness of a simulation since the mathematical solution of engine performance characteristics are questionable unless mass balances have been performed. All the simulations presented in this study have been examined for mass balances and the data were found to be of the same order as those presented in this section. A comprehensive collection of computer simulation results are contained in Appendices C to E.

CHAPTER 5

EXPERIMENTAL APPARATUS

5.1 Introduction

A description of the test rig and engine instrumentation is given in this chapter. The two-stroke engine test rig which comprises a YAMAHA MT-110S two-stroke engine has been built for the present project in the Department of Mechanical Engineering, Victoria University of Technology. This rig, together with specially developed data acquisition hardware and software, allows systematic monitoring of engine performance data such as engine torque, speed and fuel consumption, and the dynamic pressure histories in an engine cylinder, transfer ducts and exhaust pipe under different operating conditions. The engine specifications and the details of the construction of the test rig, followed by the description of the instrumentations and data acquisition environment are presented. The experimental procedures are also outlined.

5.2 Test Engine Specification

The experimental work in this project was conducted on a YAMAHA MT-110S engine. It is a natural aspirated single cylinder schnurle type two-stroke general purpose engine, with crankcase compression, piston port timing and loop scavenging. The engine specification is shown in Table 5.1.

5.3 Construction of Experimental Apparatus and Engine Instrumentation

The test engine has undergone a number of modifications to accommodate various types of instrumentation. To enable the measurement of the pressure-crank angle history at different locations, engine performance characteristics such as torque, speed and fuel flow

rate during experiments, a dynamometer rig has been developed and illustrated in Fig 5.1. A detailed description of the instrumentation of the engine is given below.

Table 5.1 Basic Specifications of Test Engine

Manufacturer	YAMAHA Motor Co, Japan
Model	MT-110 S
Induction	Carburettor
Bore	52 mm
Stroke	50 mm
Connecting Rod Length	101 mm
Capacity	100 cc
Compression Ratio	5.8
Exhaust Port Open	104° ATDC
Transfer Port Open	128° ATDC
Inlet Port Open	62° BTDC
Exhaust System	Various

5.3.1 Fuel System

The fuel is delivered through a fuel measurement system. To determine the fuel mass flow rate, the original fuel tank was removed from the engine and placed some 0.2 meter above its original position and connected to a fuel measuring tube.

A three way valve was installed in the pipe line to ensure that during the normal operation

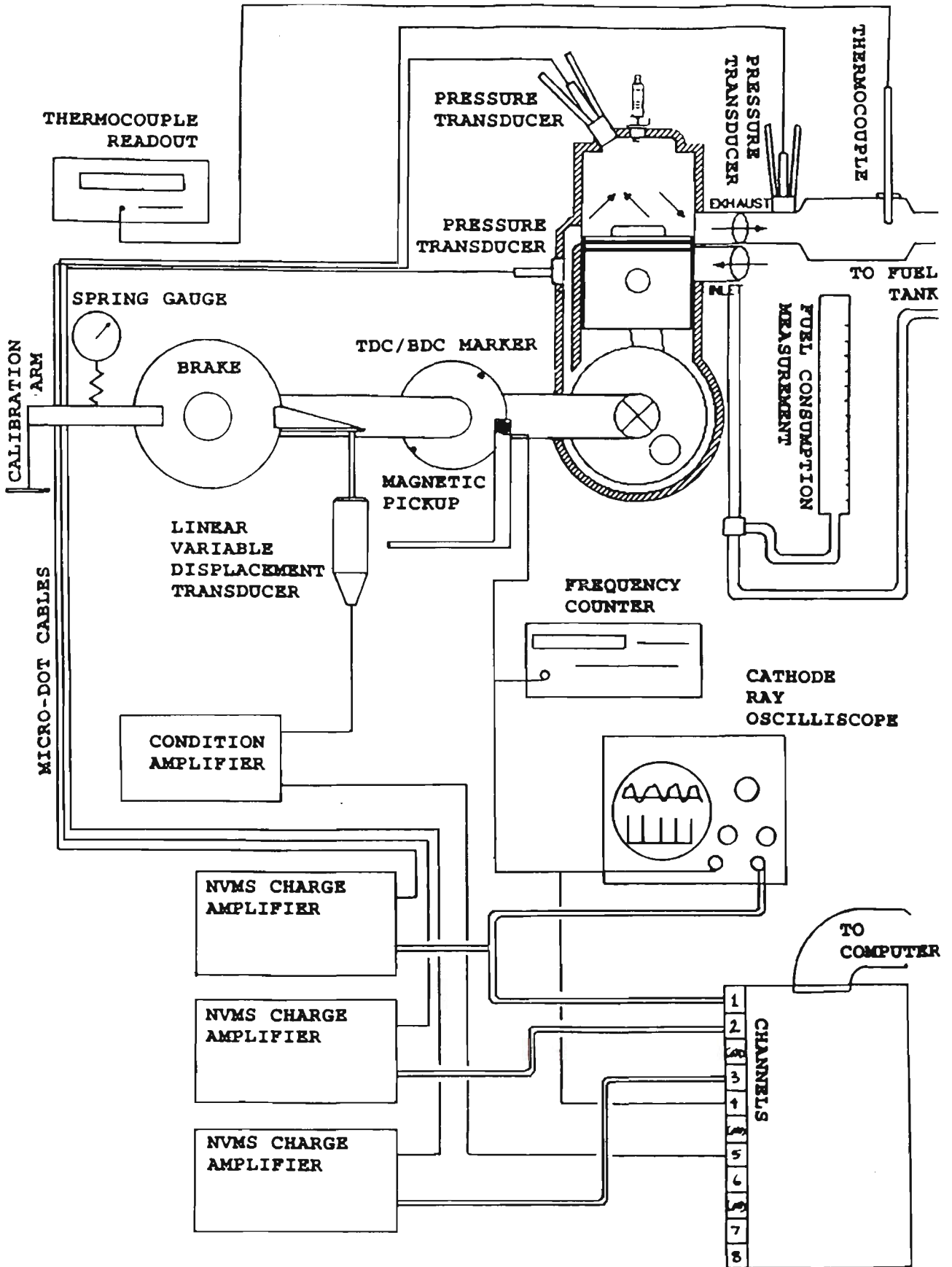


Fig. 5.1 Layout of the two-stroke engine instrumentation rig

the tank, the tube and the engine were connected to each other. When fuel measurement was required, the valve was turned off so that the supply between the fuel tank and the engine was cut and only the fuel in the measuring tube entered the engine. The time taken for the engine to consume 16 ml (measuring tube capacity) fuel was recorded by an electronic stop watch and was entered manually into the computer to determine the brake specific fuel consumption (BSFC).

A two stage throttle tuning device was designed and fitted to the original carburettor. This device ensured the accurate adjustment of the engine throttle opening. It included a coarse adjusting lever and a fine tuning screw, allowing the throttle to be tuned and locked in any desired position within its range.

5.3.2 Torque Measurement

The test engine was coupled to a TECQUIPMENT hydraulic dynamometer. The hydraulic dynamometer acts as an inefficient centrifugal pump which absorbs the mechanical energy and dissipates it as heat. The dynamometer outer casing is mounted on an anti-friction bearing so that the torque exerted on the casing is identical to the engine torque. The only torque not taken into account is the friction torque of the antifriction bearing, which is very small. The torque causes the casing to turn and the turning movement is balanced by a linear spring. The magnitude of the applied torque is thus given by:

$$M_{eng} = L \cdot (R - R_0) \quad (5.1)$$

where R and R_0 are displacement of the spring with dynamometer in operation and with dynamometer free from load respectively; L is the length of the torque arm, which is measured from the centre of the dynamometer shaft to the spring, as depicted in Fig. 5.2. As the rotation of the lever was very small, it was assumed that the torque arm L was constant.

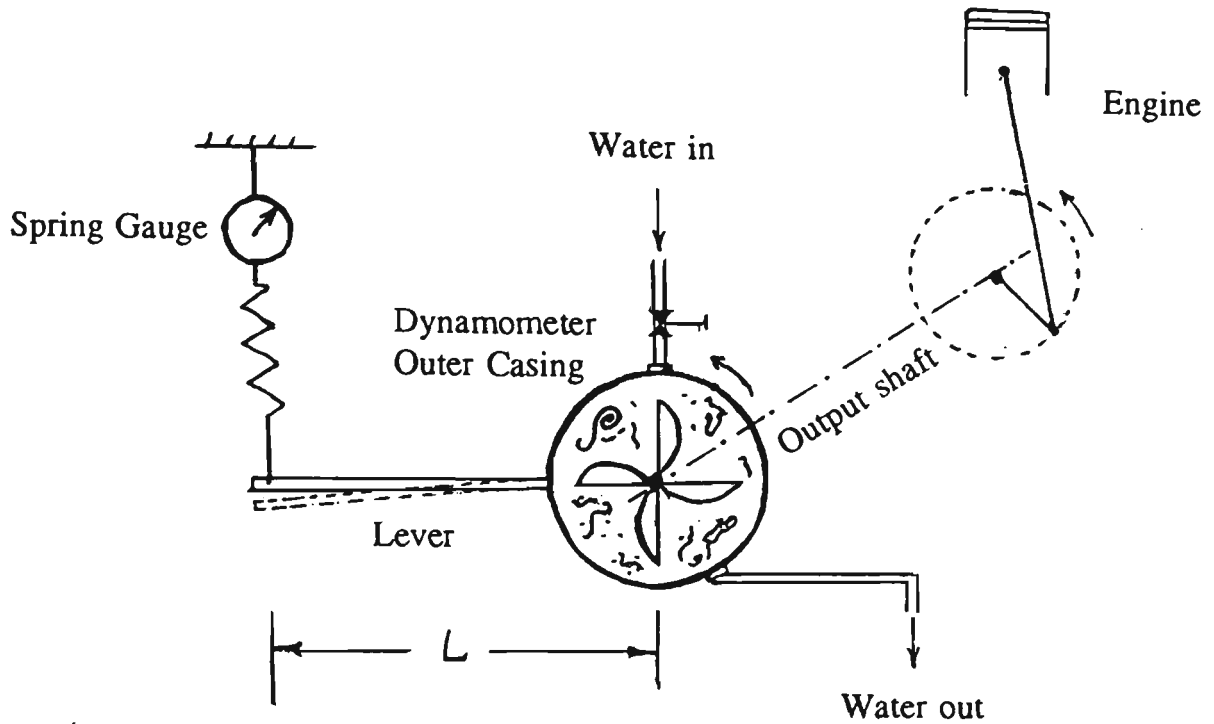


Fig. 5.2 Torque measuring device

However, due to the unavoidable vibration of the original torque measuring instrument (a spring scale) during the engine operation, accurate torque measurement was difficult. Therefore a new measuring device was developed, which used an electronic device to measure engine torque, as shown in Fig. 5.3. In this device, a dummy torque arm was attached to the outer casing of the dynamometer. The arm was 0.5 meter in length measured from the dynamometer centre. The purpose of attaching this dummy lever was to obtain the relation between the dynamometer outer casing turning movement and the torque applied to it.

To determine this, weights were gradually loaded onto the far end of the dummy torque lever to simulate the reaction torque produced by the engine. This caused a turning movement of the dynamometer outer casing as well. On the right hand side of the dynamometer, a short beam was attached to the dynamometer outer casing. The turning movement of this casing caused by the application of torque (either calibrating torque or engine torque) was then detected by a Linear Variable Differential Transducer (LVDT). A relationship between the torque applied by the weights during calibration and the LVDT output was found by calibration. The results are presented in Table 5.2 and Fig. 5.4.

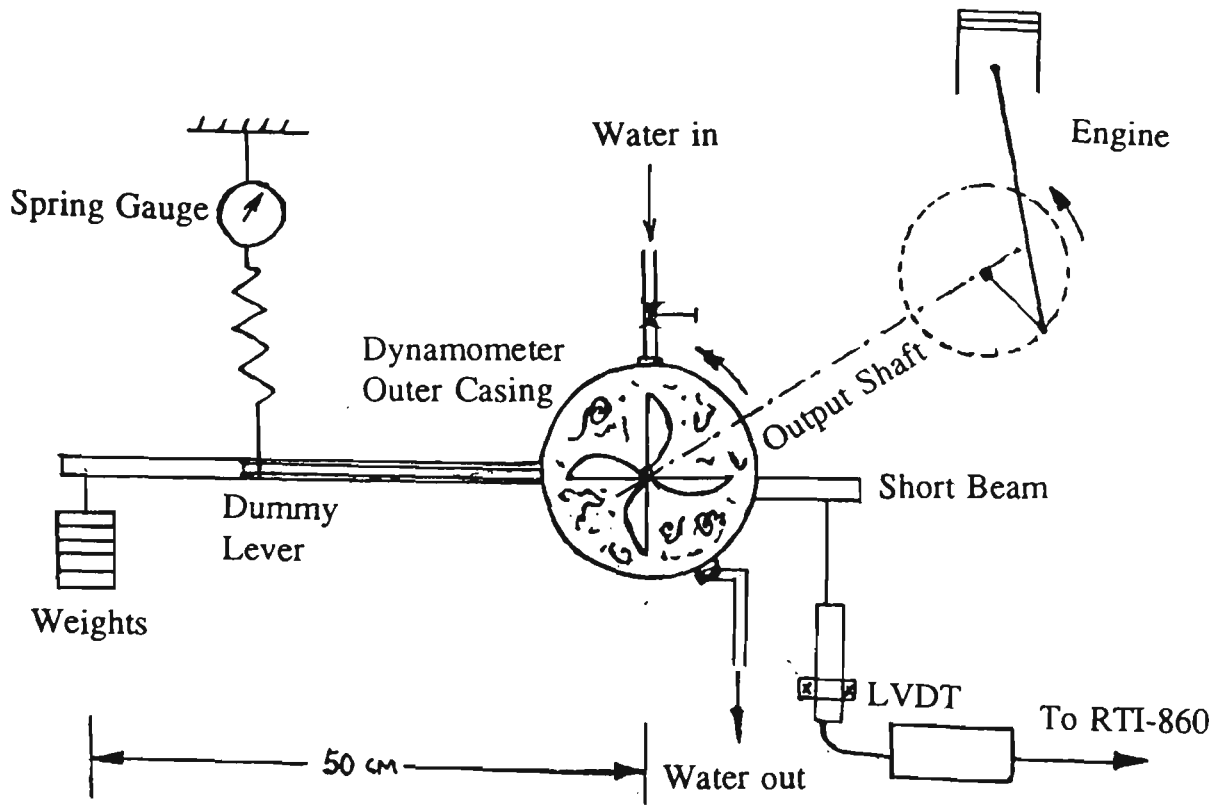


Fig. 5.3 Modified torque measuring device

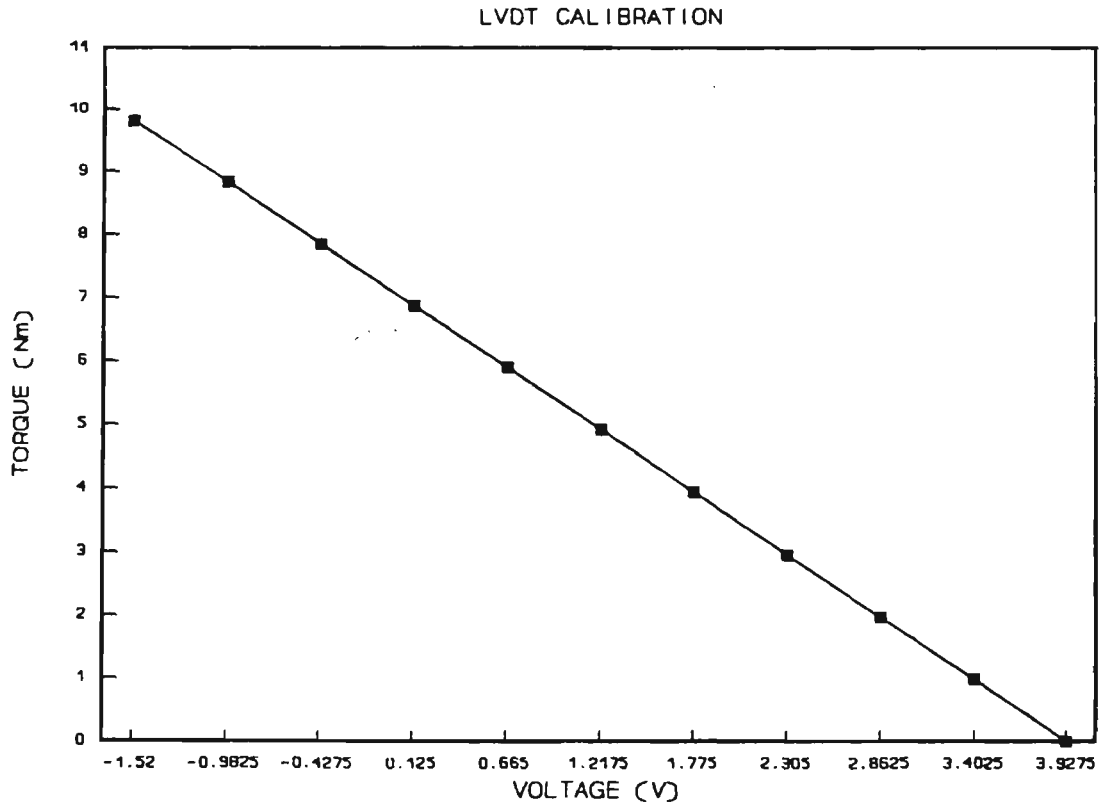


Fig. 5.4 Calibration of torque measuring device

Table 5.2 Calibration of torque measurement device

+ Weights(kg)	Voltage	- Weights(kg)	Voltage
lever+hook	3.99	2.00	-1.56
0.20	3.48	1.80	-1.02
0.40	2.94	1.60	-0.48
0.60	2.38	1.40	0.07
0.80	1.82	1.20	0.60
1.00	1.25	1.00	1.15
1.20	0.71	0.80	1.71
1.40	0.17	0.60	2.24
1.60	-0.39	0.40	2.79
1.80	-0.93	0.20	3.34
2.00	-1.50	lever+hook	3.86

As a result, the following equation relating torque M_{eng} and LVDT output was obtained:

$$M_{eng} = -1.79 \cdot V + 7.08 \quad (5.2)$$

After calibration, the weights and the dummy lever are removed and the angular movement of the dynamometer outer casing is restored. During engine operation, as mentioned previously, the engine exerts a torque on the dynamometer outer casing and causes it to swing. Since the relation of the applied torque versus dynamometer outer casing angular displacement (voltage from LVDT) has been determined, it was a simple matter to work out the engine torque through the output voltage of the LVDT.

The slope of the above equation was of primary importance. To compensate for LVDT

output drift from time to time, the LVDT output voltage was measured as a reference, or off-set voltage V_0 , before starting the engine. The equation for calculation of engine torque was thus modified to:

$$M_{eng} = C (V - V_0) \quad (5.3)$$

where M_{eng} - engine torque (Nm)

C - calibration constant, $C = -1.79$ Nm/V

V - LVDT output when the engine is running (V)

V_0 - LVDT output before the engine is started (V)

The above equation was programmed into the engine instrumentation software.

During engine testing, 50,000 LVDT samples were collected and averaged over each second. The averaged output, V , was fed into the equation (5.3) to work out engine torque M_{eng} . This torque value was displayed on-screen.

5.3.3 Dead Centre Marker and Engine Speed Measurement

To determine the phase of the unsteady pressure variations, determination of the crank angle was necessary. In the present project, this task was simplified by recording both top dead centre and bottom dead centre. The degrees of crank angle between dead centres were marked proportionally during post data processing. The construction of the dead centre markers is described below.

A round disk was made with two small holes drilled on its edge. The holes were 180° apart and two small bolts were attached to the holes. The disk itself was fixed tightly onto the engine output shaft by means of three grub screws. A digital magnetic pick-up was mounted on an aluminium bracket and was located close to the disk. The gap between the pick-up and the bolts was adjustable and was set at 0.50 mm for the optimal signal quality. With the engine piston set at either top dead centre or bottom dead centre, the position of the round disk was adjusted so that the location of the ferrous bolt agreed with the

magnetic pick up. The magnetic pick-up was excited by a 12 Volts DC power supply, see Fig. 5.5.

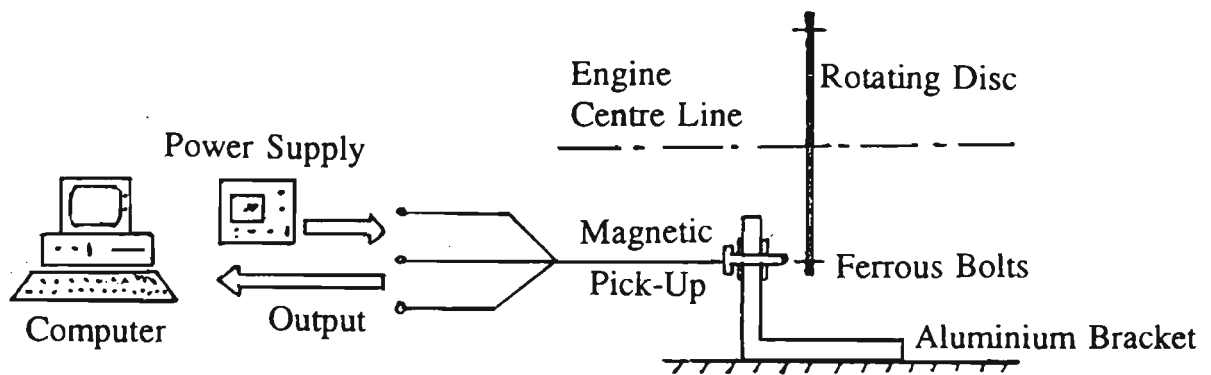


Fig. 5.5 Schematic diagram of dead centre marker

During the engine operation, the disk was rotated. As the ferrous bolt on the disk passed by the magnetic pick-up, it caused a magnetic flux change which resulted in an output signal which momentarily passed through zero as the bolt axis lined up with the transducer. This signified that the piston was instantaneously at either at TDC or BDC. By reference to the cylinder pressure history, the top dead centre was identified. The port timing on the pressure-crank angle record was then marked proportionally.

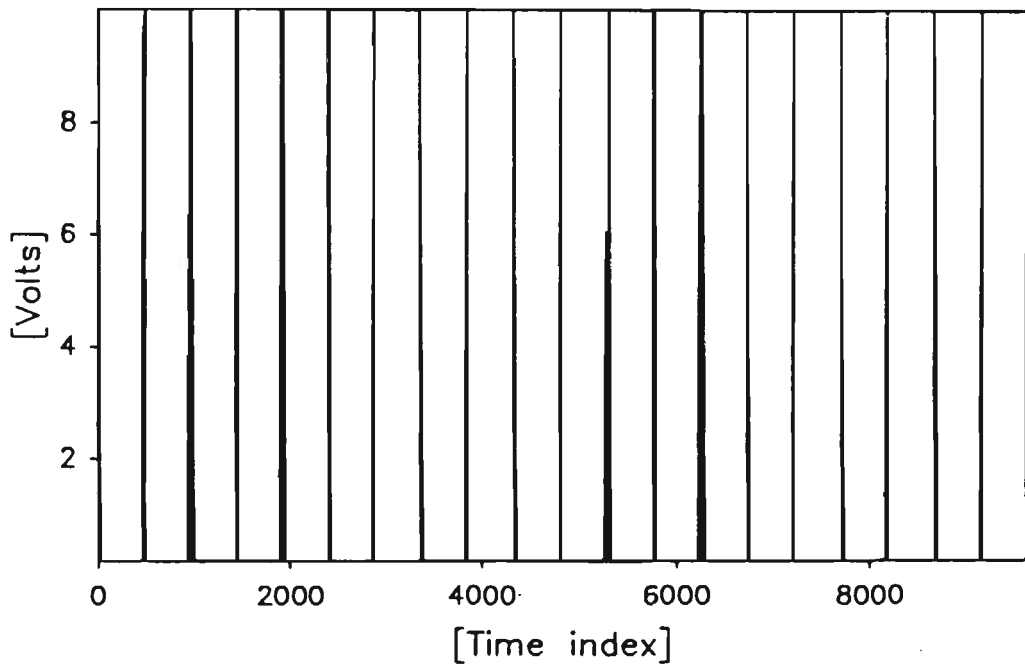
To determine the accuracy of the alignment between the sampled TDC and the true geometric TDC, a laser displacement transducer was employed to accurately determine the piston position. The transducer was held by a magnetic clamp and placed just above the spark plug hole to sense the distance between the sensor and the piston crown (the spark plug was removed). Turning the engine by pulling the recoil starter gently, the signal produced by the laser displacement transducer and the magnetic pick-up were recorded simultaneously. The results from the two transducers were compared and the positions of the peaks from the magnetic pick-up were found to coincide with the minimum distance available from the laser displacement transducer. It was important to empty the fuel supply line so that the laser lens was not stained by fuel particles.

To monitor the engine speed on line, the pulse signals from the magnetic pick-up were

continuously fed to a calibrated Hewlett Packard frequency counter. As two pulses were generated per revolution, the engine speed was found as:

$$\text{Engine Speed} = 30 * \text{Frequency (RPM)}$$

The instantaneous engine speed can be much more accurately determined after an analysis of the dead centre marker records. Since the sampling rate and the number of sampling elements were predefined, it was a simple matter to work out the engine speed by counting the pulses and dividing by the time elapsed. Fig. 5.6 shows an example of a dead centre marker record.



Trigger positions are:

0	0	10	4921
1	491	11	5410
2	986	12	5903
3	1476	13	6393
4	1971	14	6886
5	2461	15	7376
6	2955	16	7870
7	3444	17	8360
8	3938	18	8854
9	4427		

RPM (trigger processing): 3049.47

RPM (frequency counter): 3027

Sampling frequency: 50,000 Hz

Sampling element: 10,000

Fig. 5.6 A dead centre marker record

5.3.4 Pressure Transducer Installation and Pressure Trace Measurement

Three new PCB piezoelectric pressure transducers were employed in the project to record the dynamic pressure history. The transducers were located in cylinder head, transfer port and exhaust port, respectively. The transducers for cylinder and exhaust port were water-cooled.

5.3.5 Measurement of Exhaust Temperature

Two calibrated mineral insulated thermocouples of type K were installed in the exhaust system, one at the header pipe and the other at the expansion chamber end. The exhaust temperatures at both locations were monitored digitally for the duration of the test. The gas temperature in the pipe was used by the program as a pipe reference temperature to calculate the reference sound velocity which is necessary for the determination of the Riemann variables along the grid nodes in the exhaust pipe. To ensure that the situation in the test cell was close to that of the theoretical model (adiabatic), the exhaust pipe was insulated. The temperature from the two different locations along the pipe was averaged as the pipe reference temperature and input to the program to calculate the reference sound velocity in the exhaust pipe. During experiments, the gas temperature at the header pipe was limited to 600 °C for safety reason.

5.4 Computerised Data Acquisition System

To rapidly capture the analogue and digital data from the test two-stroke engine, a computer-controlled 16 channel fast data acquisition system has been developed. It consists of an IBM compatible desk-top computer, an RTI-860 data acquisition board, a screw terminal and appropriate wiring. This system was primarily developed to be used for the investigation of dynamic pressure variations in the engine cylinder and pipes. The parameters to be measured include instantaneous cylinder pressure, exhaust and transfer pressures, torque, fuel consumption, exhaust temperature, engine speed, and top dead

centre and bottom dead centre.

5.4.1 Description of Hardware

The RTI-860 is a real-time interface I/O board available from Analog Devices. It is compatible with the IBM PC AT or equivalent personal computers and can be directly plugged into one of the long expansion slots in those machines. It is a high-speed simultaneous data acquisition board that can perform 12 or 8 bit analog-to-digital conversions for up to 16 single-ended analog input channels. The signals it required were those pre-conditioned analog signals within either a ± 10 V or ± 5 V range. The board has the capability to acquire data from a single channel or to scan from multiple channels.

The data acquired can be stored in either the 256 Kilobytes on-board memory or system memory. It also has the ability to simultaneously sample data from a group of four analog input channels (channels 0 - 3, 4 - 7, 8 - 11, or 12 - 15). In such cases, four sample-and-hold amplifiers simultaneously sample and then hold the data from the four input channels while the analog-to-digital converter sequentially digitises them.

The amplitude of the analogue signal is digitised by an analogue to digital converter (ADC). The converter has 12-bit resolution (a maximum of 4096 counts), providing a resolution of 4.88 mV in the ± 10 V range, 2.44 mV when in the ± 5 V range. The ADC can be jumpered for an 8-bit resolution mode (up to 256 counts). The measurement range of ± 10 V or ± 5 V analog signals is also jumper-selectable. The 12 bit resolution and ± 5 V range was used for the project.

All analog inputs are accessed through the STB-GP screw termination panel. The STB-GP Panel contains a series of numbered screw terminations for direct connection to the various input signals. The unused screw terminations were all grounded to avoid possible disturbances. All the signals are brought over to the board through the 50-pin ribbon cable.

5.4.2 Description of Software

A computer program was written to acquire, process and save the data gathered from the instruments monitoring the engine test rig. It is a menu driven program which collects, graphs and saves the data to file for post processing. Prior to the engine test, the user may enter:

- 1) RTI-860 set up details, including board measuring range, sample size and sampling frequency,
- 2) test engine specifications,
- 3) channel sensitivities,
- 4) channel offsets.

The acquisition of pressures (for pressure at cylinder, transfer port and exhaust port, respectively) and magnetic pick up (for dead centre position) signals in four channels are acquired simultaneously at a rate of 50,000 samples per second and stored in the on board memory, before being transferred to the computer memory and saved to temporary files. The torque signal from the LVDT is collected continuously and averaged over a period of one second and printed to the screen. This value is then saved to a variable in the program when the pressure sampling mode is enacted. All analog signals from the four channels are simultaneously sampled, held and then fed to the computer at a speed the computer can handle. The program sorts the information from the four channels into four temporary files, each being specific data from each channel. These files are then automatically accessed, and the information graphed on the screen. When the SAVE command is initiated, the signals from four channels are saved under their respective files name. Then the program finds the exact positions of TDC and BDC. These values, together with the value of engine brake torque at the moment of sampling, are saved into an ASCII file to assist in analysis of the dynamic pressure trace.

5.5 Engine Experimental Procedure

To successfully operate the engine, the test rig is started after checking that all the instrumentation, data communication and water supply are functioning properly. It is necessary to wait until a stable operating condition is reached. The sequences are as follows:

- 1) Switch on power and water supply.
- 2) Enter or verify software default parameters for data acquisition.
- 3) Set charge amplifiers.
- 4) Check the fuel system. Expel air.
- 5) Measure the static LVDT output voltage (offset). This voltage is regarded as the datum voltage for torque measurement.
- 6) Record ambient temperature and pressure.
- 7) Set the length of exhaust pipe.
- 8) Start the engine.
- 9) Open the throttle and the dynamometer water valve gradually, letting the engine warm up.
- 10) Set the throttle at test position. Wait until stable conditions are achieved.
- 11) Vary the engine load by adjusting the amount of water entering the dynamometer.
- 12) Measure the fuel consumption.

- 13) Record engine torque and speed.
- 14) Check the dynamic pressure signals displayed on the CRO to ensure all pressure transducers are working properly. Capture all dynamic signals.
- 15) Repeat step 11-14 to get the speed characteristics.
- 16) Change the length of the exhaust pipe and repeat steps 11-15.
- 17) Stop the engine.

CHAPTER SIX

EXPERIMENTAL RESULTS AND DISCUSSION

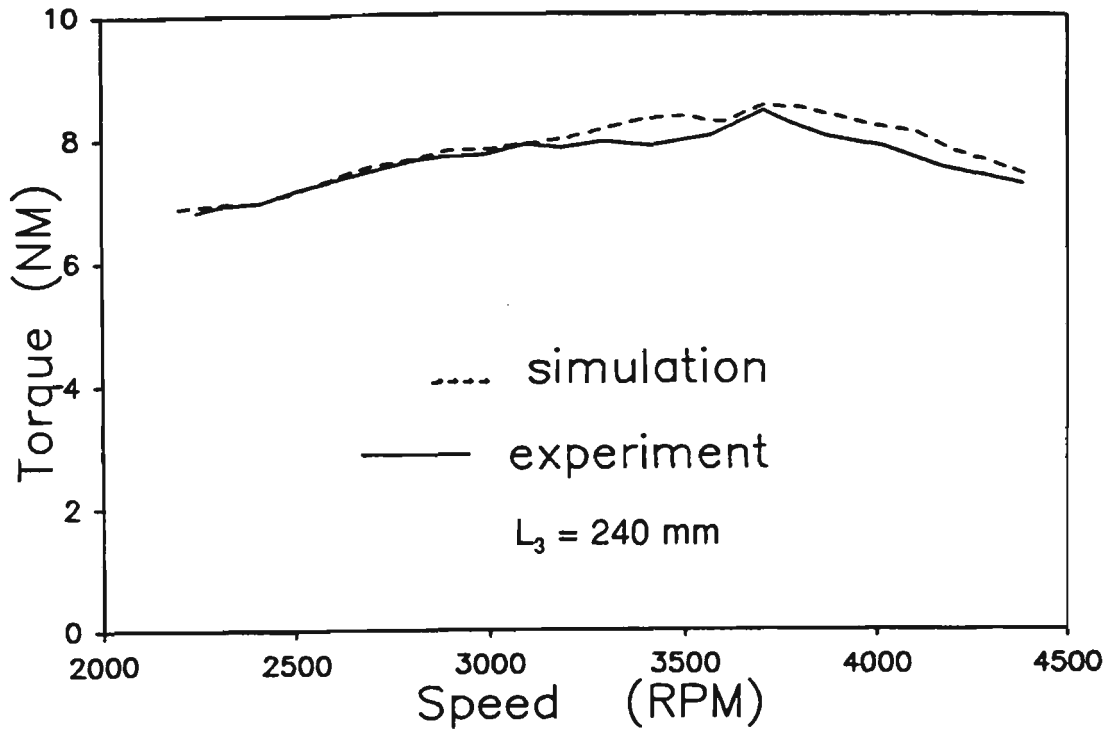
6.1 Introduction

After the construction of the dynamometer rig and the exhaust pipe, the engine testing was carried out as described in section 5.4. A range of tests was performed to verify the computer model. Each point on the performance characteristics, including pressure traces, required approximately 250 kilobytes of computer memory. Data shown here are typical examples obtained during the experiments and are presented for illustrative purposes. Results for five lengths of the middle parallel section of the exhaust pipe L_3 are shown: 240, 330, 400, 480 and 550 mm. Experimental results are compared with numerical model predictions displayed in the figure with a dashed line for comparison. Wide open throttle (WOT) performance characteristics were compared for nominated lengths L_3 . Cylinder and port pressure traces for various speeds are also compared.

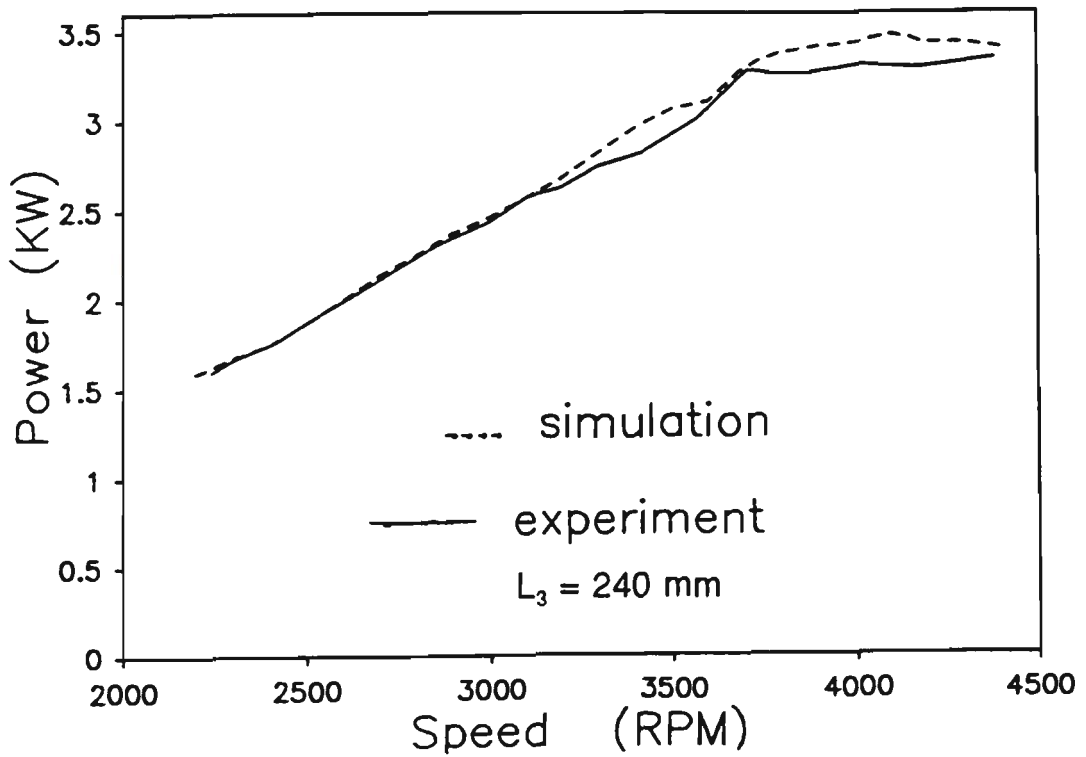
The measured engine torque and power curves with the middle parallel section of the exhaust pipe L_3 settings at 240, 330, 400, 480 and 550 mm are presented in Fig. 6.1-5, respectively. The calculated engine performances are also displayed with a dashed line for comparison.

6.2 Measured and Predicted Performance Characteristics

The measured torque curve for the test engine with its original box silencer was shown in Fig. 4.3 (the solid line curve located on the bottom of that graph). Its maximum value was 7 Nm. From Fig. 6.1-5, it is clear that over nearly the whole speed range studied, the engine performance with the designed exhaust pipe surpassed that with the original box silencer. The peak performance shifted towards lower RPM as the pipe length was increased, in accordance with the mathematical predictions. The agreement between the

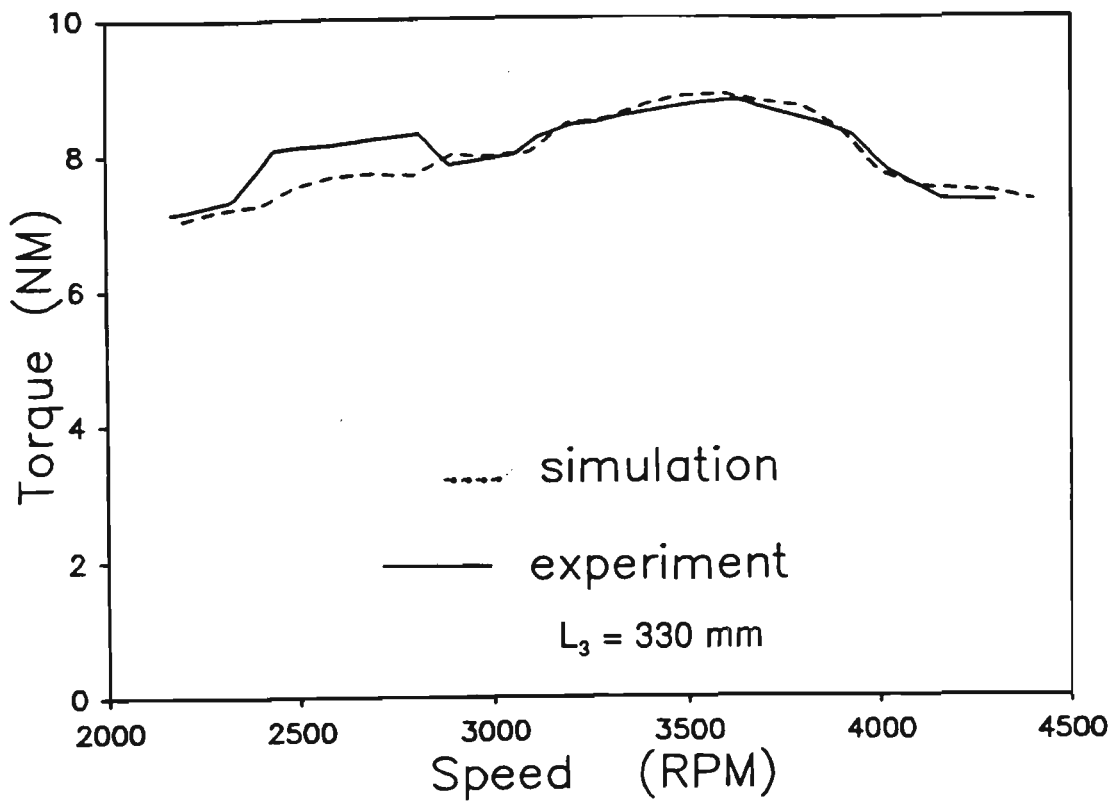


(a) Torque curve

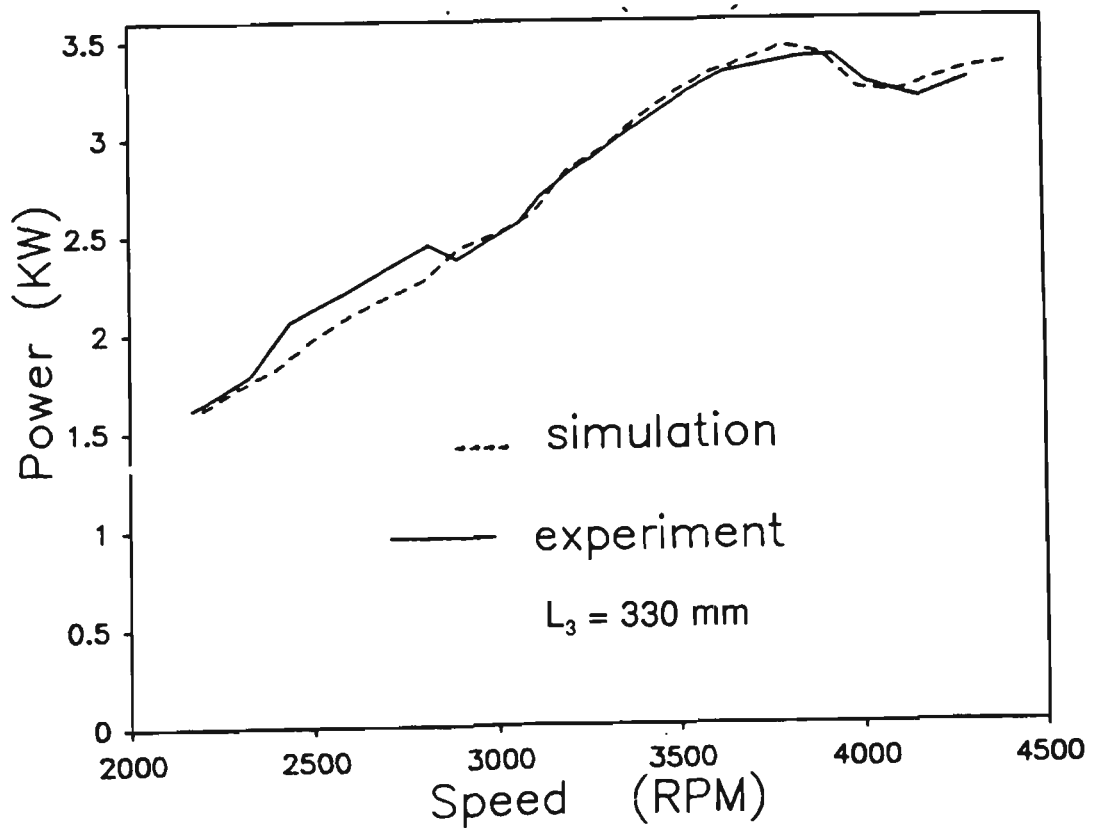


(b) Power curve

Fig. 6.1 Performance characteristics for $L_3 = 240$ mm

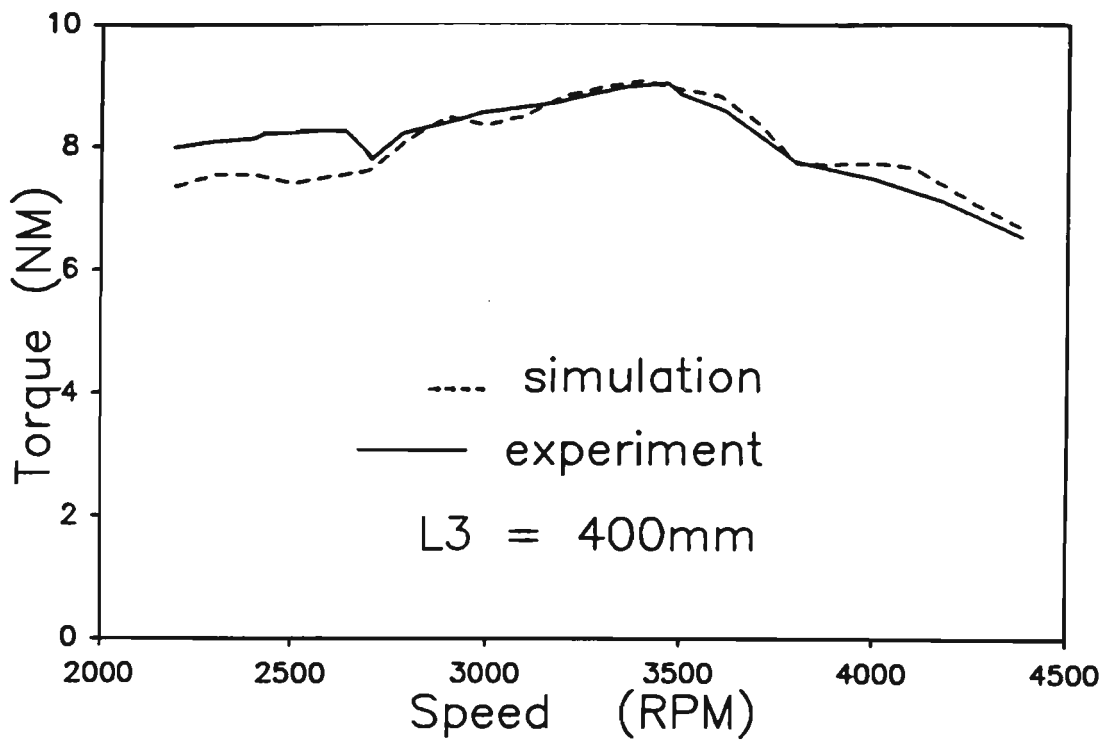


(a) Torque curve

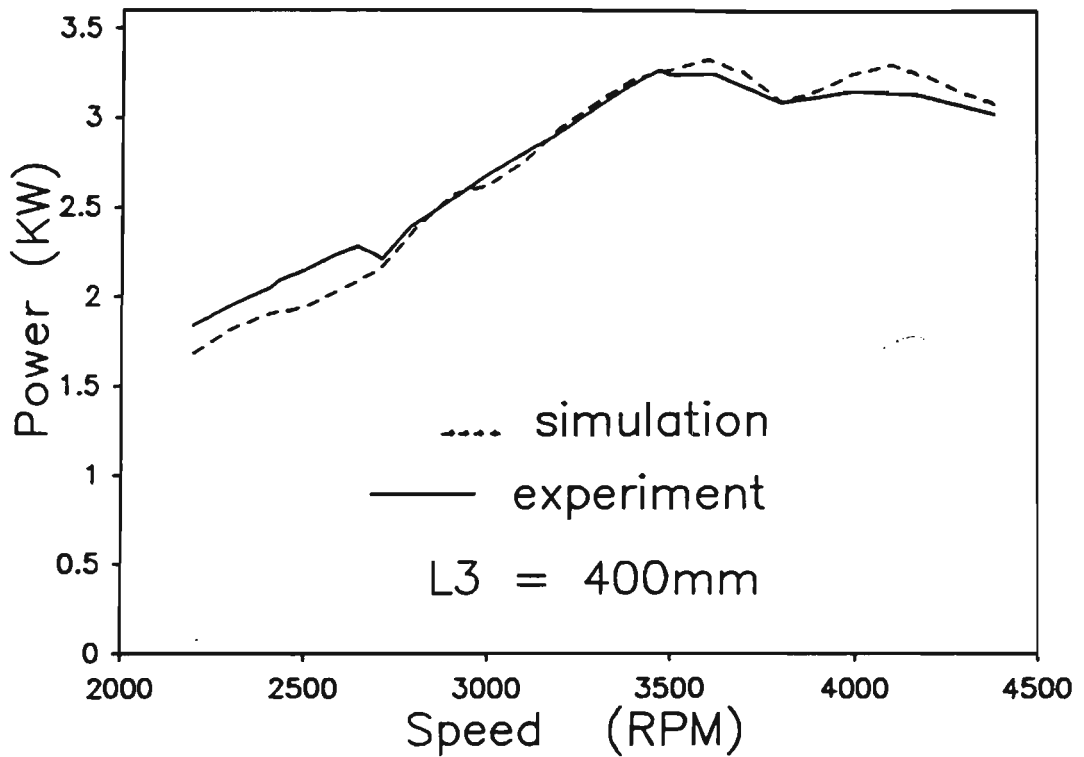


(b) Power curve

Fig. 6.2 Performance characteristics for $L_3 = 330$ mm

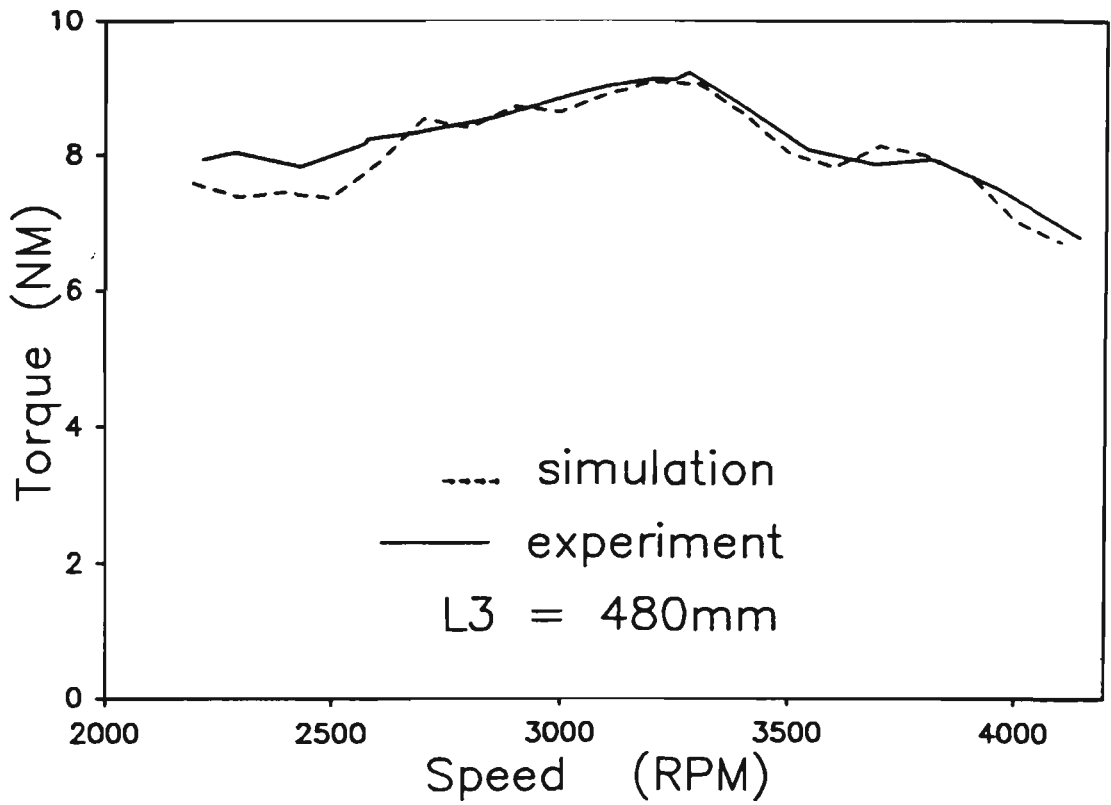


(a) Torque curve

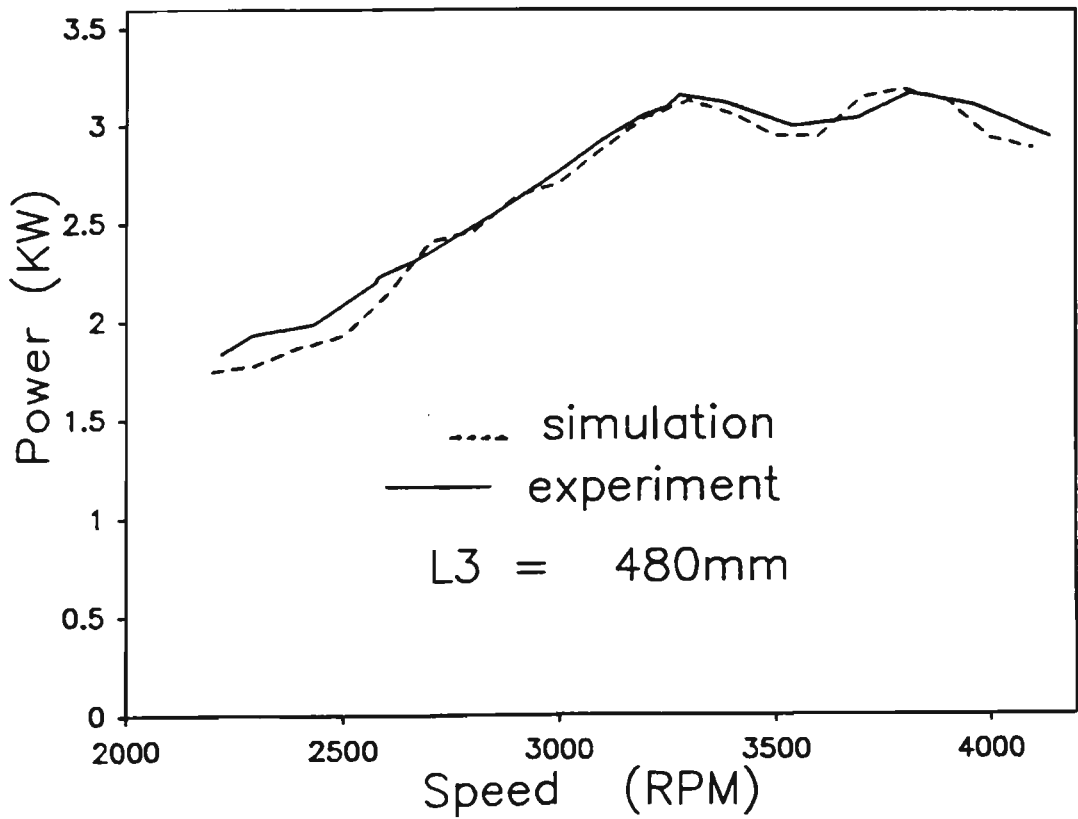


(b) Power curve

Fig. 6.3 Performance characteristics for $L_3 = 400\text{ mm}$

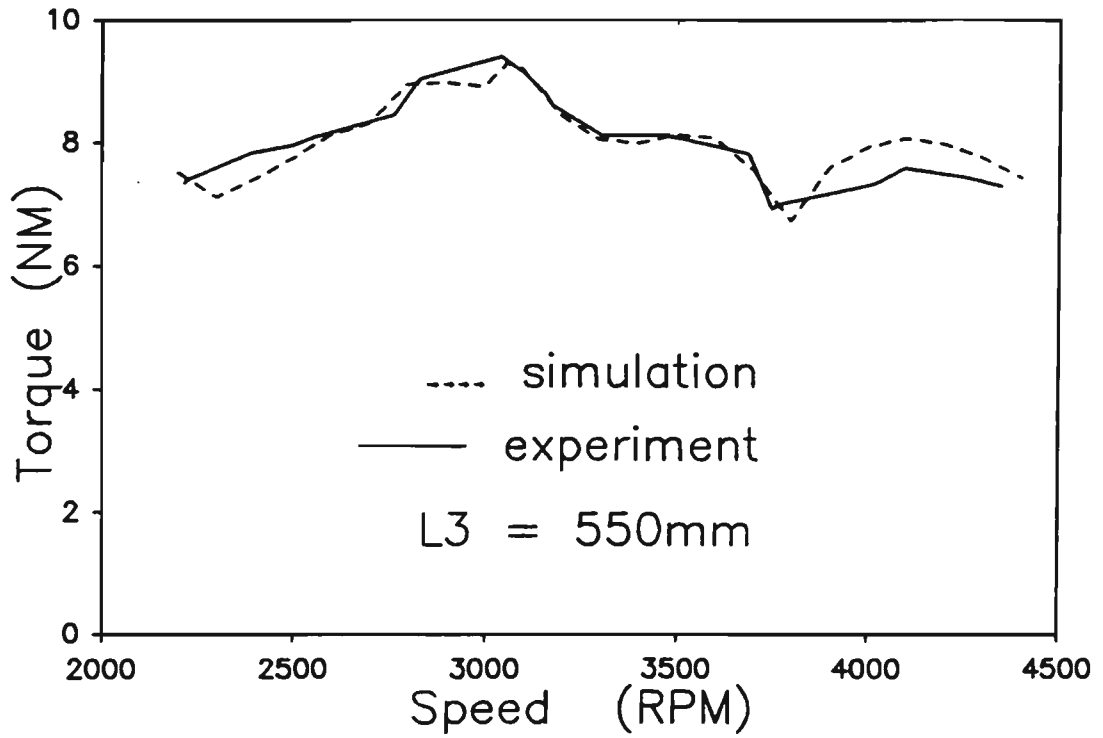


(a) Torque curve

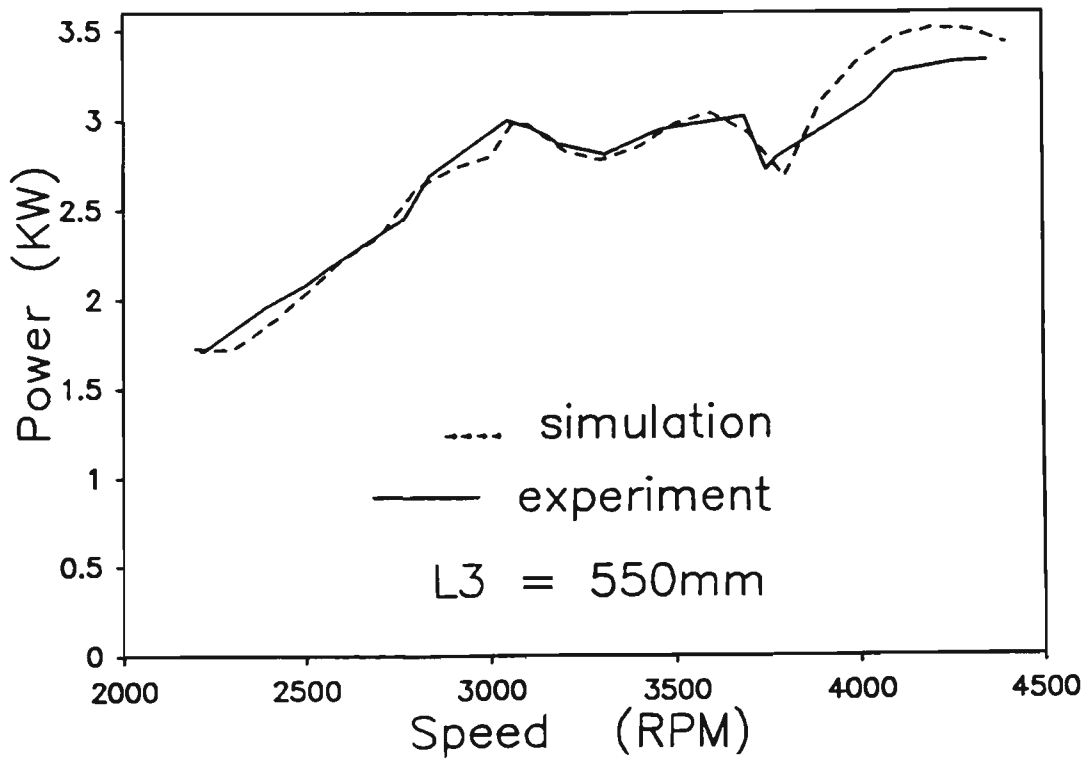


(b) Power curve

Fig. 6.4 Performance characteristics for $L_3 = 480\text{ mm}$



(a) Torque curve



(b) Power curve

Fig. 6.5 Performance characteristics for $L_3 = 550$ mm

measurements and calculations was good, particularly at the medium and higher speeds. At lower speeds, the agreement deteriorated slightly, however the maximum discrepancy was still below 10%.

Apart from the pipe flow model, the prediction of engine performance characteristics is very dependent on how the combustion is modelled. The pipe flow model describes how the engine breathes, but it is the combustion model which describes how the fresh mixture trapped in the cylinder is burnt and the power delivered. In the current study, the combustion model was simplified as a heat release model. The value of the model parameters (polytropic index, combustion efficiency, trapped air-fuel ratio etc.) were those suggested by Blair *et al* [49][56]. These parameters are assumed constant for all speeds in the calculations. In practical cases, these parameters may vary slightly with engine speed and load change. For an accurate simulation, such parameters should be determined experimentally and input to the program. This may include the accurate analysis of the cylinder pressure trace, and the measurement of the trapping efficiency and BSFC.

The general agreement between the measurements and calculations achieved in this study suggests that the constant value combustion parameters used in this study are adequate.

6.3 Measured and Predicted Pressure Traces

The dynamic pressure histories in the cylinder, transfer port and exhaust port have been successfully acquired. As the amount of data collected was large (over 250 kilobytes each sampling) and take considerable computer time to sort and display while the engine is running, they were only taken for significant events. The overall engine performance characteristics were measured prior to recording the dynamic pressure signals. The engine speed which corresponds to good or poor performance was determined and the pressure acquisition routine was then executed. Figures 6.6 - 6.12 show typical pressure traces. Data were taken at:

- 1) 2900, 3435 and 3741 RPM for $L_3 = 330$ mm;

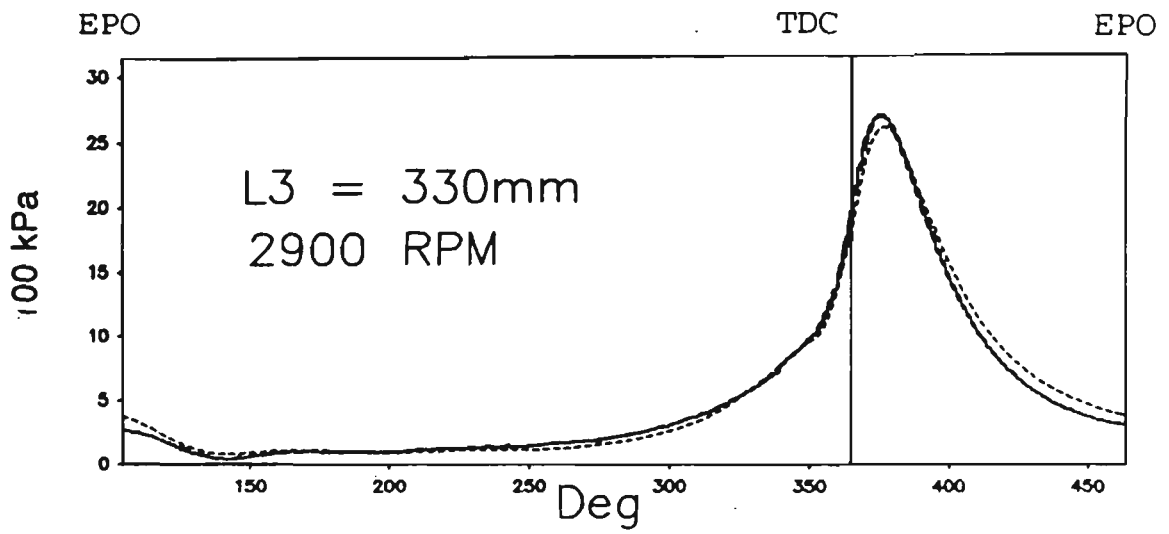
- 2) 3328 RPM for $L_3 = 400$ mm;
- 3) 2550 and 3250 RPM for $L_3 = 480$ mm
- 4) 3060 RPM for $L_3 = 550$ mm.

The calculated pressure variations versus crank angle in cylinder, transfer port and exhaust port are also presented in Fig. 6.6-12 using a dashed line for comparison. The agreement between the measured and calculated pressure traces was good.

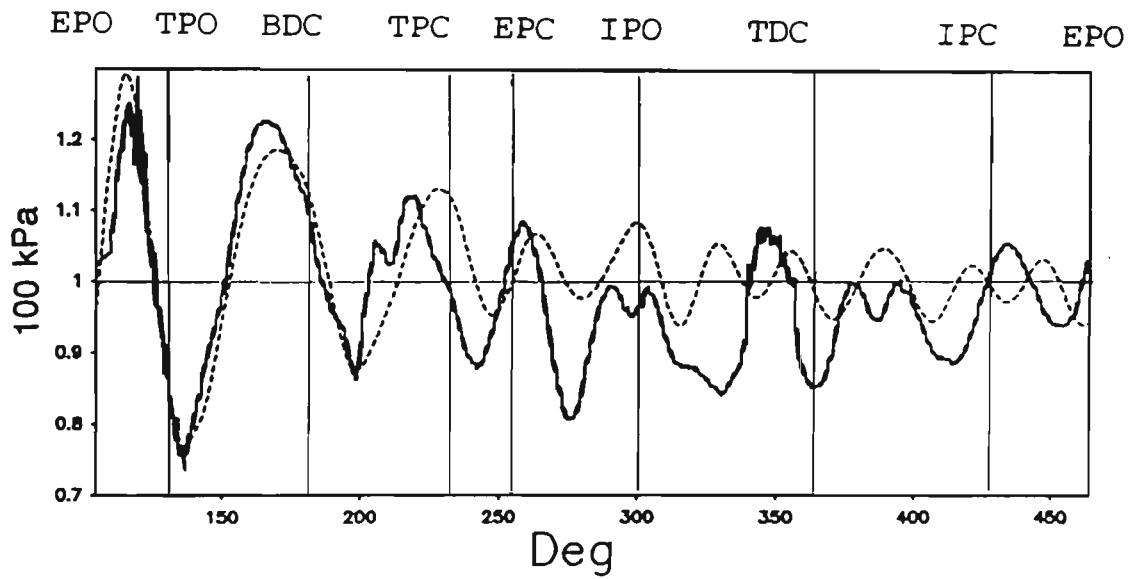
6.4 Discussion

The experimental observations obtained in this study indicate that the amplitude of the exhaust pulse is a complex function of engine speed, exhaust configuration and the residual wave pattern in the pipe. The large oscillations in pressure amplitude at the exhaust port after the port closure implies that the wave energy was not fully utilised in assisting scavenging, refer to figures (b) in Fig.6.6 - 6.12.

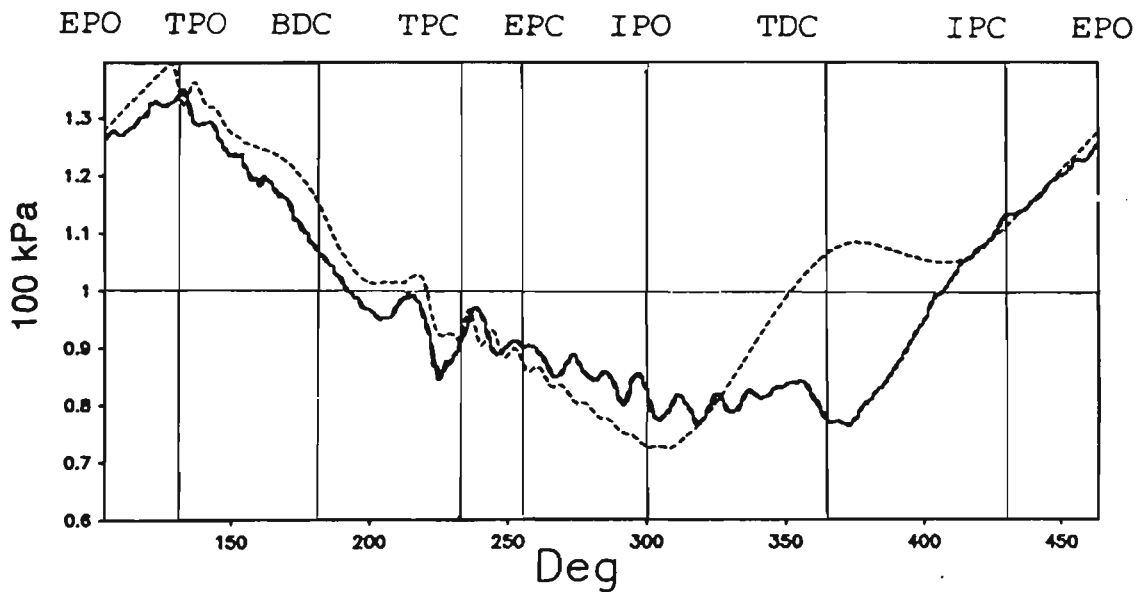
Although experiments confirmed good improvements in engine torque/power have been achieved by substituting the expansion chamber for the box silencer, Fig. 6.1 - 6.5 and Fig.4.4, it is clear that the returning "suction wave" and the succeeding "plugging wave" arrived at the exhaust port too early in all cases, figures (b) in Fig. 6.6 - 6.12, compared to the ideal waveform in Fig. 2.8, leading to the relatively inefficient evacuation of the cylinder during the gas exchange period, thus hindering the further improvement of the engine performance. The further computer simulation shows (for $L_3=400$ mm) that the ideal exhaust waveform at port appears at 5500 RPM with a power output as high as 5.6 kW.



(a) Cylinder

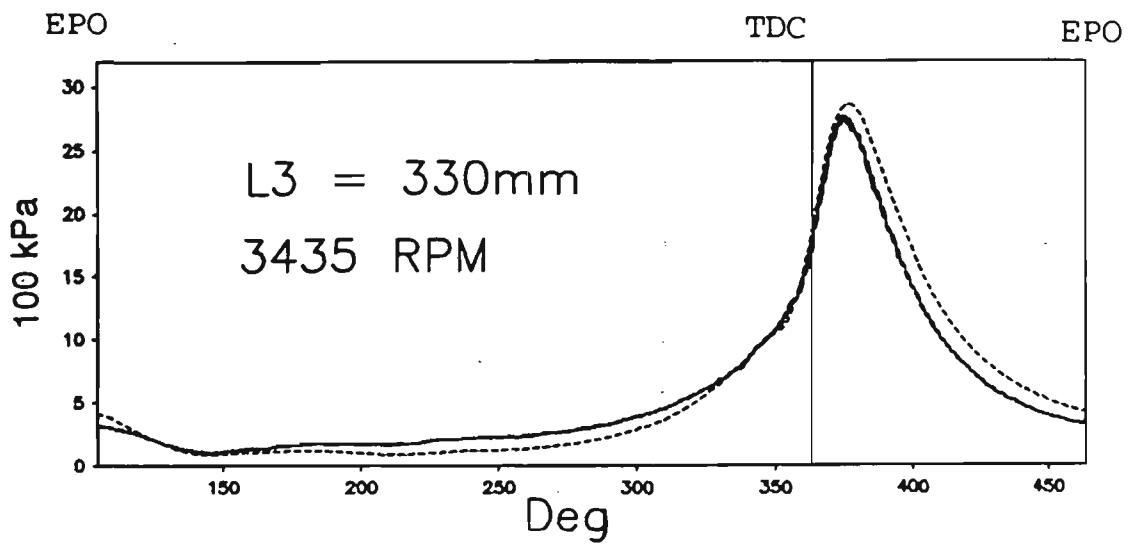


(b) Exhaust port

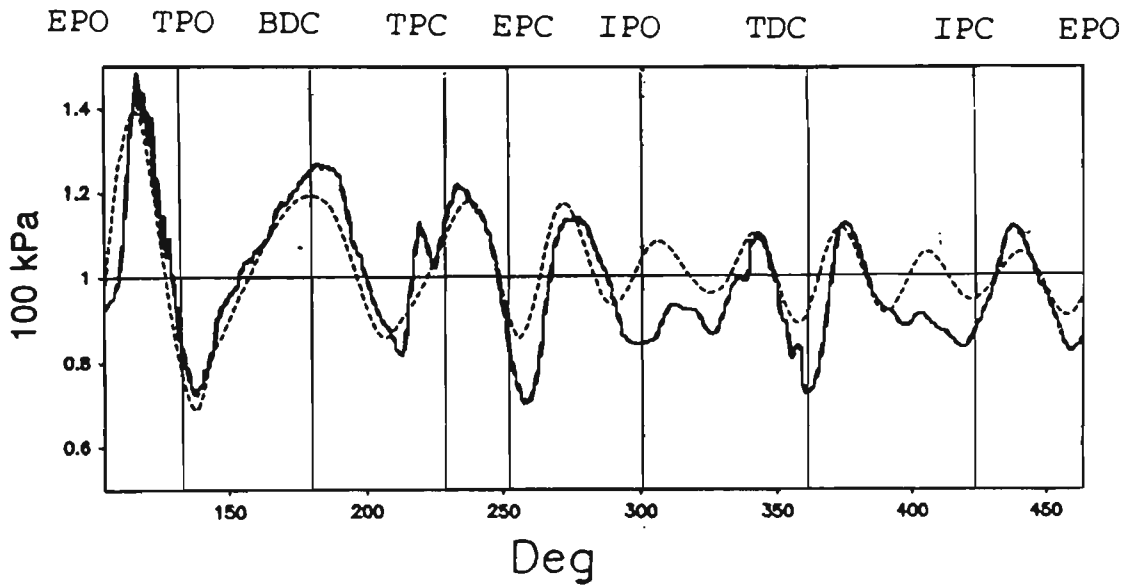


(c) Transfer port

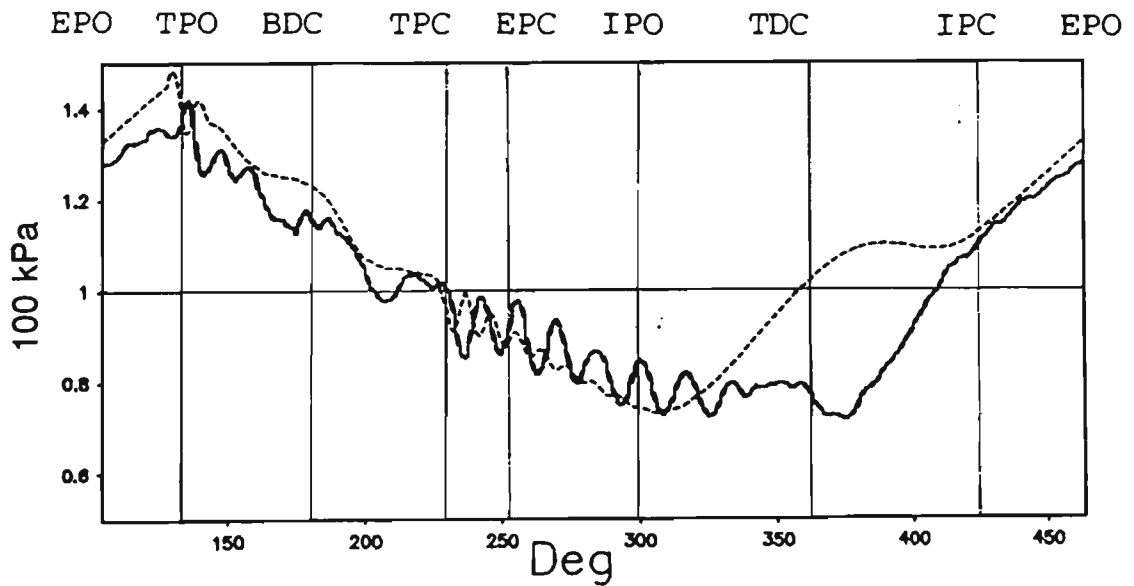
Fig. 6.6 Pressure histories at various locations for 2900 RPM and $L_3 = 330$ mm



(a) Cylinder

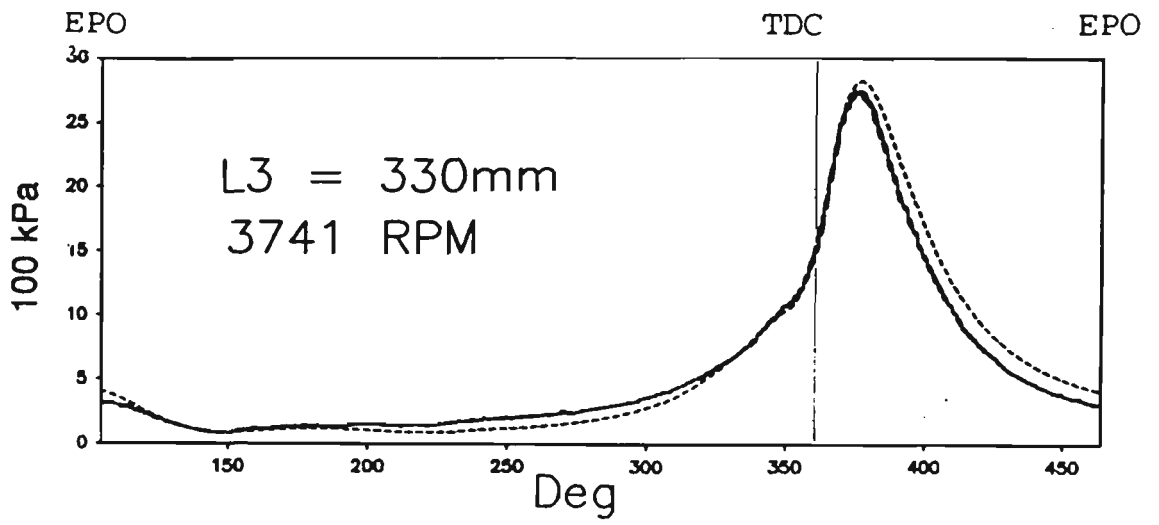


(b) Exhaust port

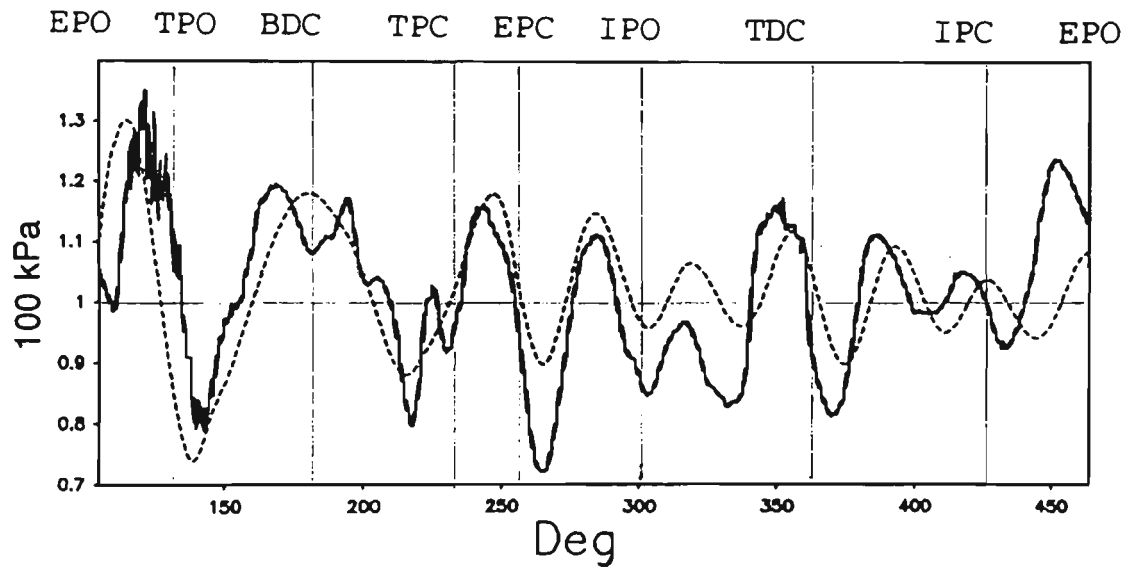


(c) Transfer port

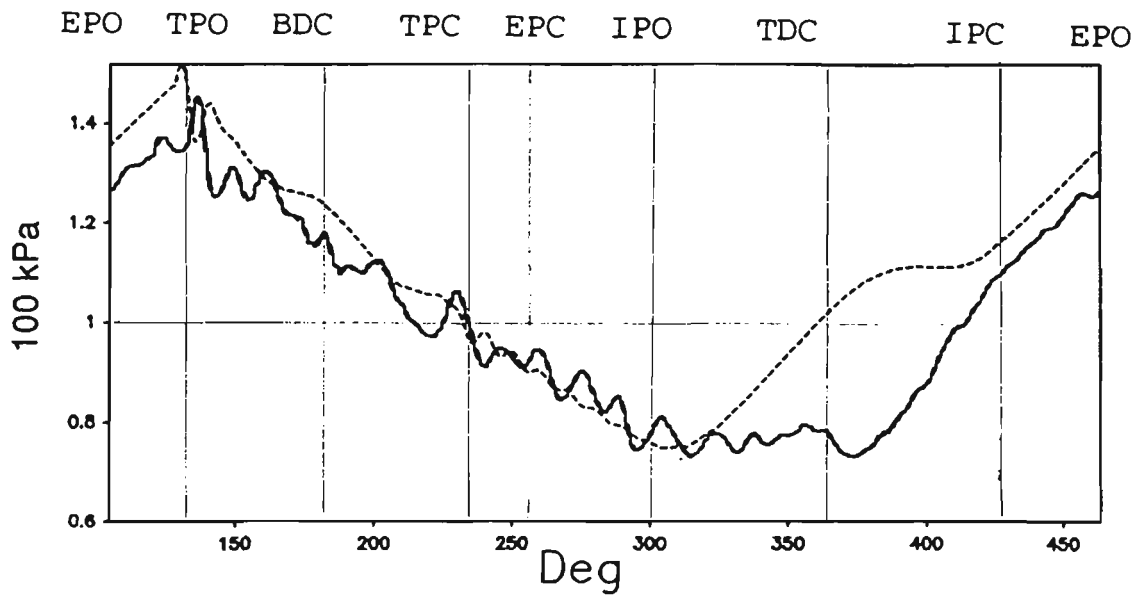
Fig. 6.7 Pressure histories at various locations for 3435 RPM and $L_3 = 330$ mm



(a) Cylinder

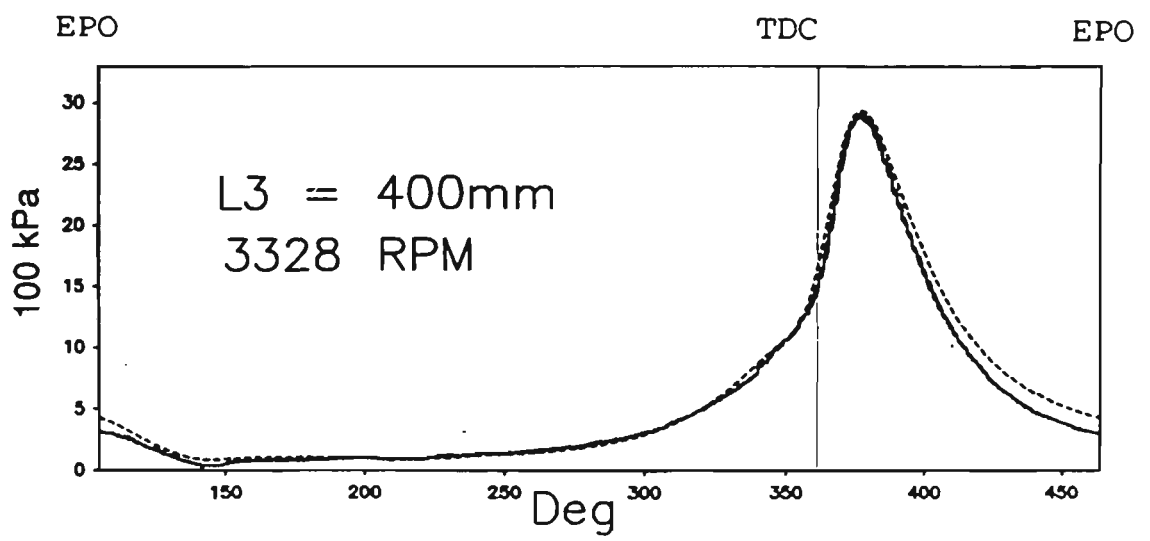


(b) Exhaust port

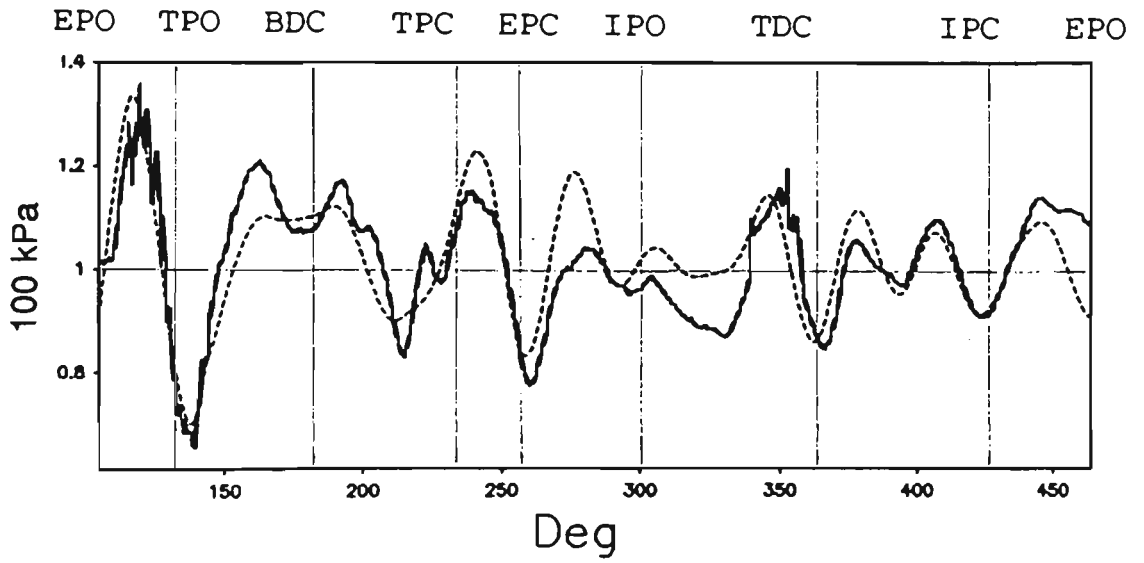


(c) Transfer port

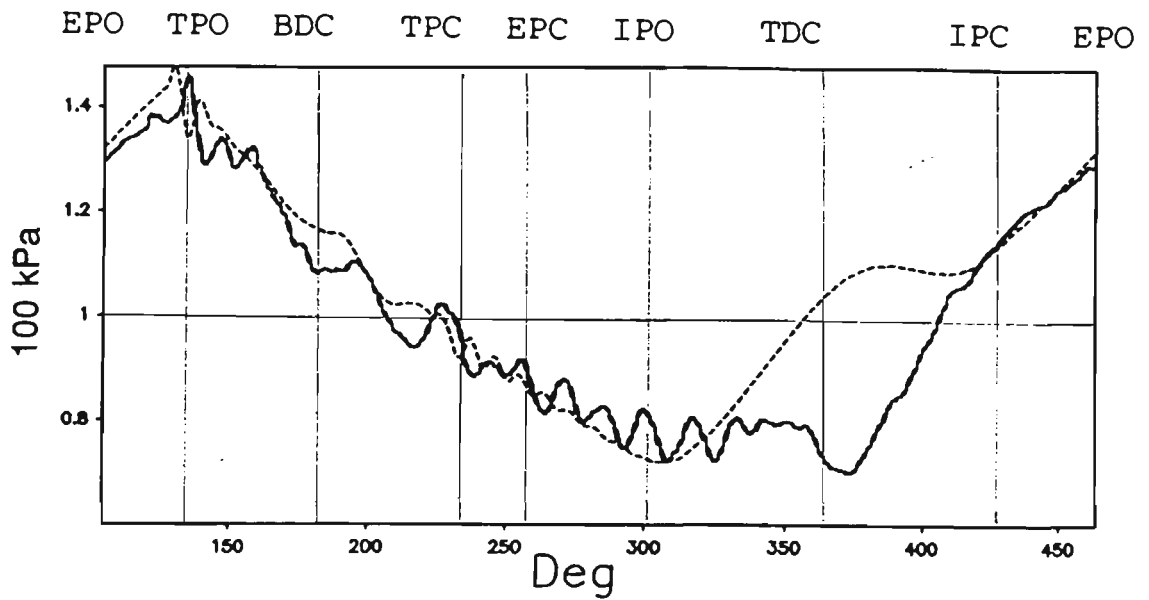
Fig. 6.8 Pressure histories at various locations for 3741 RPM and $L_3 = 330$ mm



(a) Cylinder

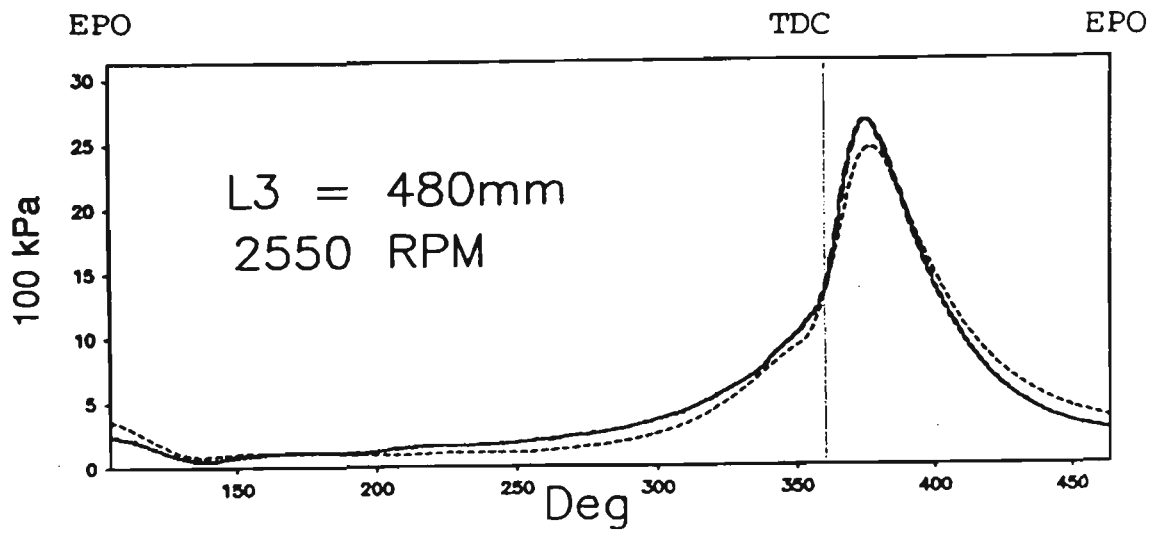


(b) Exhaust port

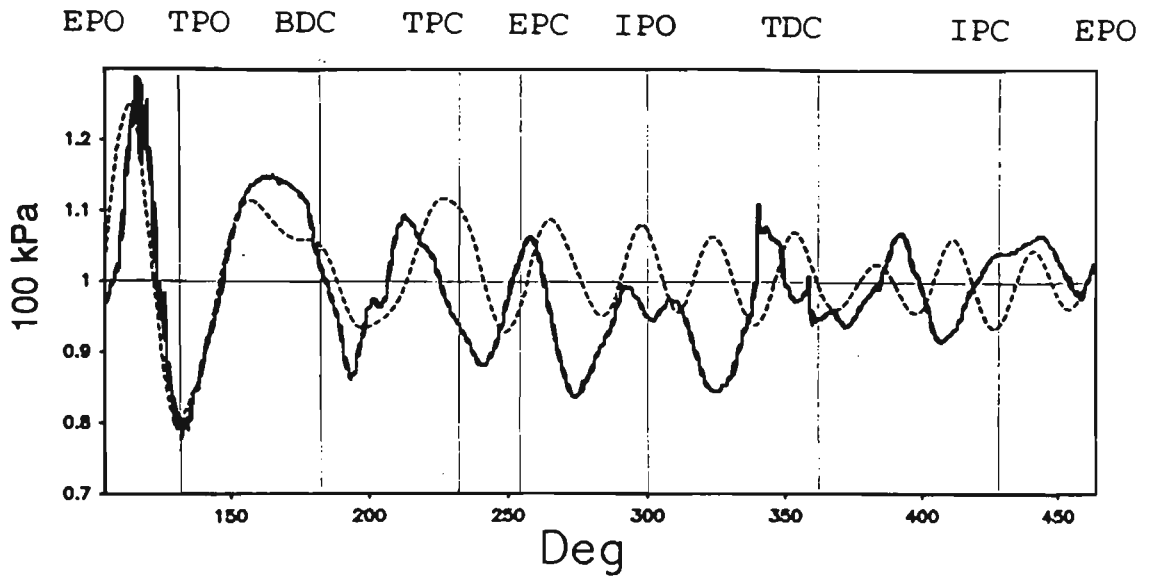


(c) Transfer port

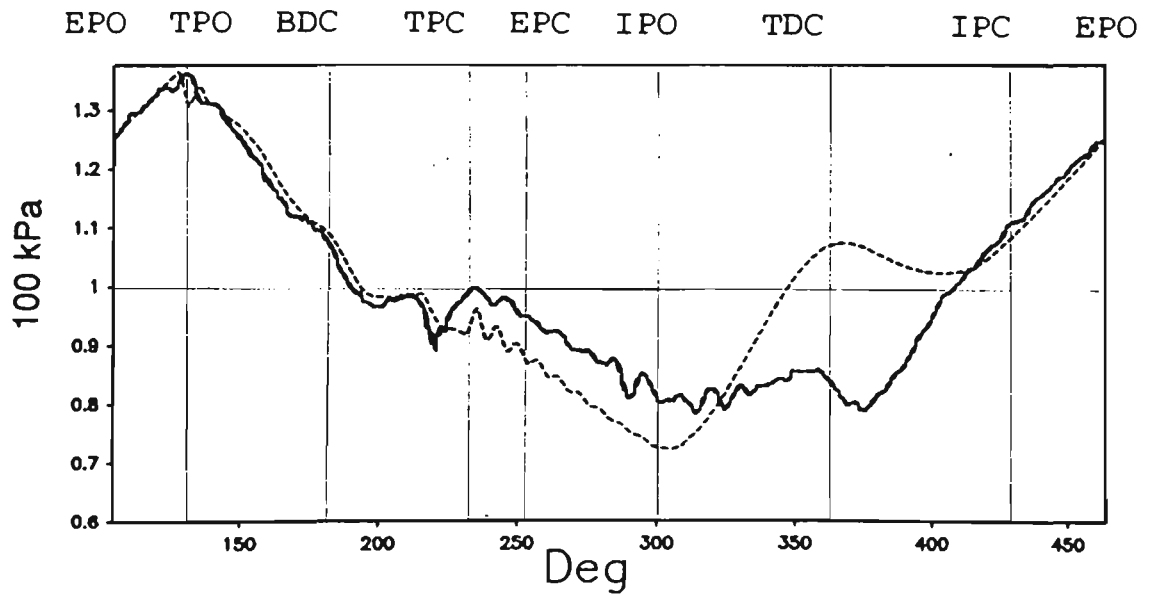
Fig. 6.9 Pressure histories at various locations for 3328 RPM and $L_3 = 400$ mm



(a) Cylinder

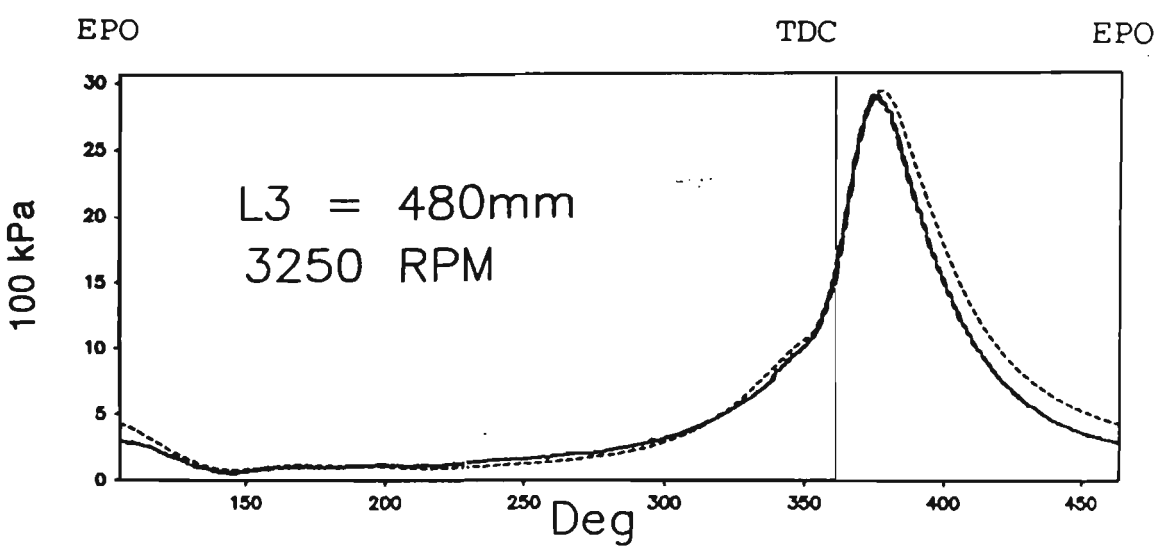


(b) Exhaust port

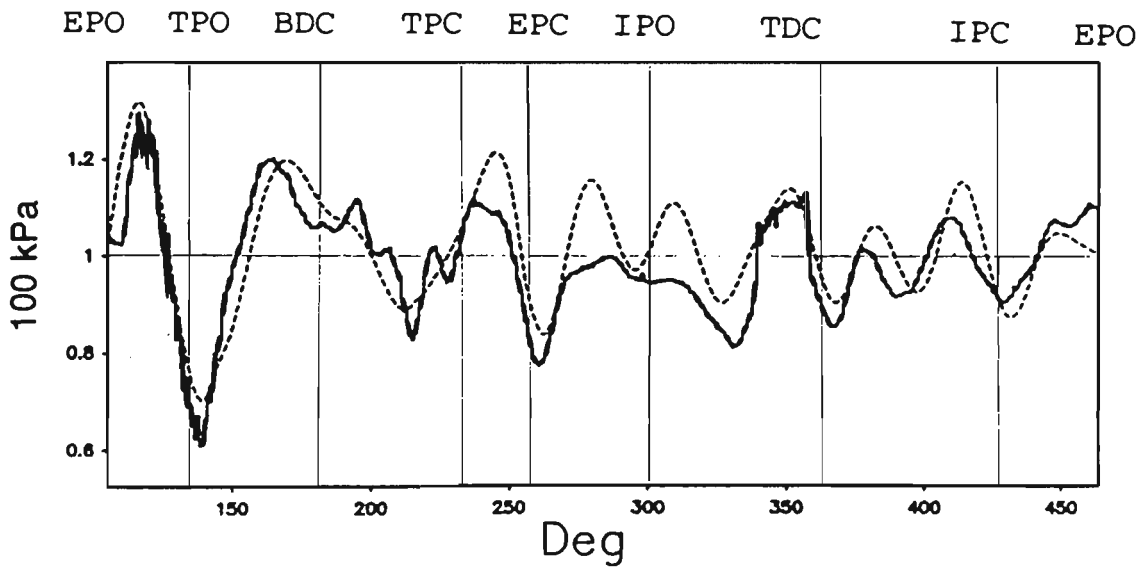


(c) Transfer port

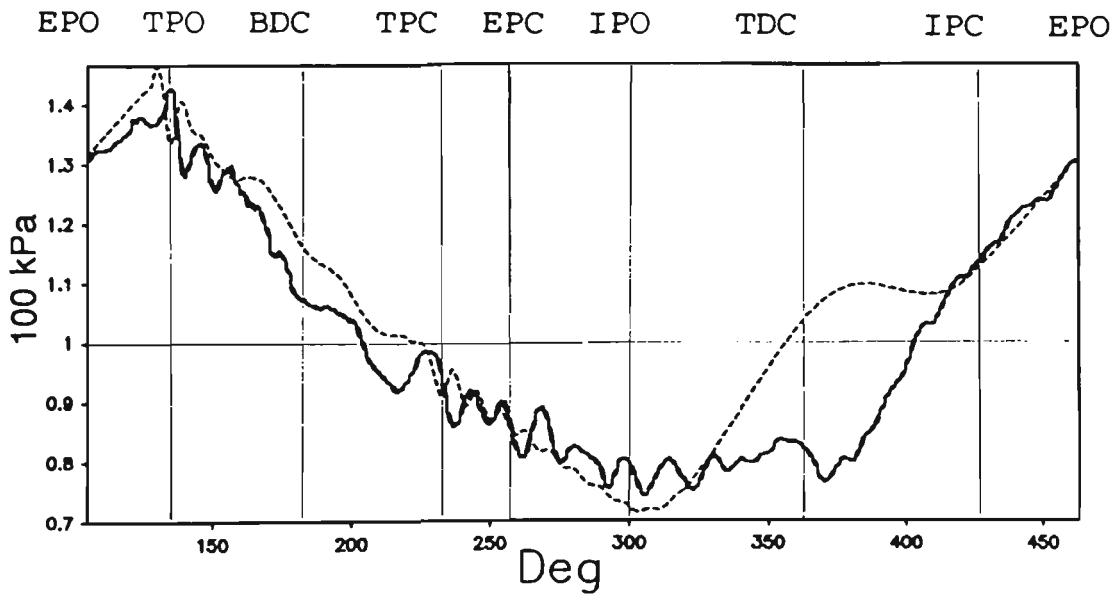
Fig. 6.10 Pressure histories at various locations for 2550 RPM and $L_3 = 480$ mm



(a) Cylinder

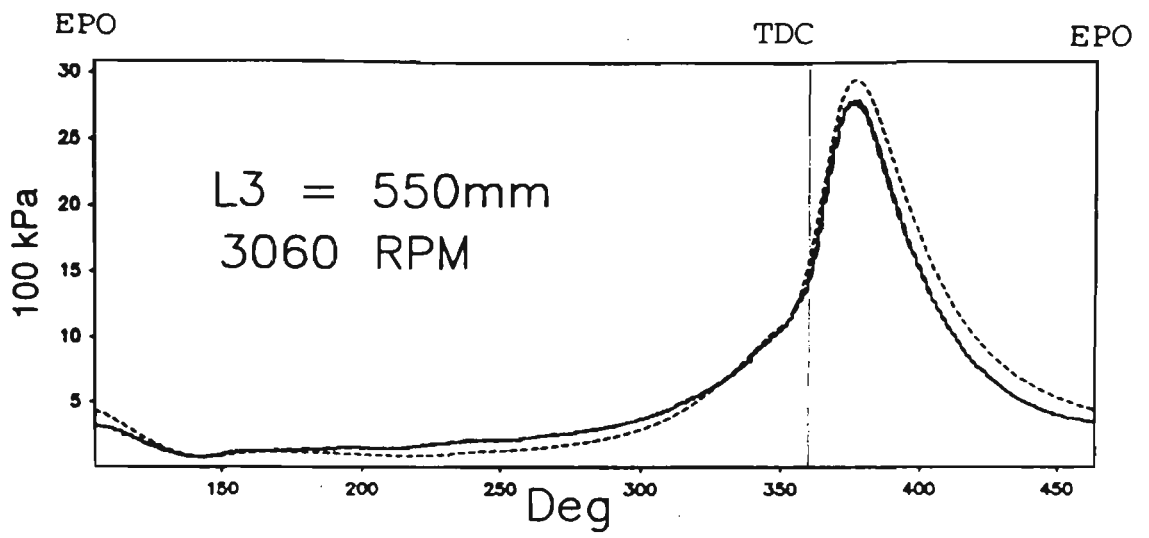


(b) Exhaust port

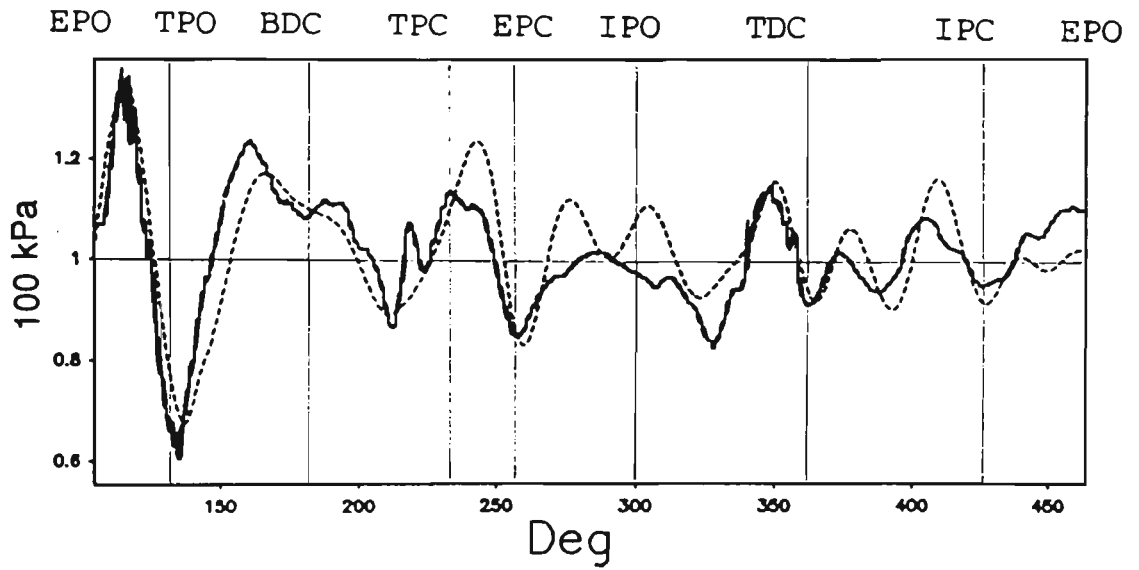


(c) Transfer port

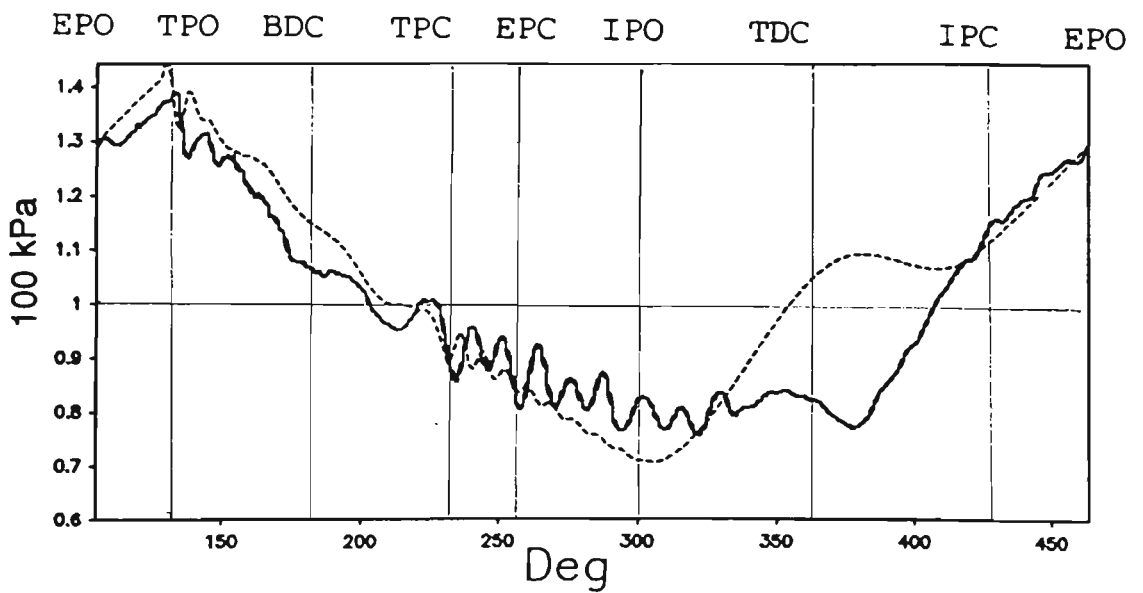
Fig. 6.11 Pressure histories at various locations for 3250 RPM and $L_3 = 480$ mm



(a) Cylinder



(b) Exhaust port



(c) Transfer port

Fig. 6.12 Pressure histories at various locations for 3060 RPM and $L_3 = 550$ mm

CHAPTER SEVEN

CONCLUSIONS

7.1 Research Achievement

In this project, the three objectives set out in Chapter One have been achieved.

1. The two-stroke engine simulation model has been developed to predict the steady state performance characteristic of a crankcase compressed, piston port-timed, two-stroke engine equipped with expansion chamber. The parameters include engine torque and power, BSFC, scavenging efficiency, charging efficiency and so on. It also has the ability to predict the unsteady gas dynamic behaviour in various engine pipes. The instantaneous pressure fluctuations and mass flow rates at inlet port, transfer port and exhaust port were calculated and analysed.

The model has several advantages compared with other previous model. It includes an improved procedure to account for the variation in geometry of the pipe and to determine the thermodynamic states in the cylinder/crankcase. It also considered the temperature discontinuity at the port/pipe interface. All these effort increases the accuracy and numerical stability of the prediction.

2. A single cylinder two-stroke engine dynamometer rig and dedicated fast data acquisition hardware and software have been developed during the project. Engine torque, speed and fuel consumption can be measured from the dynamometer rig. The dynamic pressure signals in engine cylinder, transfer port and exhaust port, together with crankshaft position signal, can be acquired at a speed of 50,000 samples/second per channel.
3. Substantial simulations and experiments were performed and the computer model was validated.

7.2 Conclusions

A variable exhaust system, as described in this study, can be used to improve a two-stroke engine's performance under off-design engine speeds. This can be realised by making the mid-parallel section of a conventional expansion chamber extendable, while the other dimensions of that chamber remained unchanged. In the study it was found that with the adjustable expansion chamber, the pressure wave timing at the exhaust port was under control within the test speed range (2200 - 4400 RPM) so that such wave timing always relatively well matches the engine port timing. The numerical approach proposed can satisfactorily handle the complicated pipe flow calculation and predict both engine performance and dynamic wave variations in the test engine with accuracy. The program can be used for improving the design and development of naturally aspirated, port-controlled crankcase compressed two-stroke engines.

7.3 Recommendation For Future Work

Based on the current study, the following recommendation are made for further work:

1. The two-stroke engine data acquisition program can calculate the instantaneous cylinder volume based on the crank shaft position signal. Therefore, a subroutine can be written to calculate the engine indicated work by integrating the cylinder pressure-cylinder volume envelope.
2. As the engine performance in terms of torque/BMEP is a function of exhaust pipe length L_3 , a self-adjustable exhaust pipe can be designed to automatically modify the pipe length for best torque/BMEP.
3. As described in section 3.2.3 and 3.9, the solution for port/pipe boundary condition (which governs the reflection of pressure wave at such interface) used in the two-stroke engine simulation program was based on the assumption that the specific heat ratio of gas is $\gamma=1.4$. The actual γ for the gas in two-stroke engine is a

function of gas composition and temperature and the solution should ultimately account for this factor.

4. To further increasing the accuracy of the computer model prediction, a subroutine can be developed to solve for the Riemann variables at new time step, λ_{n^*} and β_{n^*} , using Euler predictor-corrector algorithm.

REFERENCES

1. Tsuchiya, K., Hirano S., Okamura, M. and Gotoh, M., Emission control of two-stroke motorcycle engines by the butterfly exhaust valve, SAE 800973
2. Sher, E., Hacoheh, Y., Refael, S. and Harari, R., Minimising short-circuiting losses in two-stroke engine by throttling the exhaust pipe, SAE paper 901665
3. Blundell, D. W. and Sandford, M. H., Two stroke engine - the Lotus approach, SAE 920779
4. Blair, G. P., Computer-aided design for small two-stroke engines for both performance characteristics and noise level, I. Mech. E. automobile division conference on small internal combustion engine, paper no. C120/78, Isle of Man, 1978
5. Blair, G. P. and Hinds, E. T., Predicting the performance characteristics of two-cycle engines fitted with reed induction valves, SAE 790842
6. Sher, E., Improving the performance of a crankcase-scavenged 2-S engine with a fluid diode, Proc. Inst. Mech. Engrs, 196. (1982)
7. Sher, E. and Yafe, H., Flattening the torque curve of a two-stroke engine with a fluid diode installed at the scavenge port, SAE 830092
8. Blair, G.P., The basic design of two-stroke engines, Society of Automotive Engineers, 1990
9. Sher, E., Prediction of the gas exchange performance in a two-stroke cycle engine, SAE paper 850086 (1985)
10. Recommended practice, Engine terminology and nomenclature, SAE J. 604, SAE

Handbook, p24.01, (1987)

11. Dedeoglu, N., Scavenging model solves problems in gas burning engine, SAE paper 710579 (1971)
12. Oka, T. and Ishihara, S., Relation between scavenging flow and its efficiency of a two-stroke cycle engine, Bull. JSME 14(69), 257-267, (1971)
13. Rizk, W., Experimental studies of the mixing processes and flow configurations in two-cycle engine scavenging, Proc. Inst. Mech. Eng., 172(1), 417-437, (1958)
14. Ohigashi, S. and Kashiwada, Y., On the scavenging of two-stroke diesel engine, Bull. JSME 4(16), 669-705, (1961)
15. Ohigashi, S. and Kashiwada, Y., A study on the scavenging air flow through the scavenging ports, Bull. JSME 9(36), 777-784, (1966)
16. Phatak, R.G., A new method of analysing two-stroke cycle engine gas flow patterns, SAE paper 790487 (1979)
17. Martini, R. and Oggero, M., Experimental methods for the study of two-stroke engine scavenging, SAE paper 710145 (1971)
18. Reddy, K.V., Ganesan, V. and Gopalakrishnan, K.V., Under the roof of the cylinder head - an experimental study of the in-cylinder air movement in a two-stroke spark ignition engine, SAE paper 860166 (1986)
19. Jante, A., Scavenging and other problems of two-stroke cycle spark ignition engines, SAE paper 680468 (1968)
20. Ishihara, S., Murakami, Y. and Ishikawa, K., Improvement of pilot tube set for obtaining scavenging pictures of two-stroke cycle engines, SAE paper 880171 (1988)

21. Blair, G.P. and Kenny, R.G., Further developments in scavenging analysis for two-cycle engine, SAE paper 800038 (1980)
22. Sanborn D.S., Blair, G.P., Kenny, R.G. and Kingsbury, A.H., Experimental assessment of scavenging efficiency of two-stroke cycle engines, SAE paper 800975 (1980)
23. Blair, G.P., Studying scavenging flow in a two-stroke cycle engine, SAE paper 750752 (1975)
24. Killman, R.E., Lestz,S.S., and Meyer, W.E., Exhaust emission characteristics of a small 2-stroke cycle spark ignition engine, SAE paper 730159 (1973)
25. Hori, K., A method of measuring scavenging efficiency and its application, Bull. JSME 6(22), 289-296 (1963)
26. Hashimoto, E., Tottori, T. and Terata, S., Scavenging performance measurements of high speed two-stroke engines, SAE paper 850182 (1985)
27. Ahmadi-Befrui, B., Brandstatter, W. and Kratochwill, H., Multi-dimensional calculation of the flow processes in a loop scavenged two-stroke cycle engine, SAE paper 890841 (1989)
28. Schwarz, M.P., Thornton, G.J. and Gilbert, W., In-cylinder flow simulation for a motored two-stroke engine, 631-640, "Computational fluid dynamics", Elsevier Science Publishers B.V. (North-Holland), 1988
29. Plohberger, D., Mikulic, L.A. and Landfather, K., Development of a fuel injected two-stroke gasoline engine, SAE paper 880170
30. Smyth, J.G., Kenny, R.G. and Blair, G.P., Steady flow analysis of the scavenging process in a loop scavenged two-stroke cycle engine---a theoretical and experimental study, SAE paper 881267

31. Sher, E., Investigating the gas exchange process of a two-stroke cycle engine with a flow visualisation rig. *Israel J. Tech.*, 20, 127-136 (1982)
32. Maekawa, M., Text of course, JSME G36, 23 (1957)
33. Benson, R.S. and Brandham, P.T., A method for obtaining a quantitative assessment of the influence of charging efficiency on two-stroke engine performance, *Int. J. Mech. Sci.*, 11, 303-312, 1969
34. Sher, E., A new practical model for the scavenging process in a two-stroke cycle engine, SAE paper 850085
35. Sanborn, D.S. and Roeder, W.M., Single cycle simulation simplifies scavenging study, SAE paper 850175
36. Sweeney, M.E.G., Kenny, R.G., Swann, G.B. and Blair, G.P., Single cycle gas testing method for two-stroke engine scavenging, SAE paper 850178
37. Sammons, H., A single cycle test apparatus for studying loop-scavenging in a two-stroke engine, *Proc. I. mech. Eng.*, vol. 160, 1949, p233-246
38. Blair, G.P., Correlation of theory and experiment for scavenging flow in two-stroke cycle engines, SAE paper 881265
39. Dedeoglu, N. and Kajina, T., Two stage scavenging improves overall engine efficiency, SAE paper 881263
40. Wallace, F. J., and Mitchell, R. W. S., Wave action following the sudden release of air through an engine port system, *Proc. I. Mech. Eng. (B)*, vol.1B, p343 (1953)
41. Nagao, F., Nishiwaki, K., Kato, K. and Iijima, T., Prevention of back flow in a crankcase-scavenged two-stroke engine by fluid diodes, *Bull. JSME*, vol. 14, no.

71, pp 483-492, 1971

42. Sher, E., Improving the performance of a crankcase scavenged two-stroke engine with a fluid diode, Proc. I. Mech. Eng., vol.196, 1982
43. Sher, E. and Yafe, H., Flattening the torque curve of a two-stroke engine with a fluid diode installed at the scavenging port, SAE paper 830092
44. Winterbone, D.E., Chapter 19, Wave Action Simulation Models, "The Thermodynamics and Gas Dynamics of Internal Combustion Engines", Volume 2, Clarendon Press, Oxford, 1986
45. Saxena, M., Radzimirski, S. and Mathur, H.B., Reduction of fresh charge losses by selective exhaust gas recirculation (SEGR) in two-stroke engines, SAE paper 891806
46. Wallace, F. J., and Nassif, M. H., Air flow in a naturally aspirated two-stroke engine, Proc. I. Mech. Eng., vol.1B (1953)
47. Benson, R.S., The thermodynamics and gas dynamics of internal combustion engine, volume 1, Clarendon press, Oxford, 1982
48. Blair, G. P. and Cahoon, W. L., A more complete analysis of unsteady gas flow through a high specific output two-cycle engine, SAE 720156, 1972
49. Blair, G. P., Prediction of two-cycle engine performance characteristics, SAE 760645, 1976
50. Bannister, F. K., and Mucklow, G. F., Wave action following sudden release of compressed gas from a cylinder, Proc. I. Mech. Eng., vol. 159, p. 269, (1948)
51. Zucrow, M. J. and Hoffman, J. D., Gas Dynamics, Wiley, New York, 1977

52. Courant, R., Friedrichs, K. and Lewy, H., Translation report NYO-7689, Math. Ann., vol. 100, p32, 1928
53. Annand, W. J. D., Heat transfer in the cylinder of reciprocating internal combustion engines, Proc. Inst. Mech. Engr, vol.177, 1963
54. Annand, W.J.D. and Roe, G.E., Gas flow in the internal combustion engine, G T Foulis &Co LTD, Sparkford, Yeovil, Somerset, England
55. Sher, E., The effect of atmospheric conditions on the performance of an air-borne tow-stroke spark ignition engine, Proc. I. Mech. E., vol 198 D, No.1, 1984
56. Fleck,R., Houston, R. A. and Blair G. P., Predicting the performance characteristics of twin cylinder two-stroke engines for outboard motor applications, SAE 881266

The scavenging efficiency is evaluated in terms of oxygen concentration available from the analyser reading. The scavenging ratio is determined by moving the piston inward at the completion of the single cycle experiment until the original crankcase state is restored. A dial gauge records the piston movement precisely. As the piston area is known, the volume of the charge which leaves the crankcase is determined. The volume of charge which scavenges the cylinder is calculated by the equation of state, considering that the temperature in the cylinder and crankcase are equal, and the cylinder pressure is at atmospheric pressure. According to the definition, this volume divided by the cylinder sweep volume is the scavenging ratio.

The resulting scavenging efficiency-scavenging ratio characteristics measured from the QUB single cycle apparatus provides important information for the validation of the theoretical modelling of the scavenging process. Also, as the fuel-fresh air mixture trapped at the completion of the scavenging process is related to the scavenging efficiency, a particular η_s - λ_s characteristics is necessary for computer simulation which predicts that engine performance. Single cycle apparatus provides useful information of this kind.

Appendix B: Computer Program for Unsteady Quasi One-Dimensional Pipe Flow

```
SUB PIPE (KA, KB, A(), A2at1, B(), DF(), F(), WA1, WB1, RA1, RB1, DXW1, DXR1, SDPT, SDPP,  
SDW, SDR) STATIC
```

```
SHARED DZ, A2(), B2(), PIPEMODELS, KK
```

```
G1 = 3
```

```
G2 = 2
```

```
KC = KB - 1
```

```
FOR J = KA TO KC
```

```
AA = DZ * A(J + 1) * B(J)
```

```
BB = DZ * A(J) * B(J + 1)
```

```
Y = (1 + DZ * (G1 * (A(J + 1) - A(J)) - G2 * (B(J + 1) - B(J))))
```

```
Z = (1 + DZ * (G1 * (B(J) - B(J + 1)) - G2 * (A(J) - A(J + 1))))
```

```
WA = (A(J + 1) + G2 * AA - G2 * BB) / Y
```

```
RA = (A(J) - G1 * BB + G1 * AA) / Z
```

```
WB = (B(J + 1) + G1 * AA - G1 * BB) / Y
```

```
RB = (B(J) + G2 * AA - G2 * BB) / Z
```

```
AA = WA - WB
```

```
BB = RA - RB
```

```
CC = WA + WB
```

```
DD = RA + RB
```

```
DXW = (3 * WA - 2 * WB) * DZ
```

```
DXR = (3 * RB - 2 * RA) * DZ
```

```
DXM = DXW / 2
```

```
DXN = DXR / 2
```

```
IF J = 1 THEN
```

```
    WA1 = WA
```

```
    WB1 = WB
```

```
    RA1 = RA
```

```
    RB1 = RB
```

```
    DXW1 = DXW
```

```
    DXR1 = DXR
```

```
END IF
```

```
IF PIPEMODELS = "A" OR PIPEMODELS = "B" OR PIPEMODELS = "C" OR PIPEMODELS = "D"  
THEN
```

$$FW = F(J + 1) - DXW * (F(J + 1) - F(J))$$

$$FM = F(J + 1) - DXM * (F(J + 1) - F(J))$$

$$DFW = F(J + 1) - FW$$

$$FR = F(J) + DXR * (F(J + 1) - F(J))$$

$$FMR = F(J) + DXN * (F(J + 1) - F(J))$$

$$DFR = FR - F(J)$$

ELSE

'DFW below is actually DFONFDX() at point W, etc.

$$DFW = DF(J + 1) - DXW * (DF(J + 1) - DF(J))$$

$$DFR = DF(J) + DXR * (DF(J + 1) - DF(J))$$

$$DFM = DF(J + 1) - DXM * (DF(J + 1) - DF(J))$$

$$DFN = DF(J) + DXN * (DF(J + 1) - DF(J))$$

END IF

IF PIPEMODEL\$ = "A" THEN

$$QA = -DZ * CC * AA * DF(J) / (4 * F(J))$$

$$QB = -DZ * BB * DD * DF(J) / (4 * F(J))$$

ELSEIF PIPEMODEL\$ = "B" THEN

$$QA = -DZ * CC * AA * DF(J) / (4 * ((F(J + 1) - F(J)) / 2 + F(J)))$$

$$QB = -DZ * BB * DD * DF(J) / (4 * ((F(J + 1) - F(J)) / 2 + F(J)))$$

ELSEIF PIPEMODEL\$ = "C" THEN

$$QA = -DZ * CC * AA * DFW / (4 * DXW * FW)$$

$$QB = -DZ * BB * DD * DFR / (4 * DXR * FR)$$

ELSEIF PIPEMODEL\$ = "D" THEN

$$QA = -DZ * CC * AA * DFW / (4 * DXW * FM)$$

$$QB = -DZ * BB * DD * DFR / (4 * DXR * FMR)$$

ELSEIF PIPEMODEL\$ = "E" THEN

$$QA = -DZ * CC * AA * DFW / 4$$

$$QB = -DZ * BB * DD * DFR / 4$$

ELSE

PIPEMODEL\$ = "F"

QA = -DZ * CC * AA * DFM / 4

QB = -DZ * BB * DD * DFN / 4

END IF

A2(J + 1) = WA + QA

B2(J) = RB + QB

IF J = 1 THEN

DA2(J + 1) = .25 * ((WB1 - WA1) / SDW + (B2(J + 1) - A2(J + 1)) / SDPP) * (SDPP - SDW)

A2(J + 1) = A2(J + 1) + DA2(J + 1)

DB2(J) = .25 * ((RB1 - RA1) / SDR + (B2(J) - A2at1) / SDPT) * (SDPT - SDR)

B2(J) = B2(J) + DB2(J)

'PRINT KK, SDPT, SDW, SDR, SDPP, DA2(2), DB2(1)

END IF

NEXT J

FOR J = KA TO KC

A(J + 1) = A2(J + 1)

B(J) = B2(J)

'PRINT J, A(2), B(2)

NEXT J

END SUB

Appendix C: Computer Model Testing of the Effect of Various Schemes on the Changes of Pipe Area

Note: to find the general input data for the simulations presented in Appendix C-E,

- a) for the YAMAHA engine, see Fig. 4.2 on page 93 and Table 5.1 on page 107.
- b) for GRAND PRIX engine, see page 209 of Blair's monograph [24].

1) Simulation of YAMAHA engine at 3435 RPM with $L_3 = 330$ mm

	*Solution A	Solution B	Solution C
Power (kW)	3.18	3.23	3.15
Toque (NM)	8.85	8.97	8.75
BMEP (100 kPa)	5.24	5.3	5.18
BSFC (g/kWH)	523	511	514
Scav. eff. (%)	76.40%	76.20%	75.32%
Trapping eff. (%)	56.74%	57.80%	57.59%
Charging eff. (%)	46.50%	46.90%	45.96%
K_{in}	0.822	0.813	0.799
K_{ex}	0.84	0.832	0.816
K_{tr}	0.839	0.831	0.815
ϵ_{ex} (%)	27.13%	4.65%	8.95%
ϵ_{tr} (%)	0.0105%	-0.0082%	-0.0005%
ϵ_{in} (%)	0.0941%	-0.1560%	-0.1015%

* Solution A is suggested in reference[24]. Solution B and C are discussed in Section 3.8 of this thesis on page 63.

2) Simulation on YAMAHA Engine at 3042 RPM With L3 = 550 mm

	Solution A	Solution B	Solution C
Power (kW)	2.88	2.96	2.94
Toque (NM)	9.04	9.29	9.23
BMEP (100 kPa)	5.35	5.50	5.46
BSFC (g/kWH)	509	497	498
Scav. eff. (%)	76.73%	76.86%	77.57%
Trapping eff. (%)	58.00%	59.34%	59.18%
Charging eff. (%)	47.32%	48.53%	48.19%
K_{in}	0.816	0.819	0.815
K_{ex}	0.838	0.840	0.835
K_{tr}	0.837	0.838	0.833
ϵ_{ex} (%)	26.88%	4.21%	7.86%
ϵ_{tr} (%)	0.0021%	-0.00706%	-0.0028%
ϵ_{in} (%)	0.0346%	-0.1129%	-0.1838%

3) Simulation of GP Engine at 11500 RPM

	Solution A	Solution B	Solution C
Power (kW)	17.19	16.33	16.33
Toque (NM)	14.27	13.56	13.55
BMEP (100 kPa)	7.25	6.89	6.89
BSFC (g/kWH)	424	404	396
Scav. eff. (%)	83.79%	79.52%	79.14%
Trapping eff. (%)	65.93%	69.32%	71.51%
Charging eff. (%)	56.13%	53.58%	53.91%
K_{in}	0.8503	0.7812	0.7631
K_{ex}	0.9127	0.82	0.818
K_{tr}	0.9125	0.8262	0.817
ϵ_{ex} (%)	34.15%	8.91%	10.78%
ϵ_{tr} (%)	-0.0154%	-2.4730%	-3.0225%
ϵ_{in} (%)	-0.9512%	-1.1744%	-1.0106%

Appendix D: Computer Model Testing of the Effect of Various Computational Mesh Sizes

1) Simulation of YAMAHA Engine at 3435 RPM With L3 = 330 mm

	*msize=50	msize=30	msize=10	msize=5
Power (kW)	3.08	3.24	3.22	3.212
Toque (NM)	8.56	8.98	8.96	8.93
BMEP (100 kPa)	5.06	5.32	5.3	5.28
BSFC (g/kWH)	513	523	512	513
Scav. eff. (%)	74.82%	77.06%	76.12%	76.10%
Trapping eff. (%)	57.46%	56.46%	57.76%	57.70%
Charging eff. (%)	44.80%	47.06%	46.96%	46.83%
K_{in}	0.7797	0.833	0.8133	0.812
K_{ex}	0.7879	0.847	0.8326	0.833
K_{tr}	0.7876	0.847	0.8315	0.832
ϵ_{ex} (%)	21.93%	12.97%	4.65%	3.59%
ϵ_{tr} (%)	-0.0026%	-0.0078%	-0.0082%	-0.0055%
ϵ_{in} (%)	-0.6375%	-0.3408%	-0.1562%	-0.1252%

*msize: mesh size (mm)

2) Simulation of GP Engine at 11500 RPM

	msize=50	msize=30	msize=10	msize=5
Power (kW)	15.69	16.06	16.33	16.4
Toque (NM)	13.03	13.34	13.56	13.63
BMEP (100 kPa)	6.62	6.78	6.89	6.91
BSFC (g/kWH)	462	439	405	395
Scav. eff. (%)	82.83%	81.18%	79.52%	79.30%
Trapping eff. (%)	61.29%	64.59%	69.26%	71.80%
Charging eff. (%)	51.79%	53.36%	53.45%	54.11%
K_{in}	0.846	0.824	0.771	0.7535
K_{ex}	0.896	0.87	0.826	0.817
K_{tr}	0.896	0.87	0.826	0.817
ϵ_{ex} (%)	28.96%	20.08%	9.22%	5.93%
ϵ_{tr} (%)	1.2980%	-0.7507%	-2.3580%	-3.2440%
ϵ_{in} (%)	-0.0811%	0.3799%	-1.0720%	-1.0620%

Appendix E: Computer Model Testing of the Effect of Modifications of Wave Reflection Near Engine Ports Due to Discontinuous Reference Temperatures

	No(3301) ¹	Yes(3301) ²	No(5501) ³	Yes(5501) ⁴
Power (kW)	3.22	3.28	2.96	3.01
Toque (NM)	8.96	9.11	9.29	9.45
BMEP (100 kPa)	5.3	5.59	5.5	5.59
BSFC (g/kWH)	511	481	497	477
Scav. eff. (%)	76.12%	76.23%	76.86%	77.26%
Trapping eff. (%)	57.76%	61.34%	59.33%	61.66%
Charging eff. (%)	46.96%	47.66%	48.53%	49.24%
K_{in}	0.81	0.778	0.818	0.8
K_{ex}	0.833	0.85	0.84	0.86
K_{tr}	0.831	0.85	0.838	0.86
ϵ_{ex} (%)	4.64%	2.04%	4.20%	1.40%
ϵ_{tr} (%)	-0.0082%	4.3090%	0.0071%	3.4300%
ϵ_{in} (%)	-0.1562%	-1.4017%	-0.1130%	-0.9170%
		Yes(5502) ⁵	No(GP) ⁶	Yes(GP) ⁷
Power (kW)		3.43	16.83	16.4
Toque (NM)		7.57	13.98	13.63
BMEP (100 kPa)		4.48	7.1	6.91
BSFC (g/kWH)		569	408	395
Scav. eff. (%)		72.73%	81.02%	79.30%
Trapping eff. (%)		53.11%	68.50%	71.80%
Charging eff. (%)		40.54%	54.98%	54.11%
K_{in}		0.764	0.8027	0.7535
K_{ex}		0.78	0.857	0.817
K_{tr}		0.78	0.857	0.817
ϵ_{ex} (%)		1.19%	7.85%	5.93%
ϵ_{tr} (%)		0.8345%	0.0327%	-3.2440%

